Metamaterial-Enabled Transformation Optics

by

Nathan Landy

Department of Department of Electrical and Computer Engineering
Duke University

Date: _____

Approved:

_____
David R. Smith, Supervisor

_____
Steven A. Cummer

_____
Daniel J. Gauthier

_____
Nathan B. Kundtz

_____
Qing H. Liu

_____
Matthew S. Reynolds

Dissertation submitted in partial fulfillment of the requirements for the degree of Doctor of Philosophy in the Department of Department of Electrical and Computer Engineering
in the Graduate School of Duke University
2013

Abstract

Metamaterial-Enabled Transformation Optics

by

Nathan Landy

Department of Department of Electrical and Computer Engineering
Duke University

Date: _____

Approved:

_____
David R. Smith, Supervisor

_____
Steven A. Cummer

_____
Daniel J. Gauthier

_____
Nathan B. Kundtz

_____
Qing H. Liu

_____
Matthew S. Reynolds

An abstract of a dissertation submitted in partial fulfillment of the requirements for the degree of Doctor of Philosophy in the Department of Department of Electrical and Computer Engineering
in the Graduate School of Duke University
2013

Abstract

Transformation Optics (TO) is a design methodology that uses the form invariance of Maxwell's equations to distort electromagnetic fields. This distortion is imposed on a region of space by mimicking a curvilinear coordinate system with prescribed magnetoelectric material parameters. By simply specifying the correct coordinate transformation, researchers have created such exotic devices as invisibility cloaks, "perfect" lenses, and illusion devices.

Unfortunately, these devices typically require correspondingly exotic material parameters that do not occur in Nature. Researchers have therefore turned to complex artificial media known as metamaterials (MMs) to approximate the desired responses. However, the metamaterial design process is complex, and there are limitations on the responses that they achieve.

In this thesis, I explore both the applicability and limitations of metamaterials in TO design. I begin by investigating quasiconformal (QC) transformations for two- and three-dimensional, (2D and 3D, respectively), TO devices. 2D-QC mappings yield material specifications that may be approximated with isotropic dielectrics. However, this approximation effectively distorts the transformed domain. This distortion can cause aberrant behavior in certain implementations. I have implemented a method to compensate for this distortion by re-scaling the size of my untransformed virtual domain.

I extend the QC method to 3D by revolving the mapping around an optical axis.

The 3D-QC method allows me to reduce the complexity of the material specification from six- to three- independent material parameters. This greatly simplifies the resulting MM design. I apply this technique to a specific device: a flattened Luneburg Lens. Both ray-tracing and full-wave simulations verify that a simplified anisotropic lens provides superior performance to an isotropic implementaton. Ray-tracing shows that my lens would produce an RMS spot diameter of less than four percent for field angles in the range 0- 45°. Similarly, full-wave analysis reveals that my reduced-parameter lens demonstrates diffraction-limited performance for aperture diameters greater than 15 wavelengths.

However, the approximations made in the design of such a lens may not be valid in other areas of TO design. For instance, the high-frequency approximations made in my lens design ignore the effects of impedance mismatch, and these approximations are not valid when the material parameters vary on the order of a wavelength. I therefore use other freedoms available to me to design, fabricate, and experimentally characterize a full-parameter cloak of invisibility. Specifically, I implement my cloak in a parallel-plate waveguide, and I corrugate the bottom plate to create a broadband paramagnetic loading inside the waveguide. By combining a corrugation with a conventional split ring resonator, I am able to tune three distinct material responses in a single metamaterial unit cell. With this unit cell, I create a unidirectional cloak capable of hiding an object six wavelengths in diameter at 10.2 GHz. My cloak reduces the scattering cross-section of a bare conducting cylinder by approximately 50% as measured by the total scattering cross-section.

In addition to these specific examples, I seek a general method to simulate transformation optics devices containing MM inclusions. I examine the discrete-dipole approximation (DDA) and its use in MM-TO design. DDA analysis reveals that cloaking performance is critically dependent on the lattice spacing between metamaterial elements: even a lattice of one-tenth the free-space wavelength degrades

cloaking performance such that the scattering cross-section of a four-wavelength diameter cloak is over 80% of the inscribed metal cylinder. Fortunately, it is possible to correct for some of the artifacts due to the nonzero lattice spacing. By calculating the Bloch index of an infinite magnetoelectric lattice, I determine polarizabilities that give the correct local index of refraction at all points in the cloak. For the same one-tenth wavelength lattice spacing and device size, this correction decreases the scattering cross-section to approximately 30%.

Finally, I examine so-called "complementary metamaterials" (C-MMs) and their utility in transformation optics devices. C-MMs exchange the void and metallized regions of conventional MM elements, and thereby offer a dual response to the electromagnetic field. This duality is attractive because it provides a straightforward method of creating broadband, highly-anisotropic magnetics. Using image theory and the concept fictitious magnetic currents, I analyze these elements and show that they may be incorporated into my discrete-dipole model. I simulate a simple nine-element array of these resonant apertures and compare to the same structure using commercial full-wave numerical software.

I have also examined the use of these complementary structures as elements for TO design. TO devices may be designed using a quasi-static interaction model for the effective response of the apertures, but that the interaction constant must be modified to account for the different interactions experienced by the apertures in a parallel plate waveguide. By incorporating this modification, a cloak could, in principle, be fashioned from C-MMs. However, C-MMs differ from regular MMs since they can couple the guided waves to free-space modes. I show that radiative loss may be mitigated by decreasing the lattice spacing, but the simulated cloak only shows cloaking, (normalized SCS less than one), for lattice spacings of $a \leqslant 0.08\lambda_0$.

To Stephanie. Thanks for waiting.

Contents

List of Figures

Acknowledgements

I would first like to thank my advisor, Prof. David R. Smith, for giving me the opportunity to pursue research in his group. I could not have hoped for a better environment to learn and develop my skills. Also, I would like to thank Prof. Smith for the enormous trust he has placed in me by allowing me to discover my own research interests and intellectual passions.

Additionally, I would like to thank the other members of the Center for Metamaterials and Integrated Plasmonics for their intellectual support and friendship. Stephané Larouche, Yaroslav Urzhumov, Jack Hunt, Guy Lipworth, Da Huang, and Yu-Ju Tsai have both assisted and challenged me intellectually in our collaborative efforts. I would also like to thank Guy Lipworth and Patrick Bowen specifically for their careful reading and feedback on this manuscript.

I would also like to thank my friends and family for their continued support through the PhD process. My parents- Marc and Barbara Landy -have continued to support me emotionally (and a bit financially!) through this long but rewarding process. Finally, I would like to thank my wife Stephanie. Not only has she endured for long years of physical separation, but she has provided invaluable copy-editing for this admittedly dry document.

1

Introduction

Conventional optical devices consist mainly of shaped dielectrics and metals. The trajectories of individual rays of light are altered via refraction and reflection at the boundaries of these homogeneous materials. The traditional optical design process is therefore reduced to finding materials with better optical responses and optimizing their surface contours for various applications. Gradient-Index (GRIN) devices introduce a new degree of freedom to the design process by incorporating inhomogeneous dielectrics. Ray trajectories are no longer restricted to straight lines inside GRIN elements, and can instead be gently curved by the gradient in the index of refraction.

In some sense, Transformation Optics (TO) is a generalization of GRIN design. Instead of simply specifying a gradient in the isotropic refractive index of a material, TO yields individual gradients in all tensor components in the electrical permittivity $\bar{\bar{\boldsymbol{\epsilon}}}$ and magnetic permeability $\bar{\bar{\boldsymbol{\mu}}}$. However, while traditional optical design is based on the short wavelength approximations of geometrical optics, TO is accurate to the level of the macroscopic Maxwell's equations, and has shown application even at zero frequency.

Unfortunately, like GRIN technology, the design freedom afforded by TO comes at the cost of complexity and extreme material parameters. In principle, these designs can be implemented with metamaterials (MMs) - composites that provide artificial material responses. In practice, however, metamaterials can add a host of complexities and restrictions to the design process. The complexity of the TO material prescription has continually forced researchers to make simplifying approximations in order to achieve any of the desired functionality, even when the dimensionality of the problem is reduced and the polarization is restricted.

Our goal in this dissertation is to provide a foundation for TO design with metamaterials. We present several methods of design and analysis that offer distinct benefits and disadvantages. Chapter 3 and Chapter 2.5 is based on the work done in [1], and discusses the applicability of quasiconformal mappings to TO design. We show, by virtue of example, the simplifications that quasi-conformal mappings bring to 3D TO design.

Chapter 3, based on the work from [2], describes the design and experimental characterization of a full-parameter microwave cloak of invisibility. In contrast to the lens of Chapter 2.5, this design replicates all the necesary material parameters specified by the TO algorithm. In this manner we are able to largely mitigate reflections in our device.

The remaining chapters are more general in scope in that we do not attempt to design a specific metamaterial geometry or device. Instead, we expand on the available tools to analyze and simulate metamaterial-enabled TO devices. Using a point-dipole approximation of metamaterial elements, we are able to simulate the impact of factors that force us out of the regime of homogenous materials. However, we show that some of these artifacts may be mitigated by introducing analytic corrections to the elements. We use these same tools in the analysis of complementary metamaterials, and we discuss the trade-offs of such elements in TO design.

In the remainder of this Introduction, we will briefly introduce the TO method. We also introduce some of the core concepts related to metamaterial design, as well as some of the challenges of trying to emulate the complicated material parameters required by TO.

1.1 Transformation Optics

The TO algorithm is predicated on the form invariance of Maxwell's Equations. Maxwell's Equations in a given space take the same form in different coordinate systems so long as the material tensors $\bar{\bar{\boldsymbol{\epsilon}}}$ and $\bar{\bar{\boldsymbol{\mu}}}$ are redefined to incorporate the effects of the coordinate transformation. A detailed derivation of this equivalence may be found in [3] and we will not reproduce it here.

Instead we will simply examine an application of this equivalence. Consider a transformation of the form $x^{i'} = x^{i'}(x^i)$. The stationary form of the material parameters is: [4]

$$\epsilon^{i'j'} = |A_i^{i'}|^{-1} A_i^{i'} A_j^{j'} \epsilon^{ij}, \tag{1.1}$$

where $A_i^{i'}$ is the Jacobian matrix of the transformation. A similar equation holds for $\bar{\bar{\boldsymbol{\mu}}}$. This fact is well known in the study of the formal structure of electromagnetics [5]. The traditional interpretation is that the transformed material parameters and the untransformed material parameters represent the same material but in different coordinate systems. However, in 2006, Pendry [6] made the conceptual leap to interpret the transformed material parameters as distinct materials in the original space. The transformed material distorts electromagnetic quantities such that they behave as if they were in the original, (virtual), space as viewed in the transformed, (physical), coordinates. These two interpretations may be called the topological and material interpretations, respectively [4].

In this Dissertation, we will restrict ourselves to orthogonal coordinate systems.

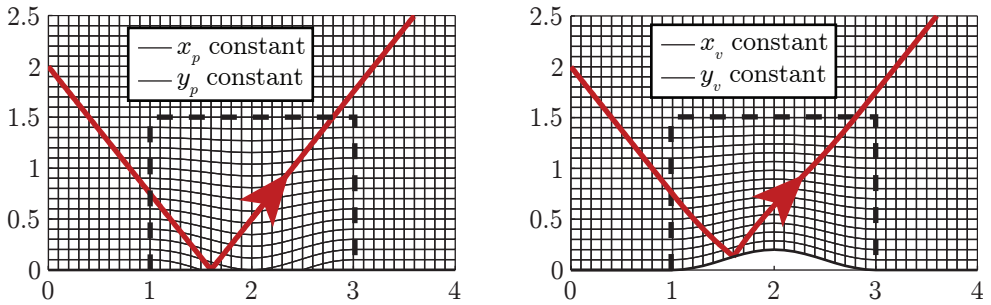

(a) Virtual Domain (b) Physical Domain

FIGURE 1.1: Ray trajectories distorted by a TO-prescribed Material

We therefore find it convenient to adopt the dyadic notation for Eq. 1.1:

$$\bar{\bar{\varepsilon}}' = \frac{\mathbf{\Lambda}\bar{\bar{\varepsilon}}\mathbf{\Lambda}^T}{|\mathbf{\Lambda}|}. \tag{1.2}$$

This notation will be used for the remainder of this work. As a concrete example of the method, consider the space shown in Fig. 1.1(a). This region consists of a vacuum bounded on the bottom by a perfect electric conductor (PEC). We call this the virtual domain, and label it with the subcript "v". The red line represents a ray that is reflected off of this PEC. We can find a coordinate transformation that maps this Cartesian space to a deformed one that produces a bump on the PEC (Fig. 1.1(b)). This is the physical domain, labeled with a "p". In the virtual space, we plot lines of constant x_p and y_p. When we move to the physical domain, we plot lines of constant x_v and y_v. In the physical domain, the ray trajectory appears deformed simply by virtue of the coordinate system we imposed on it. However, if we implement the material parameters from (1.1), we can force rays to follow this deformed trajectory. We have thus formed a type of electromagnetic cloak that is capable of concealing a perturbation under a conducting plane. This device is referred to both as a "ground-plane cloak" and "carpet cloak". We shall refer to it several times throughout this Dissertation.

Pendry's single insight therefore allows one to determine material prescriptions

that distort electromagnetic space in innumerable ways. However, the experimental realization of TO media has been hampered by a lack of naturally occurring materials that possess the necessary extreme and controllable dielectric and magnetic responses. In the next section, we will discuss metamaterials, which are able to circumvent some of the limits of natural materials.

1.2 Metamaterials

Our TO derived-devices require full control over $\bar{\bar{\boldsymbol{\varepsilon}}}$ and $\bar{\bar{\boldsymbol{\mu}}}$. However, Nature provides us with a very limited library of magneto-electric materials that provide the desired response and are also amenable to fabrication. Moreover, our devices typically require precisely controlled inhomogeneity and anisotropy, neither of which can be adjusted directly in a naturally-occurring medium.

We recognize that it is possible to create TO devices with naturally-occurring materials [7, 8]. We note, however, that this removes a number of degrees-of-freedom in design, and naturally restricts polarization. Therefore, the vast majority of experimentally-demonstrated TO devices have included artificial composites in their design [9, 10, 11, 12, 13, 14, 15, 16, 17, 18, 19, 20, 21, 22, 2]. These artificial composites are typically referred to as "metamaterials".

Unfortunately, the word "metamaterial" is not easy to define without considering several other related concepts. Consider the standard definition, according to Wikipedia:

> "Metamaterials are artificial materials engineered to have properties that may not be found in nature."

This definition is not particularly illuminating. It does, however, bring up a key concept: that of an artificial material. In this context, a material is a collection of microscopic entities, (i.e. atoms or molecules), that collectively respond to external stimulus such that the behavior of the aggregate may be encapsulated in a few

macroscopic parameters. In electromagnetics, materials are typically characterized by complex electrical permittivities and magnetic permeabilities.

In order to derive these quantities, we must introduce the process of averaging or homogenization to connect the detailed microscopic description of our system to our desired macroscopic definitions. This averaging process is usually performed over a suitable region in our system. For periodic arrangements of elements, this integration may be performed over a single unit cell.

This homogenization process, as well as the terms "microscopic" and "macroscopic," imply that there are length scales where the material definition is valid. These scales may differ quite a bit depending on physical aspects of the problem under consideration: a collection of particles may appear quite distinct to a high frequency acoustic waves and homogeneous to a low-frequency electromagnetic wave. Fortunately, the formal homogenization process reveals its own limitations, as we will show later in this Section.

We will attempt to clarify the term "metamaterial" by analyzing one in detail. Since we can not hope to describe all metamaterial elements that currently exist across multiple physical disciplines, we will restrict ourselves to a single examples related to electromagnetism. This analysis will uncover a number of important concepts in effective medium theory as well as some of the inherent limitations of electromagnetic metamaterial design. We therefore choose the split ring resonator [23, 24] due to its historical importance in the field and its use later in this dissertation. A split-ring resonator consists of a thin metallic wire or circuit board trace that has been bent to form a broken loop, as shown in Fig. 1.2. An incident electromagnetic wave will cause currents to flow and scattered fields to develop. We may determine the amplitude of these currents by developing a circuit model, as shown by [25]. We will begin our development in a similar manner.

The scattered fields appear to satisfy the Dirichlet boundary condtion on the

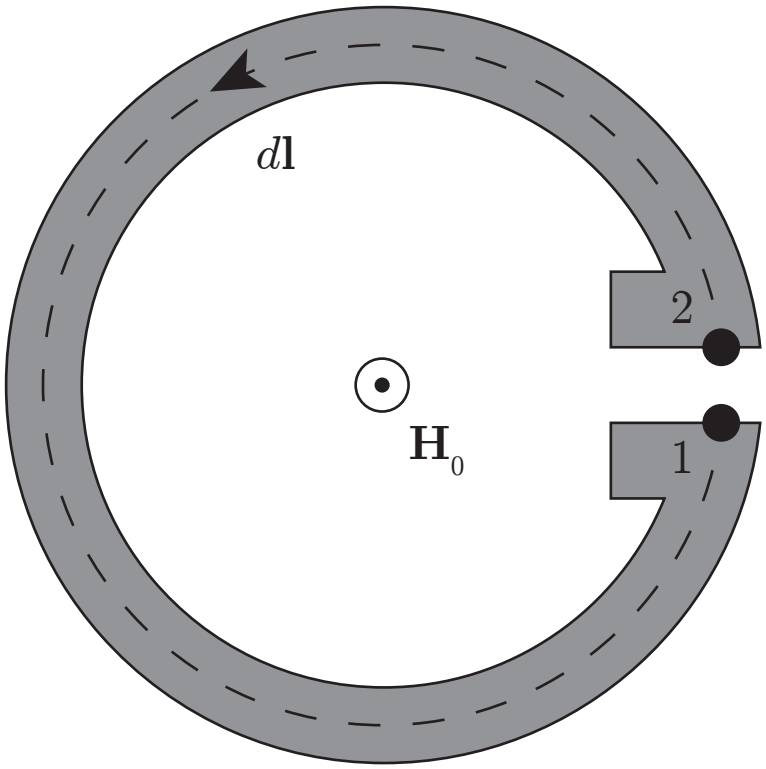

FIGURE 1.2: A diagram depicting a split-ring resonator.

conductor surface. Since $\nabla \cdot \mathbf{B} = 0$, $\mathbf{B}$ may be written as the curl of an auxilary vector potential $\mathbf{A}$ [26]. This boundary condition is therefore:

$$\mathbf{E}_0 + \mathbf{E}_s = \mathbf{E}_0 - \nabla\phi - j\omega A = 0, \tag{1.3}$$

In order to obtain a cause-and-effect relationship between the incident and scattered fields, we integrate along the contour shown in Fig. 1.2

$$\int \mathbf{E}_0 \cdot d\mathbf{l} = j\omega \int A \cdot d\mathbf{l} + \int \nabla\phi \cdot d\mathbf{l}. \tag{1.4}$$

The term on the LHS,

$$\int_1^2 \mathbf{E} \cdot d\mathbf{l}, \tag{1.5}$$

clearly represents a source for our equivalent circuit. We now assume that we can close the integral in E without effecting its solution, (meaning that the contribution from the gap is negligible). We can therefore use Faraday's law:

$$\nabla \times \mathbf{E} = -j\omega\mathbf{B} \tag{1.6}$$

combined with Stokes' theorem to find that Eq. 1.5 can be written:

$$\int \mathbf{E}_0 \cdot d\mathbf{l} = j\omega \int \mathbf{B}_0 \cdot d\mathbf{S}, \tag{1.7}$$

(i.e. the magnetic flux through the circuit induces an EMF that serves as the source). Immediately we see an ambiguity: we uncovered this source term by considering the imposed boundary conditions on the electric field only, yet we say that circuit is driven by the magnetic field. We note that at zero frequency, the time derivative of the magnetic flux is identically zero and therefore no current exists in our circuit. However, a natural magnetic medium would still show a response to a DC field. For this reason researchers often refer to artificial magnetism as second-order spatial dispersion; and the exciting field can either be thought of as a uniform B-field, or as a spatially-varying electric field. We highlight this equivalence because it presents an incomplete description of the problem. It does not consider the excitation effects of the uniform applied electric field, or other spatial derivatives of the applied electric field. For instance, the electric fields excite a quadrupole moment that contributes to the magnetic dipole moment in varying degrees as the orientation of the fields are changed [27, 28].

We assume that a uniform current I is driven through the loop except at the broken ends. Charge will build up in this gap according to the continuity equation:

$$\nabla \cdot \mathbf{J} = -j\omega\rho. \tag{1.8}$$

Happily, this azimuthal current gives us a magnetic dipole moment:

$$\mathbf{m} = \int \mathbf{r} \times \mathbf{J} dV = 2\pi R^2 I. \tag{1.9}$$

However, in order to determine the current explicitly, we must develop our model further.

Now consider the first term on the RHS of Eq. 1.4. Using Stokes' theorem and the definition of $\mathbf{A}$ and, we find:

$$j\omega \int \mathbf{A}_s \cdot d\mathbf{l} = j\omega \int B_s \cdot d\mathbf{S}. \tag{1.10}$$

Therefore, this term represents the magnetic flux that arises due to the induced currents, i.e. the inductance of the structure:

$$L = j\omega \frac{\int B_s \cdot d\mathbf{S}}{I}. \tag{1.11}$$

Unsurprisingly, the last term is the capacitance of the structure:

$$\int \nabla\phi \cdot d\mathbf{l} = \frac{Q}{C}, \tag{1.12}$$

so that the circuit is given by:

$$j\omega\Phi_m = j\omega LI - j\frac{1}{\omega C}. \tag{1.13}$$

We now have an explicit expression for I, and we can calculate m. However from the definition of the electric dipole moment:

$$\mathbf{p} = Q\mathbf{l}, \tag{1.14}$$

we see that the magnetic field induces an electric dipole moment as well [29]. This electric dipole stems from the charges deposited on the edge of the conductor in the

capacitve region, as indicated by Eq. 1.12. This is the hallmark of bianisotropy: an incident magnetic field creates an electric response and vice-versa. In such a medium, the constitutive relations are written:

$$\begin{aligned} \mathbf{D} &= \bar{\bar{\boldsymbol{\varepsilon}}} E + \bar{\bar{\boldsymbol{\kappa}}} H \\ \mathbf{B} &= \bar{\bar{\boldsymbol{\mu}}} H - \bar{\bar{\boldsymbol{\kappa}}}^T E. \end{aligned} \tag{1.15}$$

We see that a medium composed of SRRs will behave unexpectedly if this bianisotropic effect is not considered [29, 30]. This is critical for the design of TO-devices, since the formulation calls for purely anisotropic permittivities and permeabilities. Fortunately, careful MM design can mitigate-or even eliminate-the effect of bianisotropy [29, 9, 31].

Let us ignore the effects of bianisotropy for now. We have shown that an SRR provides us with a magnetic moment, which we assume is simply proportional to the field exciting the element:

$$m = \alpha H_0. \tag{1.16}$$

Now, in order to create our effective medium, we must array these SRRs in some fashion. Typically, split-rings are arrayed in a simple cubic lattice since this is the most amenable to planar fabrication. We now excite this array with a uniform magnetic field. When we do, we see that each element produces a dipole moment in response to the applied field. However, we note that these dipoles also produce magnetic fields of their own. Therefore, the field exciting these element consists of both the applied field and the fields from all the other elements. It may be shown that the local field exciting each differs from the average field by [32]:

$$< \mathbf{H} > - \mathbf{H}_{loc} = -\frac{\mathbf{P}}{3}. \tag{1.17}$$

We will investigate this phenomenon further in chapter 4. At this point we simply note that this adds another degree of complexity to our design, and 1.17 can differ

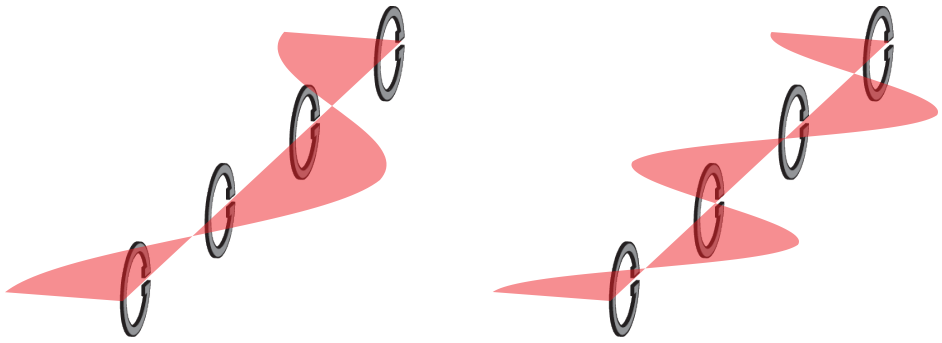

(a) Weak Spatial Dispersion (b) Strong Spatial Dispersion

FIGURE 1.3: Spatial Dispersion in an array of SRRs in a cubic lattice of period a

quite a bit depending on the layout of the array. We now increase the frequency of our applied field. As we do, the average magnetic fields in our medium become non-uniform due to the finite wavelength. As we continue to increase the frequency, the wavelength becomes shorter and shorter until the spatial variation of the wave is comparable to the spacing between SRRs, as shown in Fig. 1.3(a). At this point, our definition of an effective medium begins to break down. When we calculate the magnetization:

$$\mathbf{M} = \frac{1}{a^3}\int \mathbf{m}\left(\mathbf{r}\right) dV = \frac{1}{a^3}\mathbf{m}, \tag{1.18}$$

as expected. However, when we calculate the average field, we find [32, 33, 34]:

$$< \mathbf{H} >= \frac{1}{a^3}\int \mathbf{H}\left(\mathbf{r}'\right) dV = \mathbf{H}_0 \frac{\sin qa/2}{qa/2} + HOM. \tag{1.19}$$

If we were to calculate the average material properties in the cell, we would find an explicit dependence of μ on the wavenumber q in the system [33, 34]. Such is the consequence of averaging over a volume where there is a sinusoidal modulation to the magnetic and electric fields. This artifact becomes quite important at microwave

frequencies where the wavelength of light imposes a natural inhomogeneity in the system. However, this spatial dispersion can manifest due to any field gradient, and its effects can be quite deleterious for even highly sub-wavelength unit cells [35].

In Fig. 1.3(b), we have increased the operational frequency even further. The applied field now shows significant variation over the SRR itself, and our dipolar circuit model breaks down. In order to accurately model this system, we would be forced to consider fine structure of the currents in the SRR and how they contribute to multipoles of various orders [36]:

$$J_i = j\omega \left[a_{ij} E_j + a_{ijk} \left(\nabla_k E_j \right) + a_{ijkl} \left(\nabla_l \nabla_k E_k \right) ... \right] \tag{1.20}$$

If we continue in this fashion, our analysis will become increasingly cumbersome and cease to give us insight into the behavior of the array. We therefore stop at this point.

In the preceding analysis, we introduced a number of caveats to the material interpretation of an array of split-ring resonators. However, this should not discourage the prospective metamaterial designer. We cannot point to a specific element size or configuration and say that the material interpretation is invalid. Rather, the appropriateness of the material interpretation will depend on the particular circumstances of the system.

For our purposes, a "metamaterial" is purely a conceptual tool. By labeling something a metamaterial, we are saying we can use the concept of the device as a homogeneous material as a useful starting point for further analysis and design, i.e. the concept is enabling. This definition frees us from the stringent limitations imposed on a true effective medium, but it reminds us that we must remain cognizant of how our eventual device might differ from such a material.

2

Quasi-Conformal Mappings in Transformation Optics

In this chapter, based on [1], we examine quasiconformal mappings and their use in transformation optical design. By introducing a number of approximations, we show that these mappings allow us to design TO devices with greatly simplified material specifications. Using the TO method, we will examine the origin of aberrations that appear from our approximations, and we suggest avenues to mitigate them.

My specific contributions to this topic are as follow:

- I examine the quasi-conformal mapping technique and its application to transformation optics. I show that the all-dielectric implementations are inherently approximate and result in aberrations. I introduce a method to mitigate these aberrations by exploiting freedoms in the specification of the mapped domain.

- I extend the QCTO method to three dimensions. I show that the 3D-QCTO method is amenable to further approximations that reduce the complexity of the material mapping from six to three independent material parameters, thereby simplifying the conjoint MM design.

- I implement ray-tracing analysis to verify the performance of a QCTO-derived optic. I verify the performance trade-off for the reduced-parameter optic and the necessity of anisotropic TO design.

- I exploit the rotational symmetries of the optic to make full-wave simulation of the problem tractable. I verify that the reduced-parameter lens design offers superior performance to a dielectric-only implementation.

2.1 Conformal Mappings in Transformation Optics

The physical field distribution in a TO device is determined by the specific coordinate transformation that is used in turn to determine the distribution of constitutive parameters. In most instances, however, the field distribution within the volume of the device is of no consequence: only the fields on the boundaries of the device are relevant, since the function of most optical devices is to relate a set of output fields on one port or aperture to a set of input fields on another port or aperture. From the TO perspective, device functionality is determined by the properties of the coordinate transformation at the boundaries of the domain. Since there are an infinite number of transformations that have identical behavior on the boundary, there is considerable freedom to find a transformation that is "optimal" in the sense that it maximizes a desired quantity, such as isotropy. A useful derivation of this condition is found in [3, 37], which we reproduce here for completeness.

A coordinate transformation produces a mapping between points in two domains. The constitutive parameters that result from a general mapping can be determined from Eq. 1.2. It is instructive to restrict our attention to two-dimensional (2D) mappings of the form $\mathbf{x}' = [x'(x,y), y'(x,y)]$, for which the material transformation

tensors can be written:

$$\frac{\mathbf{A}\mathbf{A}^T}{|\mathbf{A}|} = \begin{bmatrix} x_x'^2 + x_y'^2 & x_x'y_x' + x_y'y_y' & 0 \\ x_x'y_x' + x_y'y_y' & y_x'^2 + y_y'^2 & 0 \\ 0 & 0 & 1 \end{bmatrix}. \tag{2.1}$$

For compactness, we indicate differentiation with respect to coordinates with a subscript. The 2D mapping is useful for configurations in which the fields are constrained to propagate within the plane, and are polarized so that either the electric or magnetic fields are transverse to the out-of-plane direction, (TE^z or TM^z, respectively in our coordinate system). Ideally, the constitutive tensors have only diagonal components, meaning we should impose an orthogonality condition $\varepsilon_x y = \varepsilon_y x = 0$. According to Eq. 2.1, this constraint implies:

$$x_x'y_x' = -x_y'y_y'. \tag{2.2}$$

Mappings that satisfy Eq. 2.2 will generally correspond to materials that are anisotropic in the plane, since $\varepsilon_{xx} \neq \varepsilon_{yy}$. Imposing this second constraint and using Eq. 2.2 we find that

$$\begin{aligned} x_x' &= y_y' \\ x_y' &= -y_x'. \end{aligned} \tag{2.3}$$

Thus, the result of requiring that the constitutive tensors be diagonal and that the medium be isotropic in the plane is that the Eqs. 2.3 must be satisfied; these are the well-known Cauchy-Riemann equations that define conformal maps.

Under a conformal map, the transformed coordinate system remains locally orthogonal, and angles formed by curves passing through a given point in one coordinate system are conserved in the transformed coordinate system. For conformal transformations, it can be seen from Eqs. 2.3 that the primed coordinates satisfy the vector form of Laplace's equation, or

$$\nabla^2 \mathbf{x}' = 0. \tag{2.4}$$

Conversely, any transformation that satisfies Eq. 2.4 everywhere will be conformal, so that Laplace's equation can be employed to obtain maps numerically. The constitutive parameters that correspond to conformal maps are much easier to implement than general TO media; to illustrate this explicitly, if we insert Eq. 2.3 into Eq. 2.1, we find that the constitutive parameters have the form:

$$\frac{\mathbf{A}\mathbf{A}^T}{|\mathbf{A}|} = \mathrm{Diag}\left[1, 1, |\mathbf{A}|^{-1}\right]. \tag{2.5}$$

TO media that are of the form of Eq. 2.5 are often described as "isotropic" and "dielectric-only"; however, the use of these terms with respect to Eq. 2.5 and conformal transformations requires some qualification. The in-plane components of the constitutive tensors corresponding to the conformal mapping are identically unity. Nevertheless, such a transformation can be implemented with isotropic dielectrics if the polarization of the fields is restricted in the medium. With this restriction in place, the incident field only "sees" the relevant material components. In this case, the full transformation could be obtained with an isotropic dielectric if the electric field is constrained to be parallel to the z-axis, (TM^z polarization). While explicitly solving the Cauchy-Riemann differential equations, (Eqs. 2.3), analytically to find conformal mappings may seem a challenge, it is straightforward to prove using complex analysis that any mapping between two sets of complex coordinates that can be written

$$z' = f(z), \tag{2.6}$$

where $z = x + iy$ and $z = x' + iy'$ will satisfy Eqs. 2.3. The use of complex analysis renders the effort of discovering conformal transformations a trivial matter; however, the limitations of conformal maps arise when we truncate our transformation domain. That is, once boundary conditions are applied to the governing differential equations, it is not always possible to achieve conformal modules equal to unity, and hence the

Cauchy-Riemann equations do not apply universally to all geometries.

2.2 Quasi-Conformal Transformations and the Quasi-Isotropic Approximation

The Riemann Mapping theorem states that any simply-connected domain may be conformally-mapped to the unit disk. In essence, it guarantees that we can find a conformal map between any two domains by mapping each of them to each other through a mapping to the unit disk. However, as we discussed previously, much of the power of TO is determined by the transformation at the boundary of the domain. For instance, we might require that our transformation does not introduce reflections or change the direction of a wave entering or exiting our transformed domain. These conditions introduce additional restrictions to our transformation [38]. The most straightforward way to satisfy these conditions is to stipulate that the coordinates are the same as free space on the boundary of our transformed domain, (Dirichlet boundary conditions). At the very least, we should require that each side of our physical region is mapped to the same corresponding boundary in the virtual domain. Mathematically, we assign a vertex to the intersection of each arc in our physical domain, as shown in Fig. 2.1. We then stipulate that each of these vertices is mapped to a corresponding vertex in the virtual domain.

This extra constraint severely limits the scope of conformally-equivalent domains. Specifically, once the sides of the quadrilateral domain have been specified, the region can only be mapped to another quadrilateral that shares the same conformal module. The conformal module (M) is simply the aspect ratio of the differential rectangle corresponding to a set of orthogonal coordinates. If the domain is rectangular, then M is the aspect ratio of the entire domain. Another concern relates to the boundary conditions directly. While Dirichlet boundaries are ideal for most purposes, they may be incompatible with our requirement of orthogonality at all points in the mapped

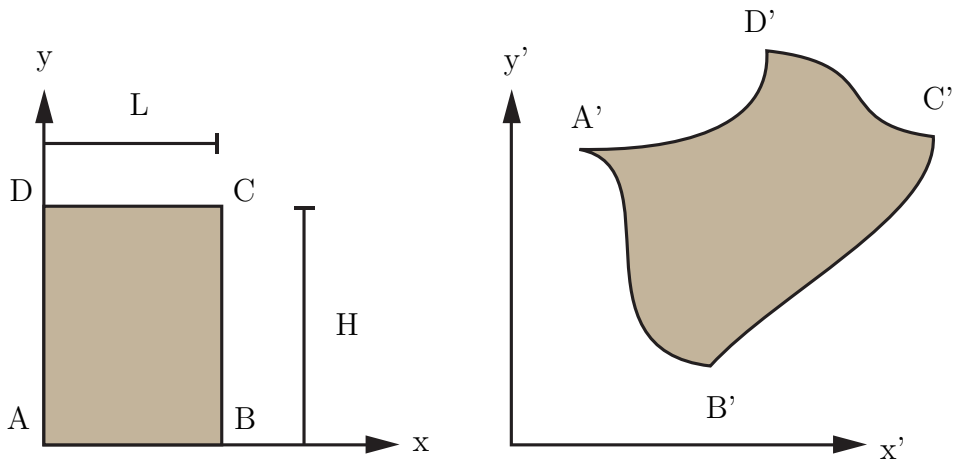

FIGURE 2.1: Mapping between a rectangle Q and a quadrilateral domain R. The generalized quadrilateral R consists of four Jordan arcs and represents the physical domain. The vertices (A, B, C, D) in Q are mapped to vertices (A, B, C, D) in R, as shown above.

domain. If we simultaneously specify $x'(x)$ and M at the boundary, the problem becomes over-determined and we are not guaranteed that the mapping will be orthogonal at the boundary [39]. Instead, we require a combination of Dirichlet and Neumann boundaries to simultaneously fix the geometry of the transformed domain and maintain orthogonality on the boundary. The Dirichlet component of the boundary conditions appear when we state that each arc in physical space corresponds to an edge in the virtual space, as shown Fig. 2.1. Formally, we state that

$$\begin{aligned} x = 0 \text{ on edge } D'A' \text{ and } x = L \text{ on edge } B'C' \\ y = 0 \text{ on edge } A'B' \text{ and } y = H \text{ on edge } C'D'. \end{aligned} \tag{2.7}$$

The Neumann component determines the position of the coordinate lines not specified by Eqs. 2.7 and guarantees orthogonality on the boundary. The orthogonality condition on the other boundaries may be rewritten

$$\begin{aligned} \nabla' x \cdot \hat{\mathbf{n}} = 0 \text{ on } y = 0, H \\ \nabla' y \cdot \hat{\mathbf{n}} = 0 \text{ on } x = 0, L \end{aligned} \tag{2.8}$$

where $\hat{\mathbf{n}}$ is the normal to the boundary curve. This formulation of the boundary

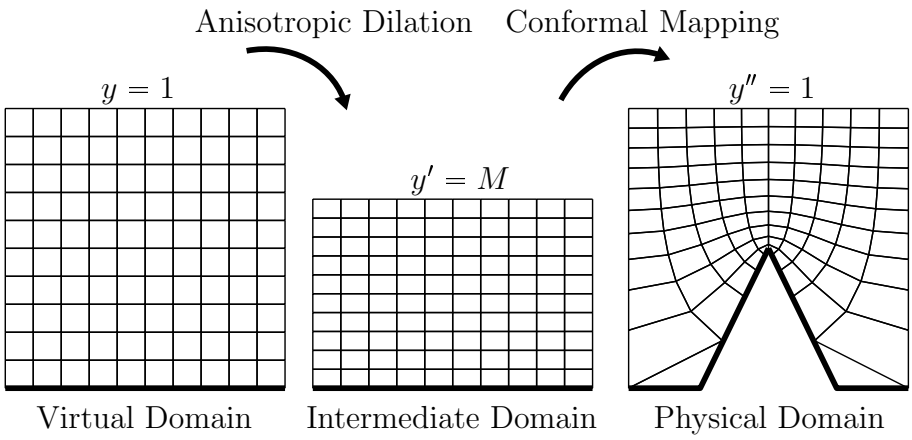

FIGURE 2.2: Depiction of the quasi-conformal mapping using intermediate transformations. Lines of constant x and y, (virtual domain coordinates), are shown in each domain. The thick black line represents a PEC boundary in each domain.

conditions in terms of gradients in the physical space will be useful for our numerical solution process later. The important thing to note at this point is that the Neumann boundary condition allows coordinate lines to slide along the boundary to ensure orthogonality. This deviates from the normal Dirichlet specification and aberrations may result depending on the severity of the deviation.

We now return to our discussion of the conformal module. What happens when two domains do not share the same conformal module? We can consider the effect via example using the tools of TO. We wish to map a given region of space onto a region that has a perturbation introduced, in this case a bump that protrudes into the domain from below, as shown on the right of the same figure. This configuration has become known as the carpet cloak, as we introduced in Section 1.1. If it is assumed that the lower boundary will correspond to a perfect electric conductor, then the mapping represents the design of a "cloak" that removes the effect of the perturbation from the reflecting surface [40]. For simplicity, we assume that the dimensions of the physical domain are one by one in arbitrary units. Note that the conformal modules for the two domains are not the same; for the case shown in Fig. 2.2, the

conformal module of the physical domain is approximately $M = 0.68$. We have intentionally made the physical domain distortion large to create a substantially different conformal module and aid in visualization of the process. To compensate for the mismatch in conformal modules, we first map our virtual domain to an intermediate domain having the same conformal module as the physical domain. The simplest way to do this is with a uniform dilation of the form $y' = My$. We can then conformally map this intermediate domain onto the physical domain with a conformal transformation, so that the functional dependence of the final transformed coordinates may be written $x'' = x''(x'(x))$. We can now consider the effect of the multiple transformations on the material parameters. The combined dilation and conformal mapping produce material tensors of the form:

$$\frac{\mathbf{A}\mathbf{A}^T}{|\mathbf{A}|} = \mathrm{Diag}\left[M^{-1}, M, (M|\mathbf{A}_c)\,|^{-1}\right] \tag{2.9}$$

where $\mathbf{A}_c$ is the Jacobian matrix of the conformal transformation between the intermediate and physical domains. For an assumed TM^z polarization, the conformal module provides an immediate measure of the anisotropy of the TO medium, as well as its required magnetic response, since $M = \sqrt{\mu_x/\mu_y}$. Written in terms of x and y, Eq. 2.3 becomes

$$Mx'_x = y'_y \tag{2.10a}$$

$$Mx'_y = -y'_x, \tag{2.10b}$$

so that equation 2.4 becomes

$$M^{-2}\mathbf{x}''_{xx} + \mathbf{x}''_{yy} = 0. \tag{2.11}$$

The solution to this vector equation is the quasi-conformal (QC) map. The QC map minimizes the anisotropy of mappings between domains of differing modules [40]. In general, there is no closed-form solution to equation 2.11, and it must be calculated

using a numerical approach. Historically, iterative methods [39, 41] are often used. Since M is not known a priori, it must be calculated at each solution step and inserted into the discretized governing equations. Alternatively, the domains may be approximated by polygons, and the mapping may be computed analytically via Schwarz-Christoffel transformations [42]. It is also possible to simply circumvent the issue of calculating M by reformulating the problem in terms of its inverse. Noting that the inverse of a conformal map is conformal, we can write:

$$Mx_{x'} = My_{y'} \tag{2.12a}$$

$$My_{x'} = -x_{y'}. \tag{2.12b}$$

Following the steps between equations 2.3 and 2.4, we find that we recover the vector Laplacian for the inverse problem:

$$\nabla'^2\mathbf{x} = 0. \tag{2.13}$$

Since the inverse mapping is independent of M, it behooves us to calculate the inverse mapping and use Eq. 2.13 to determine M in a single step. The forward transformation and material parameters can then be calculated in a post-processing step. This can be done iteratively, as before, or in a single step using PDE solution software based on the finite-element method [43]. We used the latter method for all the mappings shown. Explicitly, we solved Eq. 2.13 subject to the boundary conditions 2.7 and 2.8 in the physical domain using the commercial software suite COMSOL[1].

Returning to Eq. 2.9, we see that the cost of the QC map is immediately clear: the in-plane material tensors elements are no longer equal to each other. However,

[1] COMSOL is a multi-physics simulation suite based on the finite-element method (FEM). In addition to multiple physics models (e.g. electromagnetics), COMSOL allows the user to choose from a number of classical PDE models including Laplace's equation. COMSOL also allows the user to generate new physics models or modify existing templates; a feature we exploit in section 2.7.

it is generally the case that small deformations of space create small perturbations to the conformal module of the physical domain. Li and Pendry [40] suggested that the small anisotropy be ignored in this case. Specifically, if we define local indices of refraction along the principle axes of the transformation according to

$$n_x = \sqrt{\mu_y \varepsilon_z} \tag{2.14a}$$

$$n_y = \sqrt{\mu_x \varepsilon_z}, \tag{2.14b}$$

then geometric average of these quantities is simply

$$n = \sqrt{\varepsilon_z} = M|\mathbf{A}_c|^{-1}. \tag{2.15}$$

To implement this transformation without magnetic materials, we set the in-plane tensors components to unity and use Eq. 2.15 for the out-of-plane component. We see that the resulting material parameters are simply those of an isotropic in-plane dilation $\mathbf{x}'' = \sqrt{M}\mathbf{x}'$:

$$\frac{\mathbf{A}\mathbf{A}^T}{|\mathbf{A}|} = \text{Diag}\left[1, 1, M|\mathbf{A}_c^{-1}\right] \tag{2.16}$$

All of the limitations of the isotropic approximation can be understood in terms of these intermediate transformations. Instead of correcting the aspect ratio of the virtual domain through anisotropic stretching, we have simply isotropically dilated the virtual domain. This is shown schematically in Fig. 2.3. Assigning the physical domain a side length of one, we see that the virtual domain now has a horizontal extent of $M^{-1/2}$ and a vertical extent of $M^{1/2}$. The intermediate transformation uniformly dilates the virtual domain by another factor of $M^{1/2}$, and this region is then conformally mapped to the physical domain. Note that neither the aspect ratio nor the area of the virtual domain is the same as the physical domain.

We are now in a position to discuss the limitations of QC mapping compared with the general TO formulation. Any deviation from the strict TO prescription may result in a number of undesired wave propagation properties, or aberrations.

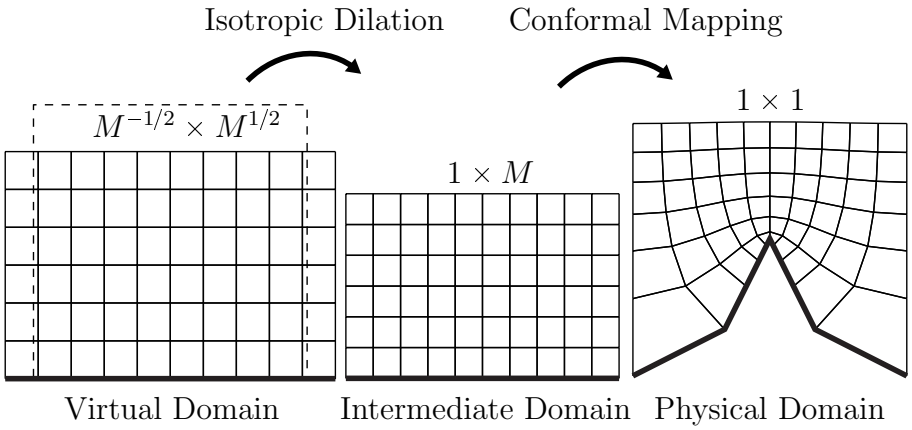

FIGURE 2.3: Depiction of the effective transformation when the anisotropy is neglected. The dimensions of each domain are shown on the top. The dashed square around the virtual domain depicts the desired domain size compared to the effective size.

Even when properly implemented with the anisotropic material properties of Eq. 2.9, the QC map requires Neumann boundary conditions that allow coordinate lines to "slip" along the boundary of the transformed domain. This can lead to aberrations, since the resulting material parameters are not those of free-space. In general, however, this type of error is small and can be mitigated by increasing the size of the transformation domain. We will see the effect of slipping quantitatively when we study a QCM-derived optic. A more significant problem arises from the isotropic approximation represented by the material prescription in Eq. 2.16. Since the virtual and physical domains are no longer the same size, the transformations no longer result in a strictly TO medium; instead, the resulting distributions of material parameters are only approximately correct, and will introduce a number of aberrations. The aberrations that result from the QC approximation will clearly depend on the severity of the transformation: larger deformations of space will inevitably result in larger changes in the module. However, even small changes in the module can disrupt the functionality of a QC device. It has been shown that carpet cloaks are always rendered visible when anisotropy is neglected, regardless of the size of the

perturbation [44].

Despite its limitations, the QC method has found many applications. For example, those aberrations that might be manifest in ray-tracing analyses [44] can be obscured when the device is on the order of the wavelength of operation so that diffractive effects dominate device behavior. This is a common situation at microwave frequencies, and the QC method may be applied to flatten conventional dielectric lens- and parabolic reflector- antennas without significant loss in performance [45, 46, 47]. Alternatively, the method can be used to reshape antenna radiation patterns by reshaping the boundary of a domain containing the antenna [48]. We could also attempt to mitigate aberrations introduced by the QC method by exploiting extra degrees of freedom that might exist in the design. For instance, as we have shown, the QC map is required when the conformal module of the physical and virtual domains are not the same. This situation is typically the case for the carpet cloak, whereby the boundaries of the cloak intercept free space on three sides of the domain. But there may be other cases where the boundary conditions are less severe. We will demonstrate how this can be used via example.

Consider a metallic waveguide operating in the TE10 mode, as shown in Fig. 2.4. Inserting a kink or a bend in this waveguide will, in general, cause reflections. We could use TO to map this distorted region to a straight one and restore performance [49, 50]. However, we note that there is some ambiguity when we define our transformation: how long is our virtual domain? Theoretically, we could choose any length we wanted and performance would be unchanged up to a phase shift in the wave exiting the transformed region. We may as well set the length of the virtual domain to be equal to the conformal module of our physical domain. When we do this, the transformation becomes strictly conformal and we may use a dielectric-only implementation without cost [51, 52]. The calculation is straightforward: we first calculate the QC map numerically using an arbitrary length virtual domain. We

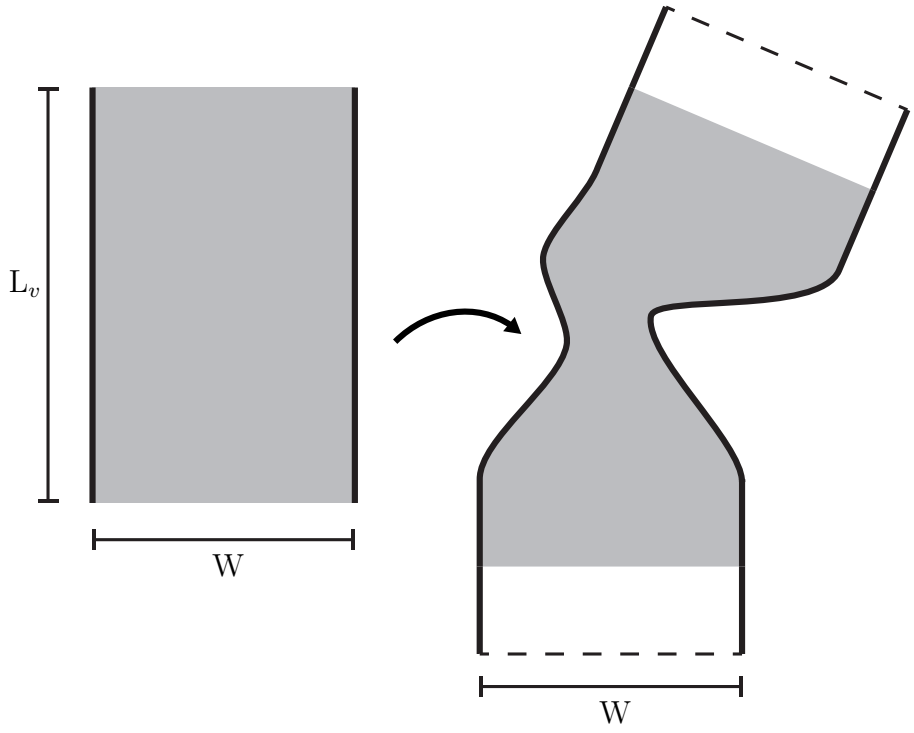

FIGURE 2.4: Conformal mapping applied to a waveguide bend. A rectangle is mapped to a distorted waveguide on the right. The height of the rectangle is chosen such that it shares the same conformal module as the bent domain.

can then calculate M according to Eq. 2.10. With this knowledge we simply make the substitution $dy \rightarrow Mdy$ to effectively scale our virtual domain. We will revisit this technique in Section 2.5 to help alleviate some of the aberrations that appear in optics modified with QCTO.

2.3 Quasi-Conformal Transformation Optics in 3D

We begin by considering a quasi-conformal transformation in the plane as depicted in Fig. 2.5, which we have determined using the tools of section 2.2. We will assume that the deformation of the module is negligible, ($M \approx 1$), or that we have scaled the virtual domain to enforce the conformal condition as discussed at the end of the last section. In part, the simplicity of the QCTO method arises from the reduced

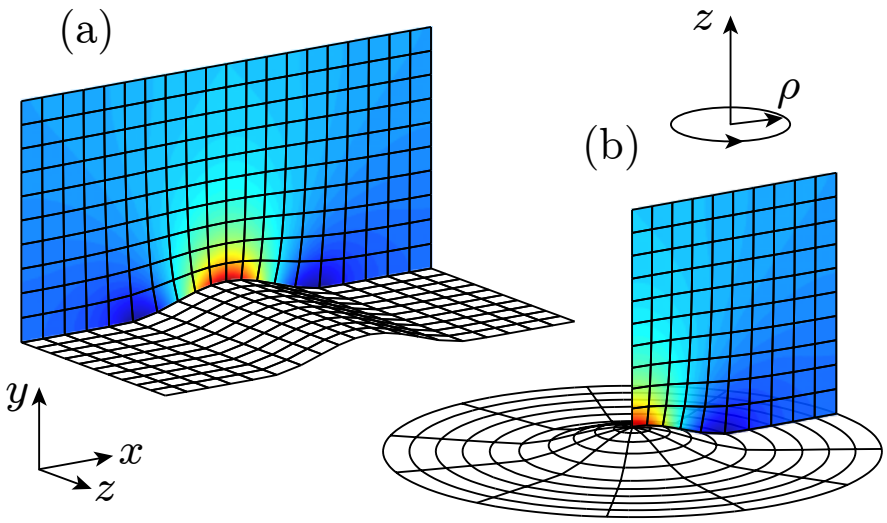

FIGURE 2.5: Depiction of the same quasi-conformal mapping in (a) Cartesian and (b) cylindrical coordinate systems.

dimensionality of the problem. The question then naturally arises: Can this simplicity be retained for other systems that exhibit some form of invariance? For instance, since many optical systems are rotationally symmetric about an optical axis, i.e. $\partial_\phi = 0$, it is natural to apply the conformal mapping procedure in the $\rho - z$ plane, as depicted conceptually in Fig. 2.5. This procedure is slightly more involved than the Cartesian case because of the complications of working in cylindrical coordinates [53]. We begin by considering our 2D mapping. Our coordinate transformation will be of the form:

$$\rho' = \rho'(\rho, z) \tag{2.17a}$$

$$\phi' = \phi \tag{2.17b}$$

$$z' = z'(\rho, z). \tag{2.17c}$$

The Jacobian of the coordinate transformation is then:

$$\mathbf{A}_c = \begin{bmatrix} \rho'_\rho & 0 & \rho'_z \\ 0 & 1 & 0 \\ z'_\rho & 0 & z'_z \end{bmatrix}. \tag{2.18}$$

Following the procedure in the last chapter and making the substitutions $x \to \rho$ and $y \to z$, we find the transformed material parameters derived from Eq. 1.2 have the form:

$$\frac{\mathbf{A}_c \mathbf{A}_c^T}{|\mathbf{A}_c|} = \text{Diag}\left[1, |\mathbf{A}_c|^{-1}, 1\right], \tag{2.19}$$

where $\mathbf{A}_c$ is now understood to be the Jacobian of the conformal transformation in the $\rho - z$ plane. While the material prescription is complete at this point, we pause to highlight a subtlety of working in non-Cartesian coordinate systems. The material parameters that we have derived are expressed in a coordinate basis. This is not the typical basis used to express physical quantities. To illustrate the complications this causes, consider the $\phi-$basis vector:

$$\phi = \rho^{-1} \left(\mathbf{x} \sin\phi - \mathbf{y} \cos\phi\right). \tag{2.20}$$

It is clear that ϕ is not normalized, implying that the material response of Eq. 2.19 will have a different physical meaning depending on its position in the mapped space. In particular, the in-plane components of Eq. 2.19 will require a non-vanishing response even though they are expressed as unity in this basis. However, Eq. 2.20 suggests that we can convert to a unit basis through the change-of-basis matrix:

$$\mathbf{A}_{cu} = \text{Diag}\left[1, \rho, 1\right], \tag{2.21}$$

and back to a coordinate basis with:

$$\mathbf{A}_{uc} = \mathbf{A}_{cu}^{-1} = \text{Diag}\left[1, \rho^{-1}, 1\right]. \tag{2.22}$$

To determine the resulting material parameters, we first use Eq. 2.22 to transform from the traditional unit basis into a cylindrical coordinate basis. In the coordinate basis, we perform our coordinate transformation with Eq. 2.19 and then return to

our, (now transformed), unit basis with Eq. 2.21. We can therefore express the total transformation operator as:

$$\mathbf{A}_T = \mathbf{A}_{cu}\mathbf{A}_c\mathbf{A}_{uc} \tag{2.23}$$

or

$$\mathbf{A}_T = \begin{bmatrix} \rho'_\rho & 0 & \rho'_z \\ 0 & \frac{\rho'}{\rho} & 0 \\ z'_\rho & 0 & z'_z \end{bmatrix}. \tag{2.24}$$

We now use Eq. 1.2 to find that the transformed material parameters are:

$$\frac{\mathbf{A}\mathbf{A}^T}{|\mathbf{A}|} = \text{Diag}\left[\frac{\rho'}{\rho}, \frac{\rho}{\rho'}\frac{1}{|\mathbf{A}_c|}, \frac{\rho'}{\rho}\right]. \tag{2.25}$$

As in the Cartesian case, the parameters are orthotropic; however, for the cylindrical case the in-plane tensor components are no longer those of free-space. The factor of ρ arises from the fact that the differential volume element in cylindrical coordinates is a function of ρ. The transformed material parameters must compensate for this extra dilation of space between the virtual and physical coordinates. Additionally, the material parameters are orthotropic in cylindrical coordinates, which means the principle axes are not constant but vary circumferentially. We have therefore not simplified our system by much, as we still require six material responses to implement this transformation, and we certainly cannot implement this transformation solely with a dielectric. However, as we shall see, this transformation is amenable to certain simplifying approximations.

2.4 Eikonal Approximations for Uniaxial Transformations

When the scale of electromagnetic inhomogeneity is substantially larger than the free-space wavelength, electromagnetic behavior is dominated by geometric optics.

In this regime, electromagnetic waves take the form of plane waves with spatially-varying phase contours. At each point in space, these waves obey a local dispersion equation that is equivalent to that of a homogeneous medium. We begin by discussing the dispersion relation for the azimuthally-uniaxial material of the previous section. Maxwell's Equations for time-harmonic fields take the usual form:

$$\nabla \times \mathbf{E} = j\omega\mu_0 \bar{\bar{\boldsymbol{\mu}}}_r \mathbf{H} \tag{2.26a}$$

$$\nabla \times \mathbf{H} = -j\omega\varepsilon_0 \bar{\bar{\boldsymbol{\varepsilon}}}_r \mathbf{E}. \tag{2.26b}$$

We make the assumption that the fields can be written:

$$\mathbf{E} = \mathbf{E}_0 e^{-jk_0\psi(\mathbf{r})} \tag{2.27a}$$

$$\mathbf{H} = \mathbf{H}_0 e^{-jk_0\psi(\mathbf{r})}. \tag{2.27b}$$

This is a "quasi-plane wave," where the spatial variation of phase is decoupled from that of the field amplitude. Inserting this form for the fields and making the definition $\mathbf{k} \equiv \nabla\psi$, we find Eq. 2.26 reduces to:

$$\mathbf{k} \times \mathbf{H}_0 - c_0\varepsilon_0 \bar{\bar{\boldsymbol{\varepsilon}}}_r \mathbf{E}_0 = j\frac{1}{k_0}\nabla \times \mathbf{H_0} \tag{2.28a}$$

$$\mathbf{k} \times \mathbf{E}_0 - c_0\mu_0 \bar{\bar{\boldsymbol{\mu}}}_r \mathbf{H}_0 = j\frac{1}{k_0}\nabla \times \mathbf{E_0}. \tag{2.28b}$$

Taking the limit $k_0 \to \infty$, the right hand side of Eqs. 2.28 go to zero and we recover the spectral form of Maxwell's Equations in a homogeneous medium. A more rigorous discussion of the applicability of this approximation is given in [54, 55] Combining Eqs. 2.28 in this limit yields:

$$\mathbf{k} \times \left[\bar{\bar{\boldsymbol{\mu}}}_r^{-1} (\mathbf{k} \times \mathbf{E}_0)\right] + \bar{\bar{\boldsymbol{\varepsilon}}}_r \mathbf{E}_0 = \mathbf{0}. \tag{2.29}$$

Making the definition $K_{ik} = \varepsilon_{ijk} k_j$, we can recast Eq. 2.29 as a matrix operation on the electric field:

$$\left(\mathbf{K}\bar{\bar{\boldsymbol{\mu}}}_r^{-1}\mathbf{K} + \bar{\bar{\boldsymbol{\varepsilon}}}_r\right)\mathbf{E}_0 = \mathbf{0}. \tag{2.30}$$

For a nontrivial solution to exist, Eq. 2.30 must have zero determinant. Enforcing this condition yields the local dispersion relation for our medium. In general, this task is complicated by the general anisotropy of $\bar{\bar{\boldsymbol{\varepsilon}}}$ and $\bar{\bar{\boldsymbol{\mu}}}$ [56], but it is greatly simplified in our case, where we constrain the material parameters to be uniaxial and share the same eigenbasis; i.e., of the form:

$$\bar{\bar{\boldsymbol{\mu}}}_r = \mathrm{Diag}\left[\mu_t, \mu_t, \mu_p\right] \tag{2.31a}$$

$$\bar{\bar{\boldsymbol{\varepsilon}}}_r = \mathrm{Diag}\left[\varepsilon_t, \varepsilon_t, \varepsilon_p\right]. \tag{2.31b}$$

The subscripts t and p refer to quantities transverse or parallel to the optical axis, (z or ϕ in the examples above). In a Cartesian basis, we find that the dispersion relation is a bi-quadratic equation that factors into two, (nominally independent), modes:

$$\left(\frac{k_x^2 + k_y^2}{\mu_t \varepsilon_z} + \frac{k_z^2}{\mu_t \varepsilon_t} - 1\right)\left(\frac{k_x^2 + k_y^2}{\mu_z \varepsilon_t} + \frac{k_z^2}{\mu_t \varepsilon_t} - 1\right) = 0. \tag{2.32}$$

Since our system is diagonal in a cylindrical basis, we convert to cylindrical coordinates in Eq. 2.32 by making the substitution $(x, y, z) \rightarrow (\rho, z, \phi)$ to find:

$$\left(\frac{k_\rho^2 + k_z^2}{\mu_t \varepsilon_\phi} + \frac{k_\phi^2}{\mu_t \varepsilon_t} - 1\right)\left(\frac{k_\rho^2 + k_z^2}{\mu_\phi \varepsilon_t} + \frac{k_\phi^2}{\mu_t \varepsilon_t} - 1\right) = 0. \tag{2.33}$$

It is important to emphasize that the components of $\mathbf{k}$ do not correspond to the solutions to Maxwell's equations in cylindrical coordinates. Rather, they are simply the projections of the Cartesian wave vector onto a cylindrical basis, i.e.,

$$\begin{aligned} k_\rho &= k_x \cos\phi + k_y \sin\phi \\ k_\phi &= k_y \cos\phi - k_x \sin\phi. \end{aligned} \tag{2.34}$$

These modes form uniaxial ellipsoidal surfaces in k-space that are equivalent to the extraordinary mode of a uniaxial dielectric. Unlike a uniaxial dielectric, however, there will not in general be an ordinary mode corresponding to anisotropic material. This form is only valid when two components of the constitutive tensors are equal in the eigenbasis of the material. For TO media, the TE and TM modes are identical since $\bar{\bar{\boldsymbol{\varepsilon}}}_r = \bar{\bar{\boldsymbol{\mu}}}_r$.

At this point, we note that the dispersion relation does not depend directly on the optical properties of the material. Rather, the relation is determined solely by the indices of refraction of the wave propagating along each of the principal axes of the material tensors. We label these unique indices

$$\begin{aligned} n_{t,TE} &= \sqrt{\varepsilon_p \mu_t} \\ n_{t,TM} &= \sqrt{\varepsilon_t \mu_p} \\ n_p &= \sqrt{\varepsilon_t \mu_t}, \end{aligned} \tag{2.35}$$

where the subscripts indicate whether the electric field (TE) or magnetic field (TM) is transverse to the optical axis. Since Eq. 2.35 only specifies these three parameters for the four unique components of $\boldsymbol{\varepsilon}$ and $\boldsymbol{\mu}$, we are free to specify one of these material components to be equal to an arbitrary value α if we make appropriate substitutions to the other components. For instance, if we set $\tilde{\mu}_t = \alpha$, then the other components become (in the cylindrical case):

$$\begin{aligned} \tilde{\epsilon}_t &= \frac{\varepsilon_t \mu_t}{\alpha} \\ \tilde{\epsilon}_t &= \frac{\varepsilon_\phi \mu_t}{\alpha} \\ \tilde{\mu}_\phi &= \alpha \frac{\mu_\phi}{\mu_t}. \end{aligned} \tag{2.36}$$

In order to minimize the number of magnetic elements in our eventual design, we should choose $\alpha = 1$. This flexibility is general to uniaxial magneto-dielectric media,

but for our TO-derived design, this approximation also retains the degeneracy of the dispersion relation so that waves of both polarizations follow the same trajectory in the medium.

The above procedure illustrates the great benefit of the QC method for 3D TO. While the material parameters derived directly from the TO algorithm are not particularly simple, (three required magnetic responses), the symmetries of the mapping permit us to make a subsequent approximation that greatly reduces the complexity of the problem, (one required magnetic response) [57].

At this point, we have introduced a number of approximations to the general TO specification. In the next section, we will test these approximations when we apply this methodology to the design of a high-performance lens. Since lenses have well-defined metrics of performance, we can discern the effectiveness of the QC mappings as well as our material approximations by evaluating the performance of these lenses. We will use a variety of numerical techniques to judge the effectiveness of these lenses.

2.5 Transformation Optics for 3D Devices: Reshaping the Luneburg Lens

This section applies the methods of Chapter 2 to the design of a specific device. Based on [2], this chapter discusses a TO-modified lens that promises near-perfect imaging characteristics with only one magnetic response. Using this lens, we examine the approximations that we introduced in the last chapter using several complementary methods of analysis.

While the carpet cloak provides a good platform to demonstrate the functionality and simplicity of the quasi-conformal technique, it is not very interesting from an applications standpoint. Fortunately, other proposed TO designs are amenable to QC optimization. One of the more compelling of these designs is the modified Luneburg lens proposed by Schurig [53]. The Luneburg lens is one implementation of

a family of spherically symmetric gradient index lenses that perfectly focuses images of concentric spherical surfaces onto one another in the geometric optics limit. Typically, the radius of one of these spheres is taken to infinity so that parallel rays are imaged to points on the surface of the lens. The most well-known, (and simplest), index distribution was derived by the eponymous Luneburg in 1944 [58]:

$$n\left(r\right) = \sqrt{2 - \left(\frac{r}{a}\right)^2}, \tag{2.37}$$

where n is index of refraction, r is the radial coordinate, and a is the radius of the lens.

While the Luneburg lens can produce a perfect image, it has the key disadvantage that the image is spread over a spherical surface: any attempt to image onto a planar surface-as would be needed for most detector arrays-would result in extreme field curvature aberration. Schurig demonstrated that TO could be used to map a portion of the spherical image surface onto a flat one, thereby creating a flat focal plane without introducing any aberrations. Schurig's proposed transformation exhibited all of the aforementioned limitations of MM-enabled TO design, in particular requiring both anisotropic permittivity and permeability with relatively extreme ranges of values.

Given its advantages for imaging, the Luneburg lens represents a useful challenge for QC techniques, since an all-dielectric implementation could serve as a superior optical device. Kundtz and Smith [59] made use of a transformation similar to the one illustrated in Fig. 2.6, in which the virtual space consists of the unperturbed Luneburg lens index distribution. In this 2D realization of the Luneburg, it is desired that the physical space be a quadrilateral, with one side corresponding to the flattened Luneburg. The virtual space is then distorted, bounded on the top, left, and right by straight lines, while the lower boundary is conformal to the curve of the lens, as shown in Fig. 2.6a. The index distribution of the Luneburg is then inserted

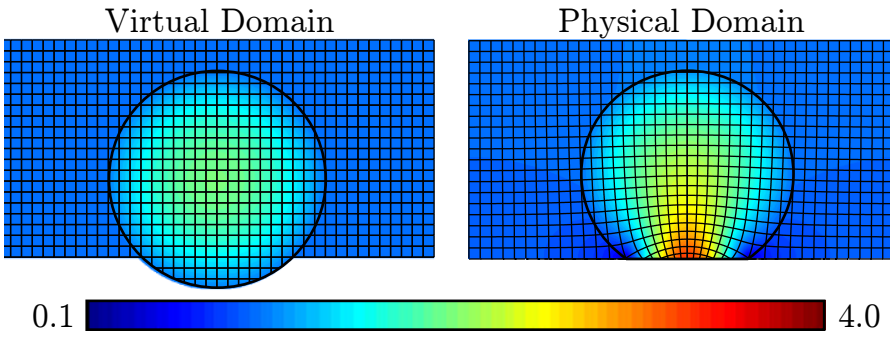

FIGURE 2.6: Depiction of the QC transform for the Luneburg lens flattened for a ninety degree field-of-view in 2D. The black line indicates the extent of the lens in the mapped regions. (left) Virtual domain lens geometry showing lines of constant x and y and the Luneburg dielectric distribution. (right) Physical domain geometry showing lines of constant x and y and the transformed dielectric distribution. The scale bar on the bottom indicates the color scaling of the dielectric.

into the virtual space, where it multiplies the QCTO material distribution, and the inverse transformation is used to flatten the Luneburg. Since it is assumed that a detector will terminate the fields on the flattened side, the same "slipping" boundary conditions can be applied on the lower edge as were used for the carpet cloak, and Eq. 2.13 solved to determine the QC grid[2]. This same "flattening" procedure may be applied to other GRIN devices, such as the Maxwell fisheye lens [19], and can also be used as a method to correct field curvature in conventional optical systems [37].

The first implementation of the flattened Luneburg was performed at microwave frequencies using cut-wire dipoles to achieve the desired gradient index structure [59]. Recently, a similar design has been demonstrated in the infrared [20], showing the versatility of the QCTO technique. While possibly of use for planar, chip-scale devices, the 2D lens has limited utility. An initial approach to extend the QCTO methodology to three dimensions was to take the 2D dielectric distribution from a QC transformation and revolve it around an axis of symmetry [14, 15]. However,

[2] Rigorously, the slipping boundary condition should be applied to all boundaries as specified in the last section. However, there is little practical difference between this and Dirichlet boundary conditions on the boundaries that are removed from the perturbation.

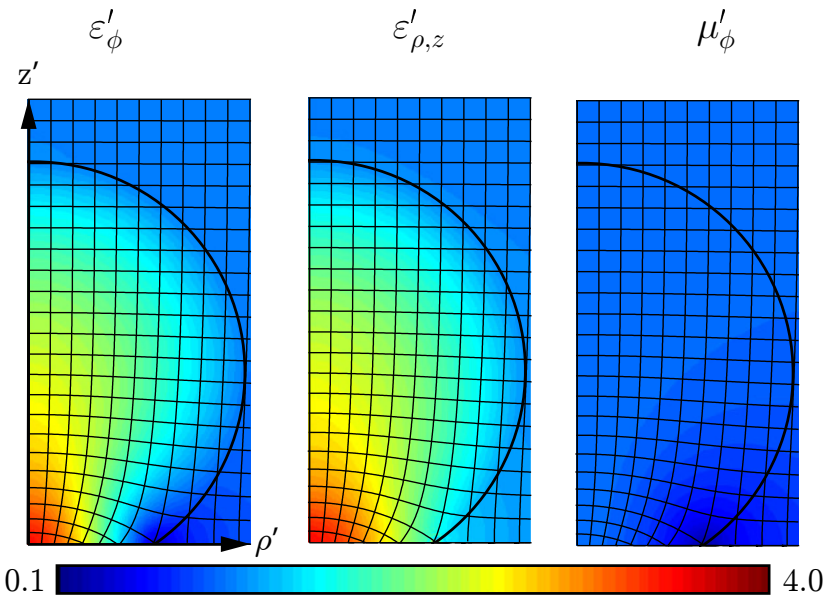

FIGURE 2.7: Reduced-Parameter material distribution for a flattened Luneburg lens. The other two components of $\boldsymbol{\mu}$' (not shown) are unity.

as we show in subsequent sections, this method does not produce a medium that corresponds to the correct transformed material parameters, and such a lens will suffer additional aberrations.

Rather, we will use the approximation developed in section 6.4 to design a reduced-parameter implementation of the lens. This approximation is especially appropriate for the transformed Luneburg lens, since the original dielectric distribution was derived under geometric optics considerations [58]. Fig. 2.7 shows the material parameters for a lens with the same degree of flattening as Fig. 2.6. In the following sections, we will compare this approximation with the full-parameter design and an isotropic-only variant.

2.6 The Hamiltonian Method

Ray-tracing is a useful tool for optically-large problems in which diffraction effects may be ignored. Additionally, ray-tracing may be formulated in the language of Hamiltonian optics, and it may be possible to glean some insight into the perfor-

mance of devices based upon the symmetries that they might possess. We begin by considering each ray of light as a particle that follows a trajectory that satisfies the Hamiltonian

$$H\left(p_i, q_i\right) = 0. \tag{2.38}$$

The parameterized ray trajectory $\mathbf{q}\left(\tau\right)$ is found by numerically integrating Hamilton's equations:

$$\dot{q}_i = \frac{\partial H}{\partial p_i}, \tag{2.39a}$$

$$\dot{p}_i = \frac{\partial H}{\partial q_i}. \tag{2.39b}$$

In Cartesian coordinates, the Hamiltonian is simply the local dispersion relation, and the conjugate momenta are simply the components of the normalized wave-vector k. Straightforward algorithms exist for ray-tracing in general impedance-matched media [4] and uniaxial media specifically [54]. However, we wish to exploit the symmetry of our system by performing our integration in cylindrical coordinates. We accomplish this by finding the Hamiltonian that preserves the form of Hamilton's equation [60]:

$$H = \frac{p_\rho^2 + p_z^2}{n_t^2} + \frac{p_\phi^2}{\rho^2 n_\phi^2}, \tag{2.40}$$

where we have used the indices of refraction along the principle axes of the material as defined by Eq. 2.33 and assumed degeneracy in the dispersion relation. This form of the Hamiltonian is important for two reasons. From Hamilton's equations we see that the coordinates are cyclic in the coordinate ϕ:

$$\dot{p}_\phi = -\frac{\partial H}{\partial \phi} = 0 \tag{2.41}$$

so that p_ϕ is conserved along a ray. This implies that we can categorize rays based upon their initial angular momentum. Rays with zero angular momentum $p_\phi\left(\tau\right)$

obey a reduced Hamiltonian of the form

$$H = \frac{p_\rho^2 + p_z^2}{n_t^2}, \tag{2.42}$$

which is simply the Hamiltonian of a ray in an axially-symmetric isotropic medium. The implication here is that the flattened Luneburg lens can be properly implemented with an isotropic dielectric only at normal incidence.

Extreme care must be taken in the numerical integration of Eqs. 2.39, since the mapping itself is determined numerically. In the absence of a closed-form solution for the mapping, we must rely on an intelligent interpolation scheme to retrieve the material values and their spatial derivatives as required by Eq. 2.39. Fortunately, COMSOL provides us with the spatial derivatives of all solved quantities. However, these are derivatives in the virtual domain, and we require them in the physical domain for our ray-tracing. From the chain rule, we see that

$$\partial_{i'} = \left(\partial_{i'} x^i\right) \partial_i = \mathbf{A} \partial_i. \tag{2.43}$$

With these quantities calculated on a regular grid, we can then use Hermite-cubic interpolation [61] to determine these quantities anywhere to high precision. We expect even higher accuracy could be achieved by using the same mesh and interpolation functions that are used internally by COMSOL.

In our study, we considered four distinct lenses based on two different transformations. The first transformation is based on the traditional QC mapping where the conformal module between domains is not preserved. The second transformation is based on the conformal (C) mapping where we have adjusted the height of the virtual domain to preserve the conformal module. From each of these transformation we construct two different lenses: one anisotropic, based on the proper transformed material equations, and one isotropic, which mimics the proper material parameters at zero field angle as shown by Eq. 2.42.

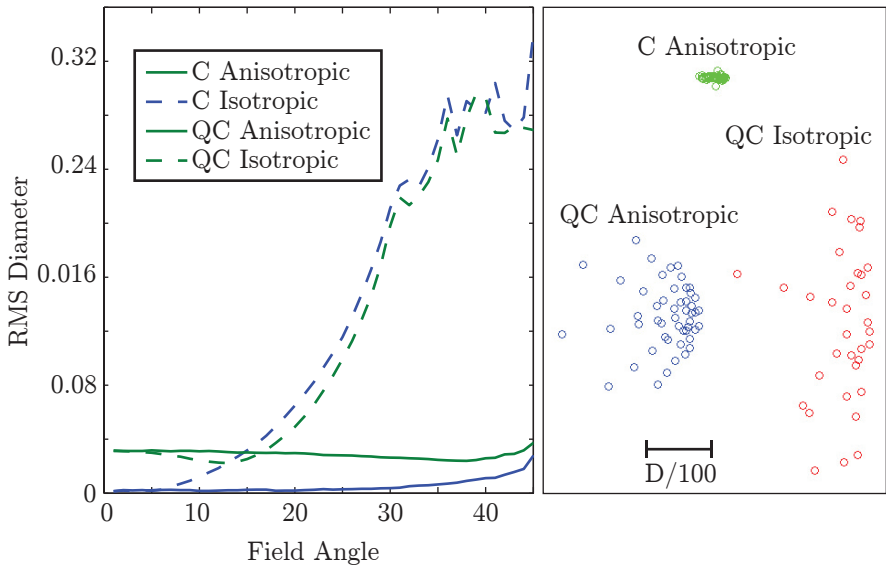

FIGURE 2.8: (Left) Spot Size comparison of various flattened Luneburg lenses calculated with numerical ray-tracing. The spot size at each angle is the RMS average of 100 incident rays. (Right) Spot diagrams at 30°.

Fig. 2.8 shows the root-mean-square (RMS) spot size for four different lens constructions: C isotropic and anisotropic, and QC isotropic and anisotropic. At normal incidence, (zero field angle), $p_\phi = 0$ and the ray paths for the anisotropic and isotropic lenses are degenerate. However, aberrations do appear in the lenses derived from the QC mapping. These aberrations are related to our omission of in-plane anisotropy, as discussed in Section 2.2. At normal incidence, all the rays pierce the top boundary of the cylindrical transformation domain without refractive aberration since $\hat{\mathbf{n}} \times \mathbf{k} = 0$. Therefore, we can ignore the slight material inhomogeneity at this boundary, as well as the isotropic scaling that occurs in the quasi-conformal approximation. However, we cannot neglect the error induced by neglecting anisotropy. As we showed previously, the material anisotropy allowed us to stretch the mapped region to fit in the transformation domain. Without this stretching transformation, the Luneburg lens is no longer circular in the virtual domain. Instead, it will appear compressed along one axis. This leads to the non-vanishing spot at zero field angle.

Up to approximately 5°, the isotropic lens configurations are essentially identical to their anisotropic counterparts. However, we see that the isotropic lens performance drops dramatically for larger field angles. By comparison, the anisotropic lenses show consistent performance across the specified field of view. The conformally-mapped lens shows the smallest spot size ($D_{spot} < 0.03D_{lens}$) up to about 44°. At this point, a significant number of rays are now intercepting the domain from the side where the mismatch has been increased by scaling the virtual domain. This aberration could be reduced by increasing the lateral extent of the transformation domain, but this would have the unwanted effect of increasing the size of the optic.

The isotropic variants of lenses clearly show the largest aberrations for large field angles. At 44°, the isotropic variants have spot sizes of $0.27D_{lens}$ and $0.33D_{lens}$ for the C and QC mappings, respectively. We can visualize the source of these aberrations by plotting the ray trajectories for anisotropic and isotropic lens variants as shown in Fig. 2.9. Rays that lie in the plane of the chief ray and the optical axis, (meridional rays), are focused identically in both cases, as these are the rays with zero angular momentum. However, we see a dramatic difference in performance when we plot rays in an orthogonal plane that contains the chief ray. This is the sagittal plane, and these rays have maximum angular momentum. Only the anisotropic lens properly focuses in this case. Sagittal rays in the isotropic case appear to be focused to a point above the nominal focal plane so that the lens exhibits astigmatism. Similar results were shown qualitatively in [57] for all three lenses and in [21] for the isotropic case.

We can connect these results to those of traditional optical lens design by calculating the optical path difference (OPD) for our rays. The optical path length (OPL) is simply the change in the eikonal across the path of each ray. From the definition of the eikonal, we then have:

$$OPL = \psi(\mathbf{r_1}) - \psi(\mathbf{r_0}) = \int_{\mathbf{r_0}}^{\mathbf{r_1}} \mathbf{k} \cdot d\mathbf{l}. \tag{2.44}$$

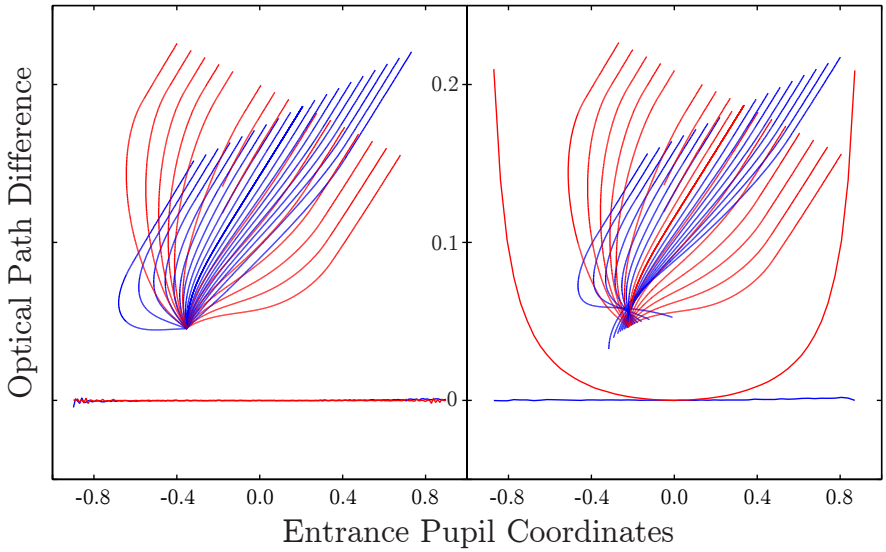

FIGURE 2.9: (Left) : OPD plots across the sagittal and meridional planes an anisotropic (left) and isotropic (right) lens. Insets are traces of rays in the meridional plane and sagittal plane. The sagittal rays and OPD are red, and the meridional rays and OPD are blue.

The OPD is calculated by subtracting the OPL of the chief ray from the OPL of all other rays. The OPD is plotted in Fig. 2.9 for both sagittal and tangential rays. As expected, the meridional rays have virtually no OPD in either case. However the sagittal rays in the isotropic case show an OPD plot that is symmetric about the optical axis. This is indicative of astigmatism, as previously mentioned. Similar ray-tracing analysis may be performed for the carpet cloak [62]. Unsurprisingly, the revolved, all-dielectric implementation of the cloak fails to operate effectively at all angles of incidence. Interestingly, an extruded version of the all-dielectric carpet cloak appears to mitigate these aberrations to some extent [62, 63]. However, this technique may have some application, especially in designs with restricted incident angles. For instance, alternative cloaking designs such as the conformal map introduced by Leonhardt [64] are only designed to work at one angle of incidence. If this structure is revolved around the axis parallel to this angle, performance is not diminished, as

shown in [65].

2.7 Full-Wave Verification of Eikonal-Limit Design

Ray-tracing is strictly valid only in the limit of vanishing wavelength. However, lenses are often used in situations where the aperture is only a few wavelengths across. In this regime, diffractive effects must be considered explicitly. Various models, (physical optics, geometrical theory of diffraction), can account for these effects with increasing accuracy, but, to our knowledge, only full-wave numerical solvers can handle these effects in conjunction with the complicated gradients and anisotropy of TO-derived materials. Full-wave simulations also allow us to test the effects of the eikonal approximation that we made to the transformation.

The full-wave simulation of optically-large, 3D objects is a formidable task. For example, the finite-element method (FEM) requires at least a few nodal points per wavelength to resolve gradients in electromagnetic fields. Memory requirements thus scale with the volume of the simulation domain. Fortunately, these requirements can be drastically reduced for problems with azimuthal invariance, such as the lens considered above. We first expand the fields in a Fourier series in ϕ:

$$\begin{aligned} E(\mathbf{r}) &= \sum_{m=-\infty}^{\infty} E_m(\rho, z)\, e^{jm\phi} \\ H(\mathbf{r}) &= \sum_{m=-\infty}^{\infty} H_m(\rho, z)\, e^{jm\phi}. \end{aligned} \tag{2.45}$$

The orthogonality of the series permits us to solve for the fields associated with each mode individually. Moreover, we can make the substitution $\partial_\phi \rightarrow jm$ in Maxwell's equations so that the problem is reduced to finding the 2D field pattern for each mode. This allows us to solve M small 2D problems sequentially instead of one large one.

To simulate a plane wave incident on the lens, we decompose the incident fields as in Eqs. 2.45. The decomposition is facilitated by the introduction of the auxiliary vector potentials A and F to represent the two distinct polarizations of the incident wave, (TM^z and TE^z, respectively) [26]. For instance, an incident wave making an angle θ_0 from the z-axis with the electric field polarized in $\mathbf{y}$ may be expressed as:

$$E_\rho = -\frac{E_0}{k_0 \rho \sin\theta_0} \sum_{m=-\infty}^{\infty} j^{1-m} J_m\left(k\rho\right) e^{jm\phi} \tag{2.46a}$$

$$E_\phi = E_0 e^{jk_0\rho\cos\theta_0} \sum_{m=-\infty}^{\infty} J'_m\left(k\rho\right) e^{jm\phi} \tag{2.46b}$$

where the prime ($'$) indicates differentiation with respect to the argument. In practice, the series must be truncated at some maximal wavenumber M. From the asymptotic form of Bessel functions, the series may be truncated without significant error when [66]:

$$M = \text{Ceil}\left(k_0\rho\sin\theta_0\right) + 6, \tag{2.47}$$

where ceil[] is the integer ceiling operator. With these tools in place, we can now investigate the performance of our lenses. For each lens, we simulate an incident plane at 30° off-normal for apertures ranging from five to thirty wavelengths in diameter. Our performance metric is the spot size that encompasses 84% of the energy in the focal plane, the same amount of energy contained in the primary lobe of a non-aberrated Airy disk. This metric enables quick comparison between our lenses and the expected diffraction-limited performance of a lens with the same aperture and focal length.

In our study, we looked at three lenses derived from the same conformal transformation[3]. The first lens uses the full-parameter implementation given by Eq. 1.2.

[3] Unlike our ray-tracing analysis, we found no significant difference between the strictly conformal- and the quasi-conformal mapped-lenses since the RMS spot size of both lenses lies below the diffraction limit in the simulated range of aperture sizes.

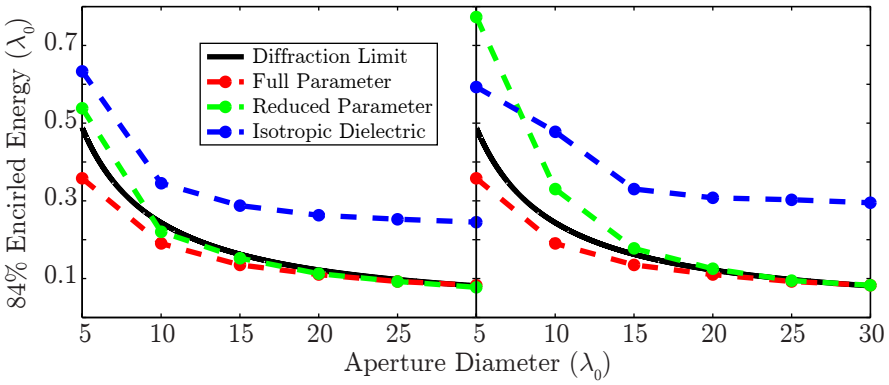

FIGURE 2.10: Comparison of spot sizes for various lenses using FEM.

For this case, we also set the virtual-domain Luneburg material distribution to be

$$\mu_r = \epsilon_r = \sqrt{2 - \left(\frac{r}{a}\right)^2}, \tag{2.48}$$

so that the lens performance is identical for both polarizations of the incident wave. The second lens uses the eikonal approximation of Eq. 2.36. As opposed to the first lens, the Luneburg distribution is mostly dielectric so as to maintain the minimum amount of magnetic coupling in the design. Since this design is based on a high frequency approximation, we expect inferior performance as compared to the full transformation for small apertures, and then we expect it to asymptotically approach the performance of the full transformation as the aperture size is increased. Additionally, we expect some difference in performance for the two polarizations of the incident wave. The final lens represents an isotropic, dielectric-only implementation. Since this implementation neglects the anisotropy of the transformation, we expect it to show the worst performance for all aperture sizes. Additionally, we expect the spot size to asymptote to the nonzero value corresponding to the RMS size given by the ray-tracing analysis of the previous section.

We note that these simulations numerically solve the full vector form of Maxwell's equations. It is important to consider the full vector fields when determining spot-

size since high-numerical aperture lenses can show significant longitudinal fields in the focal region [67]. We therefore calculate the intensity as a function of postion $\mathbf{r}$ directly from normal component of the time-averaged Poynting vector:

$$S(\mathbf{r}) = \frac{1}{2}\mathbf{E}(\mathbf{r}) \times \mathbf{H}^*(\mathbf{r}). \tag{2.49}$$

The simulation results are plotted in Figure 2.10. For comparison, we also plot the expected diffraction-limited spot diameter, given by

$$D = 2.44\lambda f/\#, \tag{2.50}$$

where $f/\# = f/D = 1/2$ is the f-number of the untransformed Luneburg lens. As expected, the full-parameter lens shows superior performance for all simulated aperture sizes. In fact, the spot size is a bit smaller than one would expect from Eq. 2.50, though both curves show the same behavior at short wavelengths.

At long wavelengths, the reduced-parameter and isotropic lenses have substantially degraded performance in comparison to the full-parameter implementation. For instance, the TE spot-size diameters for the isotropic and reduced parameter lens are 63.3% and 53.8% of the lens diameter, respectively, whereas the spot size of the full-parameter lens is 31.5%. However, the reduced-parameter implementation quickly regains performance as the aperture size is increased, so that by the time $D = 25\lambda$, the reduced parameter curve is practically indistinguishable from the full-parameter curve (9.26%, for both). On the other hand, the performance of the isotropic curve quickly asymptotes to a non-zero value as predicted by our previous ray-tracing analysis (25.3%).

Lens performance in the five- to ten-wavelength range is difficult to understand since the scale of material variation is on the order of the free-space wavelength. From simulations, it appears that main performance limiting factor is reflections in the lens interior where the material variations are the most rapid; these reflections

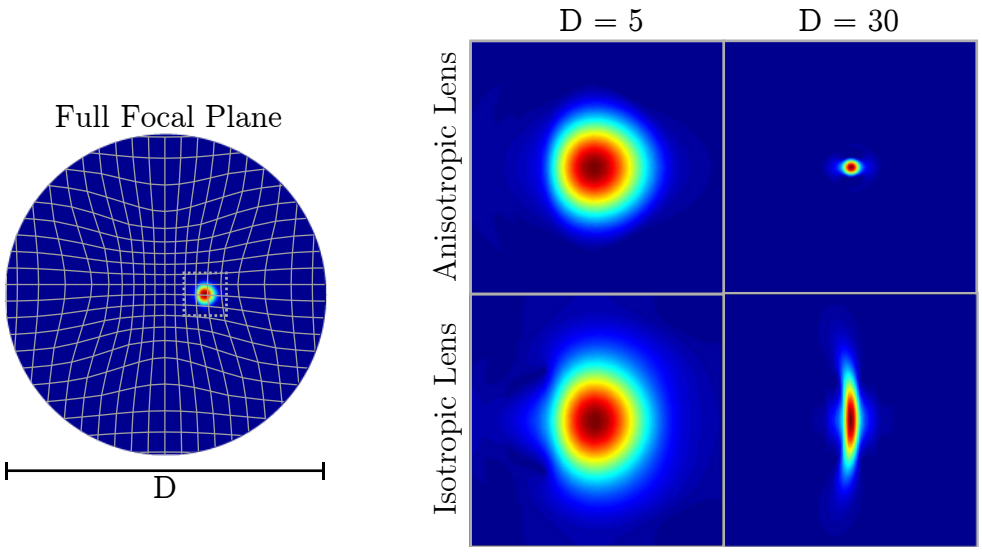

FIGURE 2.11: Intensity plotted in the focal plane of each lens.(Left) Intensity over the full focal plane for a five wavelength, reduced parameter-set lens. A virtual domain grid is overlaid to show distortion in the focal plane. The dotted grey square indicates the relative dimensions of the spot diagrams on the right. (Right, top) Spot diagrams for the reduced-parameter lens for apertures of five and thirty wavelengths. (Right, bottom) spot diagrams for the isotropic, dielectric-only lens at the five and thirty wavelengths.

spread energy over the focal plane so that the diameter of 84% encircled energy is larger than we would expect from qualitative examination of the spot diagrams Fig. 2.11.

While the short-wavelength behavior of the reduced-parameter lens is diffraction limited, the spot diagram shown in Fig. 2.11 clearly differs from the expected Airy disk. The full-parameter lens shows the same behavior at all frequencies: the distortion in the spot is due to the mapping itself. This is unsurprising in light of the Neumann boundary conditions we enforced when generating the map. In the focal plane, the lines of constant ρ, (virtual coordinates), are distorted to guarantee orthogonality in the mapping. To illustrate this distortion, we plot the virtual coordinates in the physical focal plane in Fig. 2.11. We see that an image near the center is de-magnified, whereas an image towards the edge is slightly magnified. Addition-

ally, an image of our 30° incident plane wave is compressed vertically, as we saw in our full wave simulation previously. The only way to circumvent this problem is to specify the virtual domain points directly as done in [53].

2.8 Conclusions

I conclude this chapter by briefly reviewing my contributions and discussing possible avenues for future research and design. Specifically:

- I extended practical TO design to 3D by applying the quasiconformal mapping method to azimuthally-symmetric systems. Using the eikonal approximation, I simplified 3D-TO design by reducing the nonvanishing material responses from six to three. Only one of these remaining responses is magnetic, which further reduces the complexity of design.

- I built on the designs presented by Schurig [53] and Kundtz [59] by flattening the focal surface of a Luneburg lens using the aforementioned QC method in 3D. Using both ray-tracing and full-wave numerical analysis techniques, I have shown that the reduced-parameter lens provides diffraction limited-performance out to 30° for apertures over twenty-five wavelengths in diameter. Future work on this design would consist of experimental verification and generalization to higher frequencies. The specific steps would include:

  - To design a metamaterial unit cell to provide the range of magnetic and dielectric responses required by the reduced-parameter lens design.
  - Verification of unit cell performance by incorporating the retrieved polarizability in a discrete-dipole simulation (Chapter 4) of the full 3D lens.
  - Fabrication and characterization of the reduced-parameter lens at microwave or higher frequencies.

– Generalization of the design to higher frequencies. At infrared frequencies and above, metallic losses may preclude the used of artificial magnetism [68, 69], and alternative methods may be needed to generate the necessary anisotropy in the lens.

3

A Unidirectional Metamaterial Cloak

In this chapter, I examine some of the freedoms in TO design when both the propagation direction and polarization of the problem is fixed. In this work, published in [2], I contribute the following:

- By restricting the polarization of the incident wave, I am able create a new type of metamaterial unit cell for broadband paramagnetism.
- I design, fabricate, and experimentally characterize an impedance-match metamaterial cloak at 10.2 GHz. By restricting myself to a unidirectional design, I am able to reduce residual scattering from the cloak as well as increase the size of the inscribed scatterer as compared to [9].

3.1 Cloaking and Transformation Optics

The very first promise of transformation optics was that it could be used to create a cloak of invisibility. Naturally, this promise captivated both the scientific community and the popular imagination. Since the initial demonstration of the electromagnetic cloak [9], there has been a flurry of activity around the subject. However, the com-

plexity of the TO material prescription has continually forced researchers to make simplifying approximations in order to achieve even a subset of the desired functionality [70, 71, 40, 72, 11, 8, 7], even when the dimensionality of the problem is reduced and the polarization is restricted. These approximations place profound limitations on the performance of TO devices in general [57], and cloaks especially [73, 44].

Most demonstrations of TO-enabled devices have relied on the so-called eikonal approximation; the permittivity and permeability tensors may be adjusted arbitrarily so long as the anisotropic index of refraction is maintained. This approximation is typically used to allow the designer to eliminate a material response in a single direction, thereby greatly simplifying the eventual metamaterial unit cell design. However, this approximation comes at a high cost: the wave-impedance is not inherently matched as it would be for a full-parameter design, and reflections may be created at the interface of the device with free space. Additionally, the eikonal approximation is a short wavelength approximation, and the notion of a locally-varying index of refraction loses all meaning for devices that are themselves inhomogeneous on the order of a wavelength[1]. The goal of this chapter, based on [2], is to show that the complexity of full-parameter design may be overcome by the judicious choice of transformation and metamaterial design. Specifically, we design and experimentally characterize an impedance-matched, unidirectional cloak that realizes the full TO material prescription. We begin by discussing the implemented cloaking transformation.

3.2 Unidirectional Cloaking and the Bi-linear Transformation

This particular cloaking configuration, variants of which were first introduced in [74, 75], may be viewed as a type of ground-plane or carpet cloak [40]. The carpet

[1] Please see Section 2.4 for an in-depth discussion of the eikonal approximation and its use in Transformation Optics design.

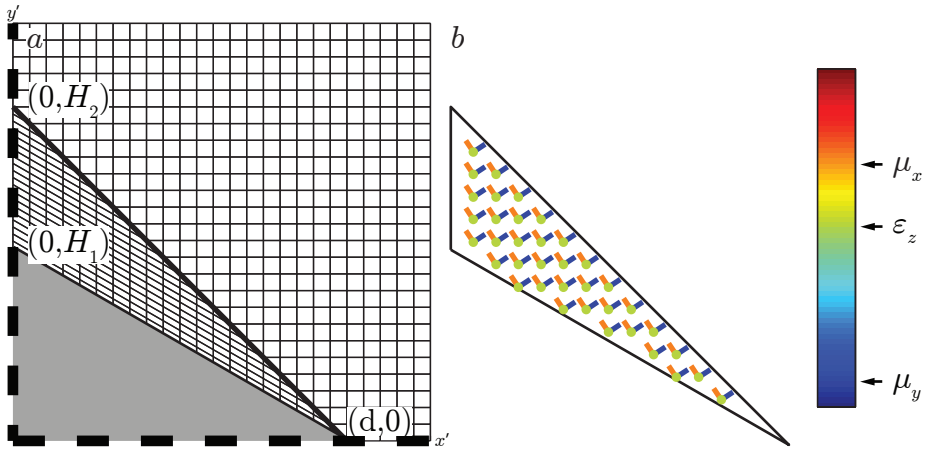

FIGURE 3.1: Graphical depiction of the bilinear transformation and derived material parameters. (a) The transformation is bounded by a triangle of height H_2 and length $2d$, creates a cloaking region of height H_1. Lines of constant x and y, (virtual domain coordinates), are plotted in the physical domain, (x' and y'). In the full design, the transformation is mirrored over both the x- and y- axes. (b) Pseudo-color plot of the material responses required by the cloaking transformation. The full structure is mirrored in the vertical direction. The colored lines, (dots for the out-of-plane component), indicate the direction of the response, and the color indicates the magnitude as shown by the color bar on the far right.

cloak is designed by applying a bi-linear transformation to reduce a two-dimensional (2D) region of space to a line segment. This transformation effectively cloaks any object placed within the 2D region to observers viewing the cloak along the axis of the transformation. The mathematical cloaking mechanism is the same as that of the cylindrical design in that the dimensionality of a region of space is reduced. The difference is that the reduction in the cylindrical cloak is 2D to 0D, (area to point), while in the unidirectional cloak it is 2D to 1D, (area to line). The general transformation, (in the x-y plane), is of the form:

$$\begin{aligned} x' &= x \\ y' &= \frac{H_2 - H_1}{H_2} y + \frac{d - x sgn(x)}{d} H_1 \\ z' &= z \end{aligned} \tag{3.1}$$

where the geometrical parameters H1, H2, and d are defined in Fig. 3.1a. The transformation is plotted in Fig. 3.1a. Using the standard TO algorithm encapsulated by equation Eq. 1.2, we find that the material parameters have the form:

$$\frac{\mathbf{A}\mathbf{A}^T}{|\mathbf{A}|} = \begin{bmatrix} \frac{H_2}{H_2-H_1} & -\frac{H_1H_2}{(H_2-H_1)d}sgn(x) & 0 \\ -\frac{H_1H_2}{(H_2-H_1)d}sgn(x) & \frac{H_2-H_1}{H_2} + \frac{H_2}{H_2-H_1}\left(\frac{H_1}{d}\right)^2 & 0 \\ 0 & 0 & \frac{H_2}{H_2-H_1} \end{bmatrix}. \tag{3.2}$$

In our design, we required that the cloak circumscribe a cylinder of radius R, and have a maximal extent of twice the cylinder radius, i.e. $H_1 = 2R/\sqrt{3}$ and $H_2 = 2R$.

Using standard techniques, we diagonalize Eq. 3.2 using the given geometrical parameters to obtain the material parameters. The direction of the response is given by the eigenvectors of Eq. 3.2. The magnitude and direction of the three responses are indicated on the Fig. 3.1. The benefits of the carpet cloak transformation are two-fold. First, the bilinear transformation yields spatially-homogeneous constitutive parameters, with no zeros or singularities. Additionally, the homogeneity of the medium vastly reduces the complexity of the metamaterial design, since only one metamaterial element is needed, rather than the more challenging gradient structures common to many TO designs. In comparison to the omni-directional cloak designs [6, 9], the absence of extreme constitutive parameters implies that the cloak can operate at frequencies further removed from material resonances; materials that are less dispersive typically exhibit a larger bandwidth of operation with reduced material losses. The price of the carpet transformation is that an object can be effectively cloaked only for a narrow range of observation angles about the axis of the transformation. Permutations of the carpet cloak transformation have been applied to design electromagnetic cloaks operating at visible wavelengths [8, 7] and acoustic structures that cloak sound waves [76]. However, these implementations have relied on the aforementioned eikonal approximation, and are thus mismatched to the surrounding environment. Additionally, these devices could not operate in free

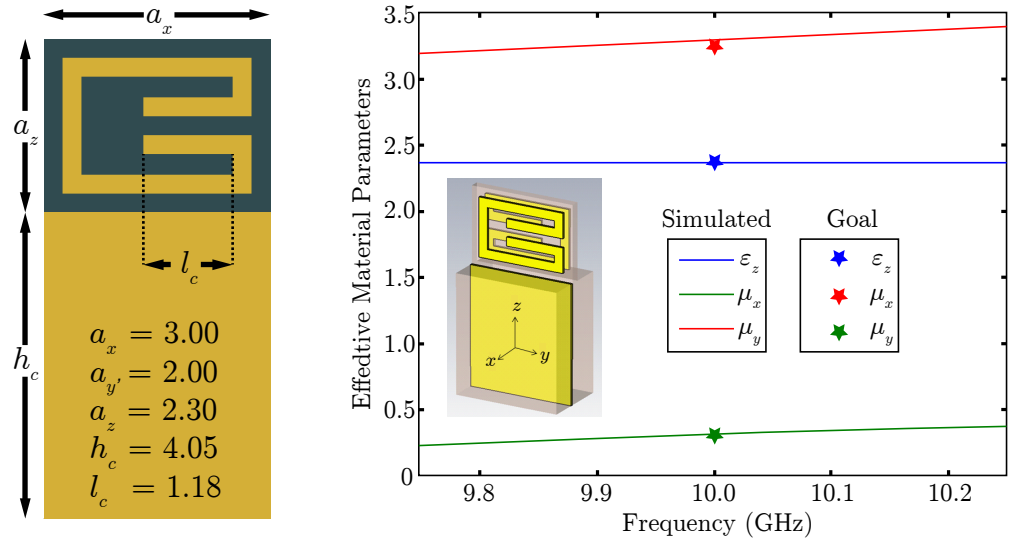

(a) Combined Unit Cell (b) Retrieved material parameters

FIGURE 3.2: (a) Diagram of the unit cell. Dimensions are given in millimeters. The 10-mil substrate is Rogers RT/Duroid 5880 ($\varepsilon_r = 2.2 - 0.002j$) (b) Retrieved material parameters for the unit cell in (a). The inset shows the coordinate system, and The PCB substrate is transparent to show the copper patterning on both sides.

space; they had to be immersed in a dielectric since the material could not provide a refractive index less than one.

3.3 Cloak Design

3.3.1 Metamaterial Unit Cell Design

We implemented the requisite three distinct material responses with two separate metamaterial inclusions. We coupled to μ_y and ε_z with a canonical doubled-sided split-ring resonator (SRR) [24, 29] shown in Fig. 3.2. The magnetic and dielectric responses were tuned by changing the length of the capacitive arm lc and the unit cell height a_z, respectively. A similar design was used to couple to the diamagnetic and dielectric responses required for the eikonal-limit omnidirectional cloak[9]. It would have been possible to use another SRR in each unit cell to provide the paramagnetic response μ_x, but this would have caused several complications that would have ham-

pered cloaking performance. The primary concern was loss: SRRs only provide an appreciable paramagnetic response very close to resonance where the loss tangent is significantly greater [77, 78]. Additionally, the second SRR would significantly increase the effective dielectric in the medium. In order to keep this quantity at the designed value, we would be forced to decrease the fill factor of each SRR, which would increase losses even further [77, 78].

Instead, we exploited the parallel-plate waveguide environment of our testing apparatus alluded to above; that is, we obtain a new degree of freedom by manipulating the waveguide itself to derive an effective response. Specifically, we added one-dimensional corrugations to the bottom plate of the waveguide. The corrugations provide an effective magnetic loading in the direction along the corrugations. Metallic corrugations are common in both guided-wave and radiating devices. These corrugations are typically 1/4- wavelength in depth to provide a resonant response. Theoretically, these corrugations are often treated as lumped, high-impedance surfaces. Once the surface impedance is known, the effects on the modal fields may be determined. However, we demonstrate that corrugations may be fashioned to provide an effective broadband material response. To motivate this reasoning, we introduce a simple field-averaging model [33] for the long-wavelength response of a corrugation in a parallel-plate transmission line, as shown in Fig. 3.3.

Consider the circuit model shown in Fig. 3.3. An ideal (surface) current source K is connected in series with a rectangular metallic cylinder of height h_{TL} and length a. This represents a segment of our transmission line. We insert a corrugation of length t and depth h_c as shown. The average magnetic field [33] is determined by the current source through Amperes law:

$$\mathbf{H}_{av} = \frac{1}{z} \oint \mathbf{H} \cdot d\mathbf{l} = \mathbf{K}. \tag{3.3}$$

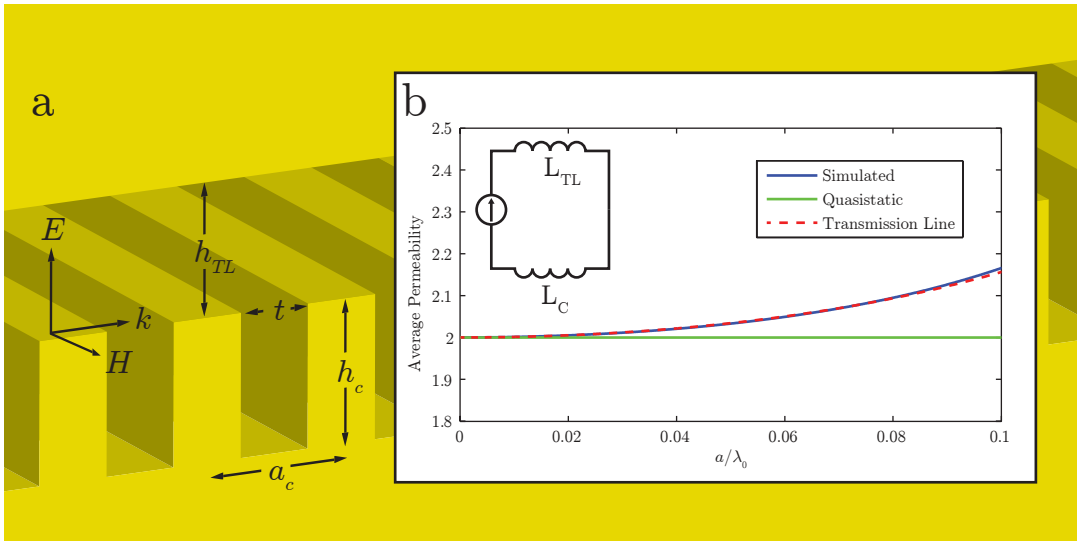

FIGURE 3.3: Depiction of a corrugated transmission line and the derived material response. (a) A corrugated transmission line. The polarization and direction are as indicated. (b) Comparison of permeability retrieved from simulation with the permeability given by analytical models. In units of maximum wavelength, the simulated geometrical parameters are: $a_c = 0.1$, $h_{TL} = 0.05$, $t = 0.05$, and $h_C = 0.1$. The artifacts due to the nonzero lattice parameter a have been removed according to [21, 32]. (b,inset) The circuit model used in the analysis below.

From Faradays law, we determine the total magnetic flux through the circuit:

$$j\omega\Phi = j\omega K\left(L_{TL} + L_C\right), \tag{3.4}$$

where L_{TL} and L_C are the sheet inductances of the unloaded circuit and corrugation, respectively. The flux is then related to the average magnetic induction [33] by:

$$\int \mathbf{B}\cdot d\mathbf{s} = B_{av} h_{TL} t. \tag{3.5}$$

The average permeability is defined as the ratio of B_{av} to H_{av}. Therefore,

$$\mu_{av} = 1 + \frac{h_c t}{h_{TL} a} \tag{3.6}$$

where we have made the approximations $L_{TL} \approx \mu_0 h_T L a$ and $L_C \approx \mu_0 h_C t$. These

approximations are valid in the limits $t \ll a$ and $t \ll h_C$ so that the fields are quasi-uniform in the structure. According to Eq. 3.6, and in contrast with the response of an SRR, the corrugations provide an appreciable magnetic response far from the material resonance. This mitigates both material dispersion and losses around the operational frequency.

In the absence of all other considerations, the effective magnetic loading is maximized by setting $t = a$ and maximizing h_C/h_{TL}. In reality, we are bounded by the need to remain in the quasi-static limit and by the need to fit a split-ring resonator in the transmission line. Additionally, we note that this effect is only appreciable for transmission lines that are narrow with respect to the corrugation height, which may limit its utility in many systems.

The frequency response of simulated corrugation is shown in Fig. 3.3. In contrast to the quasi-static model, there is clearly some dispersion. To account for the dispersive nature of the corrugation, we replace the inductive impedance $j\omega L_C$ in equation 3.4 with a generalized sheet impedance:

$$Z = j\omega\eta_0 t \tan\left(k_0 h_c\right). \tag{3.7}$$

This yields:

$$\mu_{av} = 1 + \frac{t \tan\left(k_0 h_c\right)}{k_0 h_{TL} a}. \tag{3.8}$$

The frequency responses of these models are plotted in Fig. 3.3. The transmission-line model better predicts the dispersive behavior of the corrugation, but it has an explicit dependency on the wavenumber in the corrugation. This spatial dispersion limits the utility of the effective medium description, especially when the angle of the incident wave is allowed to vary. Fortunately, a series expansion shows that Eq. 3.8 is independent of k to first-order, and that the dispersion has the typical Lorentzian form. In our design, Eq. 3.8 was used to generate an initial corrugation.

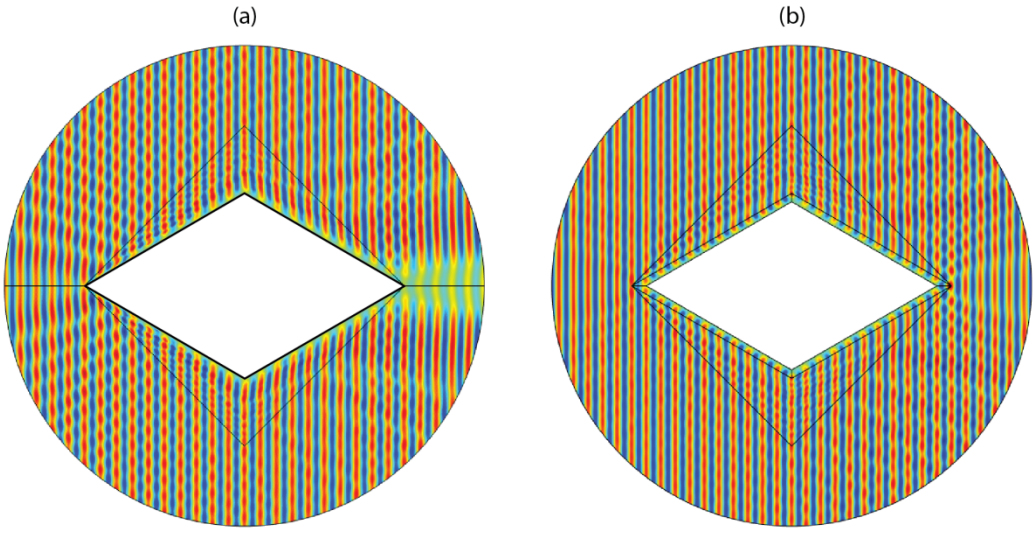

FIGURE 3.4: Effect of PEC and PMC boundary conditions on cloaking performance for TMz polarization. (a) Unidirectional cloak with PEC inner core. (b) The same cloak with a wavelength separation between the inner cloaking boundary and the PEC core.

The complete unit cell was then optimized using commercial electromagnetics code driven by a MATLAB script.

3.3.2 Polarization and Boundary Conditions

One subtlety arises from the boundary conditions that are enforced on the inner surfaces of the cloak. The mathematical considerations behind the transformation ignore the effect of differing boundary conditions for incident waves of different polarizations. Whereas the scattering cross-section of a point is identically zero, a line can scatter if it violates the boundary conditions of the incident wave. Specifically, a perfectly conducting line segment enforces $\hat{\mathbf{n}} \times \mathbf{E} = 0$. If the incident wave has a component of the electric field along the line segment, a scattered wave must appear so that the total field obeys this boundary condition. This is exactly the case in our cloaking configuration, as depicted in Fig. 3.4. Fortunately, there is a straightforward method [79, 80, 81] to transform this boundary condition to that of a perfectly mag-

netic conductor (PMC). The PMC enforces the condition $\hat{\mathbf{n}} \times \mathbf{H} = 0$. This boundary condition is obeyed by our incident field, so a surface of this type will not introduce scattering.

We now derive the thickness of a dielectric slab to form an effective PMC surface. At normal incidence, the wavenumber in the cloak is equal to that of free-space, k_0. This wave is incident on a slab of dielectric ε_r that acts as our impedance-transforming layer (ITL). Snells law requires that

$$k_x^{cloak} = k_x^{dielectric} = k_0 \cos(\theta), \tag{3.9}$$

and the phase through the ITL is then

$$k_y d = \sqrt{\varepsilon_r k_0^2 - k_0^2 \cos^2(\theta)}. \tag{3.10}$$

The PMC boundary condition is achieved when $k_y d = \pi/2$ [79, 80, 81], so that the reflected is in-phase at the inner cloaking interface. Therefore,

$$d = \frac{\lambda_0}{4\sqrt{\varepsilon_r - \cos^2(\theta)}}. \tag{3.11}$$

For fabrication and design simplicity, we used $\varepsilon_r = 1$. Combined with $\theta = 30°$, this yields $d = {}_0 2$. Fig. 3.4 (b) shows significant scattering reduction with the additional ITL. There is some residual scattering localized at the cloaking vertices where the half-wavelength condition cannot be fulfilled.

However, this model does not account for differences in height between the 2D transmission line in the cloaking layer and ITL. The height difference introduces a shunt susceptance that increases the phase in the ITL, which in turn decreases the optimum thickness d. Numerical simulations revealed that the new optimum thickness for this configuration is $d \approx \lambda_0 4$, as depicted in the simulation from Fig. 3.5b.

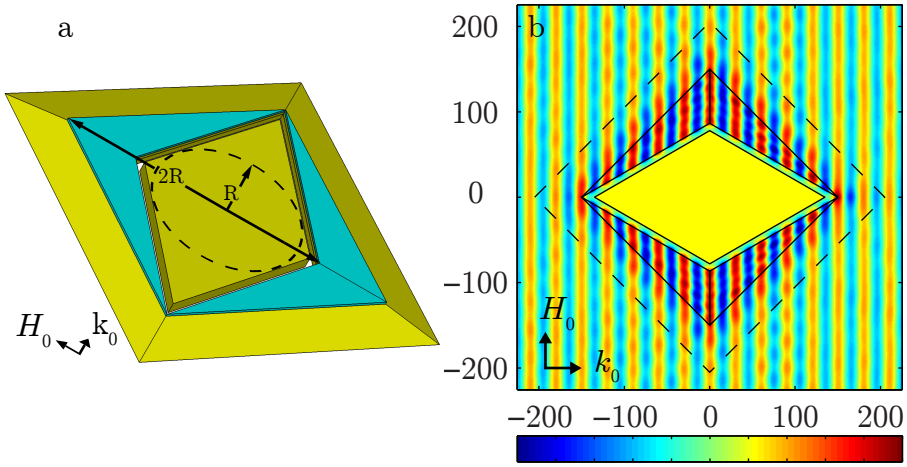

FIGURE 3.5: (a) 3D representation of the fabricated cloak. The cloak was designed to circumscribe a cylinder of radius $R = 7.5$ cm. (b) 3D Finite-Element Simulation of an electromagnetic wave incident from the left on the cloak. The dashed line indicates the extent of the taper beyond the edge of the metamaterial region.

3.3.3 Combined Cloak Design

The use of corrugations restricts the cloak to 2D operation. However, the cloak could be used outside of the 2D mapping environment by taking our design as shown in Fig. 3.5a and stacking it periodically in the out-of-plane direction. Additionally, our unit cell design and optimization assumed a parallel-plate wave-guiding environment with a height equal to the lattice parameter a_z of our unit cell. To accommodate the physical environment of our measurement apparatus, we designed a waveguide taper to squeeze the electromagnetic waves into this configuration. Full-wave simulations showed that a taper angle of 12.5° was sufficient to minimize reflections while keeping the footprint of the taper relatively small, as shown in Fig. 3.5(b).

Another subtlety of our design is that the bounding volume, (or unit cell), of our periodically positioned MM element is not rectangular. We modified the MM unit cell because a rectangular unit cell would introduce voids at the intersection of each quadrant of the cloak. Numerical simulations revealed performance was especially

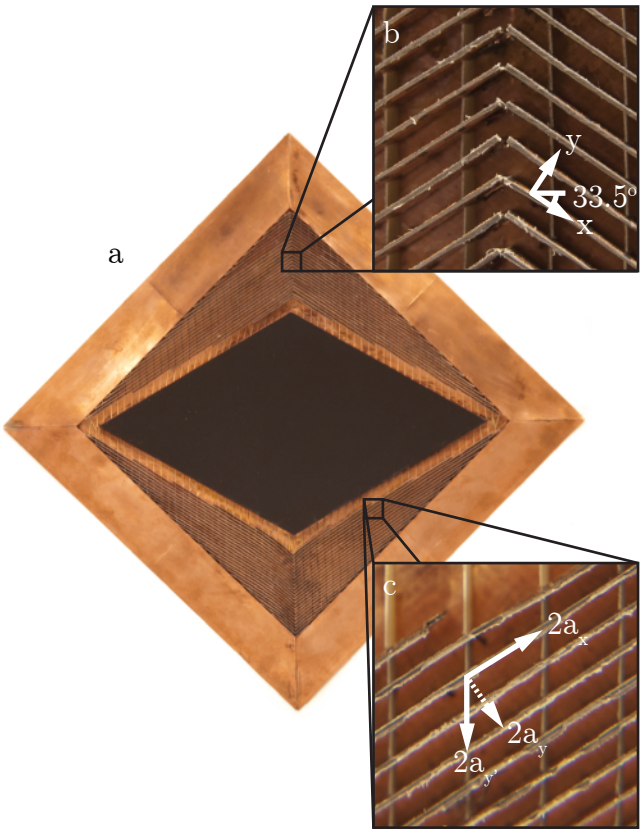

FIGURE 3.6: Photographs of the fabricated cloak. (a) A photograph of the full cloak. (b) A photograph of an internal material interface. The labeled arrows depict the orientation of the local coordinate system. The corrugations run along x, providing an effective response in that direction. Each strip has been shifted along x so that there is no discontinuity at the interior boundaries of the cloak. (c) A photograph of the material with overlaid arrows depicting the in-plane lattice vectors for the metamaterial unit cell. The vectors are twice the length of the lattice vectors to aid visibility.

sensitive to defects in this region: even small gaps would result in large reflections. To ensure the correct material interface, the strips of SRRs have been shifted so that each strip meets its mirror image at the interior boundaries of the cloak. This shift is shown graphically in Fig. 3.6b.

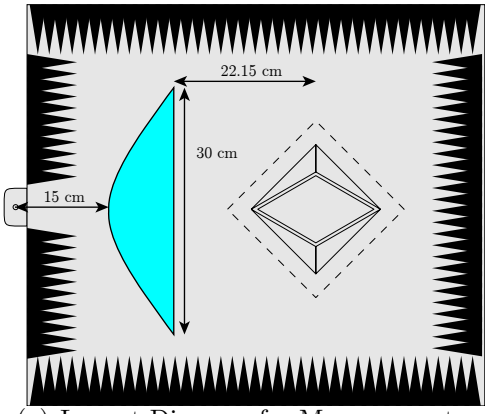

(a) Layout Diagram for Measurement.

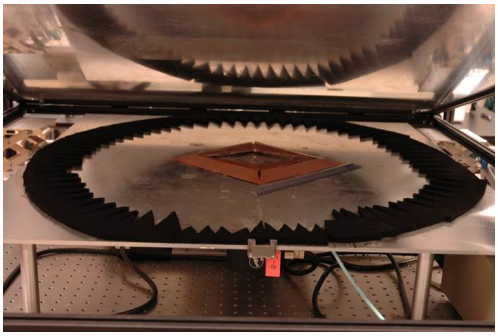

(b) Photograph of the Fabricated Cloak in the Chamber.

FIGURE 3.7: (a) Layout for the cloaking measurement. A hyperbolic lens creates a collimated incident beam. Commercial absorber is used to mitigate reflections from the edges of the waveguide plates. (b) Photograph of the fabricated cloak in the open 2D mapping chamber chamber. A one-foot ruler is shown for scale.

FIGURE 3.8: Diagram of a prototypical MM strip (top layer). The dotted lines indicate the contour for the cut-out.

3.4 Fabrication

The metamaterial portion of the cloak was fabricated using standard printed circuit board (PCB) photolithography[2]. The PCB design consisted of double-sided 10 mil Rogers RT/Duroid coated with 1 oz copper plating. The first layer consisted of 1D array of SRRs over strips of copper formed the waveguide corrugations when assembled. The bottom layer was composed of mirrored-SRRs directly underneath

[2] The circuit boards were fabricated by Prototron Circuits, 3760 E 43rd Pl Tucson, AZ 85713.

their first layer counterparts. As indicated in Fig. 3.1, the principle axes of the unit cell were neither perpendicular nor parallel to the external edges of the cloak. Therefore, no single unit cell lattice spacing would permit us to create strips of the correct length such that they contained an integer number of SRRs. We therefore calculated the integer number of cells that was closest to the correct length and extended or cut the SRR layer as needed. Since the corrugations were invariant in the direction of the strip, we simply truncated the corrugation's metallization at the correct length.

We cut the individual strips using a numerically-controlled milling machine (ProtoMat 100, from LPKF, Oregon) using a 10 mil endmill. We also cut out periodic notches as shown in the dotted line in Fig. 3.8. These notches intersect corresponding notches in FR4 (epoxy resin reinforced with glass fibers) support strips oriented vertically with respect to the page in Fig.3.6(a)-(b). These support strips provided mechanical stability to the MM strips. The support strips were of height h_c and were therefore contained entirely in the corrugations. Since the fields in the corrugations were primarily magnetic, the strips were not expected to perturb the effective medium parameters of the unit cell. This was verified in subsequent CST simulations.

As previously mentioned, the waveguide taper was designed to channel an incident wave into the corrugated waveguide environment of the cloak. The taper was also designed to provide structural support from the cloak from below, as shown in Fig. 3.9. The combined cloak and taper was height was 10.75 mm, leaving 250 μm clearance for motion between the top and bottom plates of our scanning apparatus. The other dimensions are as shown in Fig. 3.9. The support structure was composed of planar sections of FR-4. The support sections were cut out in the same manner as the MM strips, except a 1 mm contour router was used in place of the 10 mil endmill. The cut-out support sections were assembled by hand and joined using standard household two-part epoxy. The glued support assembly was held together

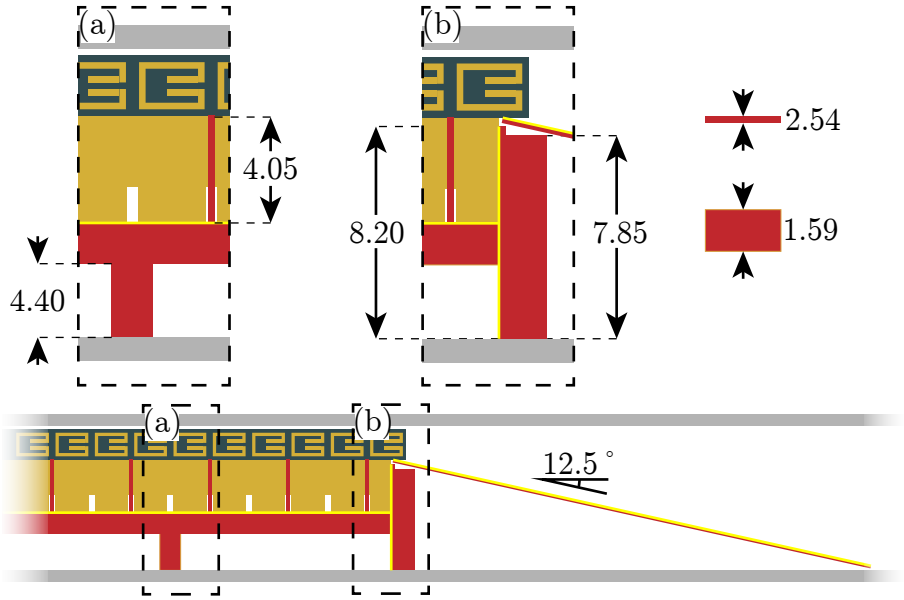

FIGURE 3.9: Diagram showing relevant dimensions for the cloak support structure and waveguide taper inside the parallel-plate waveguide. All dimensions are given in millimeters. 1/2 oz copper plating is indicated by bright yellow lines.

and allowed to dry in a frame consisting of optical component clamps on an optical table.

The MM strips and FR-4 cross strips were assembled separately from the support frame. Once assembled, the strips were deposited *en masse* into the support structure. Prior to this step, two-part epoxy had been deposited uniformly on the interior of the frame. A flat aluminum plate was placed over the MM strips while the epoxy dried to insure uniformity in the cloak height and minimize the separation between the MM strips and the ground-plane in the interior of the support assembly.

The final step was the construction of the waveguide taper. The waveguide taper was fashioned from sheets of 10 mil double-sided copper clad FR-4. The various strips of the taper were first combined with copper tape and then the composite structure was glued to the assembly using epoxy.

3.5 characterization and Experimental Results

3.5.1 Characterization

We characterized the cloaking performance in a 2D planar waveguide apparatus previously reported [82]. The various dimensions of the apparatus, as well as the specific part numbers and manufacturers may also be found in [82]. The setup consisted of parallel aluminum plates that approximated PEC boundaries boundaries. The waveguide height of 11 mm ensured that only TM^z modes could propagate. The source of electromagnetic waves was a Vector Network Analyzer (VNA) that was connected to the parallel plate waveguide via an SMA cable. A coax-to-waveguide adapter provided a transition from the SMA to the parallel plate waveguide.

The experimental layout is shown in Fig. 3.7(a). In [9], a quasi-plane wave was created by placing the cloak in the far-field of the coax-to-waveguide launch. Our cloak is significantly larger than Schurig's design, and we were forced to add additional complexity to our apparatus to approximate a plane-wave while remaining in the field of view of the probe antennas. As shown in Fig. 3.7(a), we fashioned a hyperbolic lens from 1-cm thick polycarbonate ($\varepsilon_r = 2.45$) to collimate the source from the launch.

A hyperbolic lens collimates a point-source located at the origin of a polar coordinate system when the first surface of the lens is given by [83]:

$$\begin{aligned} \rho(s) &= \frac{(n-1)\,f}{n\cos s - 1} \\ \phi(s) &= s. \end{aligned} \tag{3.12}$$

The second surface of the lens provides no focusing power, so the thickness only determines the f-number of the lens. As shown in Fig. 3.7(a), we chose a focal length $f = 15$ cm and lens diameter $d = 30$ cm.

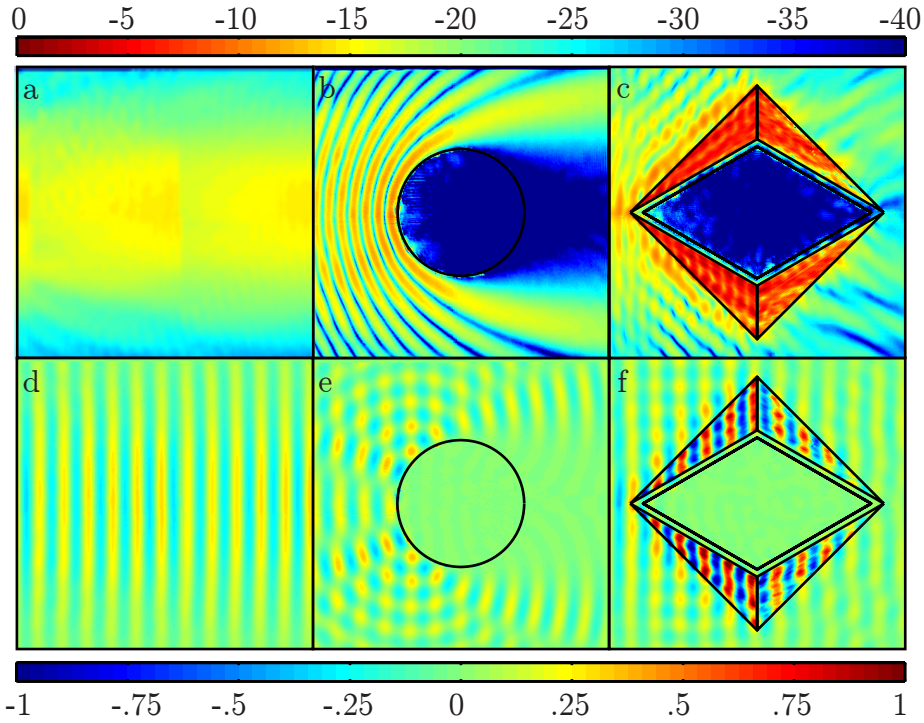

FIGURE 3.10: Measured electric field data for free space, the cloak, and a copper cylinder at the optimum cloaking frequency of 10.2 GHz. (a),(b), and (c) depict the absolute value of the field in decibels for free space, the cloak, and the cylinder, respectively. (d), (e), and (f) depict an instantaneous snapshot of the measured fields. The scaling on the top row is in dB, normalized to the maximum measured field. The scaling on the bottom row is linear and normalized to the maximum and minimum values of the instantaneous field. The scaling is given by the color bars on the top and bottom of the figure for the field amplitude, and instantaneous field, respectively.

3.5.2 Experimental Results

For comparison, we also measured a bare copper cylinder with radius $R = 7.5$ cm. The measured field data are shown in Fig. 3.10. As expected, the electrically-large cylinder strongly scatters the incident wave, resulting in a deep shadow in the forward (right) direction and a large standing wave to the left. Both of these scattering features are almost completely absent in the field plots of the cloak. The MM device guides the microwave radiation around its copper core so that the incident wave is

restored in both amplitude (Fig. 3.10c) and phase (Fig. 3.10f) upon exiting the cloak on the right. The difference in performance is particularly striking in the shadow region: the field is almost 20 dB stronger to the right of the cloak than to the right of the cylinder.

Unfortunately, the experimental layout precludes highly accurate calculation of a scattering cross-section (SCS) as performed in [84]. Multiple scattering events between the lens and the cloak make the scattering cross-section a nonlinear function of the scattered fields from the lens and cloak composite structure. However, we have performed calculations for the scattering cross-section of both the cylinder and cloak at 10.2 GHz using the methods given in [84]. The SCS of the cloak was 180.5 mm, whereas the SCS of the copper cylinder was 356.6 mm. The expected SCS of the cylinder from Mie theory was 329.1 mm, but we can not necessarily expect the same 8% error the cloak because this error depends on the interactions of the scatterer and the lens. Nevertheless, we see that the measured SCS is approximately half that of the cylinder, and we can therefore reasonably claim a cloaking effect in our device.

3.5.3 Error Analysis

In the previous subsection, we alluded to the presence of error in our characterization techniques that contributed to discrepancies between measurement and theory, as well as degradations in the measured performance. We first discuss errors in the characterization and measurement.

- We believe that the primary source of error in our measurement was due to interactions between the cloak or metal cylinder and the collimating lens. For instance, the reflected fields from the metallic cylinder were re-scattered by the lens where they can interact again with the cylinder. Therefore, the illumination source for the cylinder was no longer a plane wave and the scattered field no longer had direct correspondence with the true SCS of cylinder. Addition-

ally, the scattered fields from the lens would perturb the measurement of the SCS, which involved the integration of the fields over a circle circumscribing the scatterer [3]. If our cloak was perfect and perfectly aligned, we would still expect to measure zero SCS. However, imperfect fabrication and design contributes to a nonzero SCS, and the measured SCS may have differed from the true value.

- Alignment error may have also been substantial. The mapping chamber was not constructed to allow for a clear view of apparatus inside the chamber, and our view was partially obscure as we attempted to align the lens and cloak by hand. Rotational misalignment of the cloak would increase the measured SCS since the cloak was only intended to operate for 0° incidence. However, this would be a relatively small effect since the cloaked geometrical cross-section of the transformed object would still be small. A small tilt of the lens would produce a similar error since the tilted lens would produce a beam oriented at an angle to the cloak. Tilt would also introduce aberratopms since the hyperbolic lens is only a perfect optic for a point source on the optical axis.

Small imperfections in design and fabrication inevitably degrade cloaking performance. This degradation manifests as reflections from the cloaking boundary and improper reconstruction of the phase fronts of the incident wave. Additionally, we note that the cloaking frequency has shifted from 10 to 10.2 GHz upon implementation. We now discuss possible reasons for these discrepancies between measurement and theory.

- Due to our finite computational resources, we never simulated the cloak with all of the microstructure of the unit cells. Instead, we simulated a 2D array of orthorhombic unit cells such that only one cell was in the direction of incident wave propagation. This could have introduced several errors:

- Our simulations neglected the shift of adjacent strips relative to one another. This would change inter-unit cell coupling between MM elements, i.e. it would modify the mutual inductance and capacitances between individual resonant elements. Simulations show that μ_x is particularly sensitive to this coupling: small deviations in the resonant frequency of the SRR would result in a large deviation of the permeability. Since the deviation would not be the same in all the constitutive parameters, the cloaking efficacy would degraded at the shifted frequency.
- Coupling between unit cells in the third dimension was neglected by our simulations. This could have caused a similar error in the effective material parameters as described previously.
- Our simulations could not show the effect of the irregular termination of the array at the cloaking boundaries. In the presence of mutual coupling between unit cells, the electromagnetic environment of the boundary cells would differ significantly from those in the interior of the cloak, and the effective properties of these layers can differ significantly. Additionally, since the termination is irregular across the boundary, the materials can not be estimated as they could be for Drude transition layers in a regular slab [85].

- The PCB substrate (Rogers RT/Duroid 5880) was not rigid, and the device performance was very sensitive to repeated handling. The waveguide taper was similarly sensitive since the FR-4 substrate was thin and the deformed copper coating retained its shape when deformed. During each measurement, the taper was affixed to the bottom plate of the parallel plate with copper tape. When the copper tape was removed, some deformation of the tape occurred. This problem was exacerbated by repeated measurements: subsequent mea-

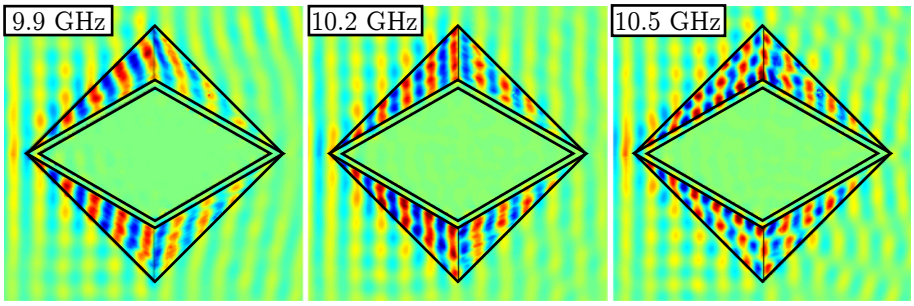

FIGURE 3.11: Measured field data at several frequencies showing the effects of material dispersion. From left to right, the fields are depicted at 9.9, 10.2 and 10.5 GHz.

surements showed qualitative cloaking results similar to those of Fig. 3.10, but the SCS no longer showed cloaking, and the SCS was not consistent between repeated measurements.

- We noted in Subsection 3.3.3 that cloaking performance was sensitive to defects in the interior cloaking boundaries. As discussed, we attempted to minimize defects by shifting the MM strips. However, the strips were not connected at these interior boundaries, and warping is visible in Fig. 3.6(b). We see the effect of this warping in Fig. 3.10(c). Reflections at the internal boundaries manifest as a modulation to the amplitude of the fields in the left hand portions of the cloak. This increased the SCS with respect to the simulated value.

3.6 Material Dispersion and Bandwidth

All free-space cloaks require supra-luminal phase velocity and are therefore necessarily dispersive in frequency. To see the effect of this dispersion on the fabricated design, we plot the measured instantaneous field values around the optimal cloaking frequency of 10.2 GHz in Fig. 3.11. There is clear distortion in the transmitted phase in the plots at 9.9 and 10.5 GHz. Referring to Fig. 3.11, we see that both components of the permeability are fairly dispersive in the measured frequency range. At

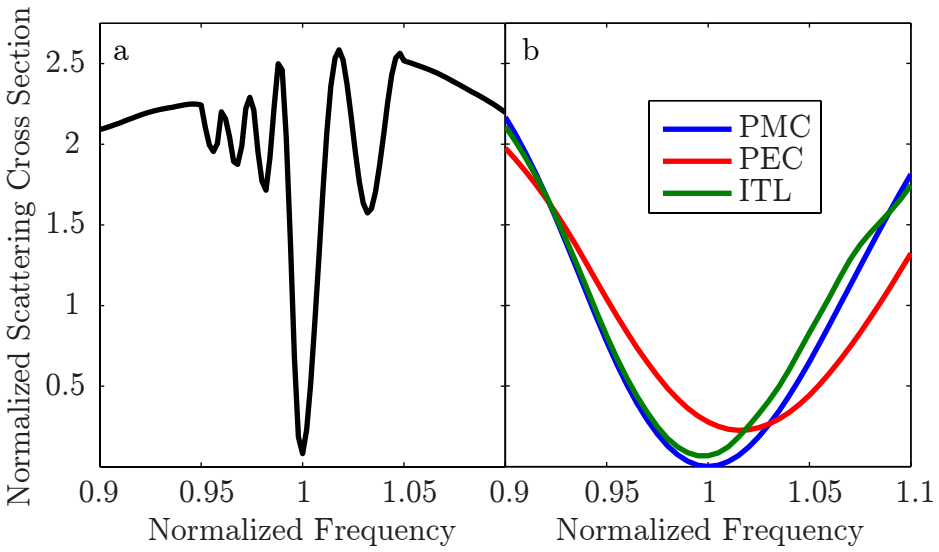

FIGURE 3.12: (a) Simulated scattering cross-section of a cloak with the fabricated material parameters over a 20% frequency band. (b) Simulated performance comparison of a cloak with minimal dispersion in the presence of different boundary conditions. The SCS of each cloak is normalized to the SCS of the inscribed PEC cylinder.

9.9 GHz, the anisotropic index is slightly lower than required by the cloaking transformation, and the wave acquires less phase as it travels through the cloak than it would in free-space. At 10.5 GHz, the index is too high and the wave acquires too much phase in the cloak. However, we note that reflections are fairly minimal at all three frequencies, which indicates that the material parameters do not vary enough to significantly alter the wave impedance of the structure. Instead, the scattering is dominated by the sheer size of the cloak; and the long path length ensures that even small deviations in the material parameters will severely hamper performance. We can see this effect quantitatively by simulating the cloak with the retrieved material values from Fig. 3.2 and calculating the total scattering cross-section, as shown in Fig. 3.12. The phase error in the transmitted wave significantly alters the far-field scattering characteristics of the cloak, and limits it to an effective bandwidth of approximately 1%. However, we did not attempt to optimize the performance

bandwidth for this design. It is therefore natural to ask what the bandwidth could be, subject to limitations of material response. To determine this bandwidth, we assume that we can configure our unit cell so that the only response with appreciable dispersion comes from the SRR due to its resonant nature. The SRR response is given by [24]:

$$\mu_y = 1 + \frac{F\Omega^2}{1-\Omega^2}, \tag{3.13}$$

where Ω is the frequency normalized to the resonant frequency of the SRR and F is the geometrical filling factor of the split ring. It is straightforward to show that the dispersion is minimized by maximizing F. However, for the response to be causal for a specified effective permittivity, we require that:

$$F \leqslant 1 - \epsilon_z^{-1}. \tag{3.14}$$

To determine the maximum cloaking bandwidth for a cloak with of our dimensions, we simulate a cloak with the dispersion determined by Eq. 3.13 subject to Eq. 3.14. Additionally, we note that the ITL is dispersive and will affect bandwidth of our design. We therefore simulate the cloak with the physical ITL as well as dispersion-less PEC and PMC inner boundaries. The calculated scattering cross-sections resulting from these simulations are shown in Fig. 3.12. As expected, the dispersive cloak with the perfect PMC inner boundaries shows the lowest SCS (nominally zero subject to numerical noise), as well as a bandwidth of about 12%. The cloak with the ITL shows slightly decreased performance in both its minimum and SCS, and in bandwidth. The ITL-loaded cloak has a higher SCS, 7%, since the design cannot satisfy the correct separation from the material boundary to the PEC at the four sharp corners of the design. The bandwidth however is only decreased to 11% due to the dispersion of the ITL boundary. The material dispersion clearly dominates the overall bandwidth of the cloak. The PEC cloak shows the highest

SCS minimum, 23%, as expected, but also a slightly enhanced bandwidth, 13%. This slight enhancement may be due to interaction with the scattered field from the imperfect cloak, as well as the fields from the effective PEC sheet. However, the effect is minor and a rigorous investigation of this phenomenon is outside the scope of this work.

3.7 Conclusions

In this chapter, I have performed the following:

- I have created a metamaterial unit cell with two distinct magnetic responses that I implemented in a full-parameter unidirectional cloak.
  - Measured data revealed that the optimal cloaking frequency had shifted from the designed frequency of 10 GHz to 10.2 GHz. I attributed this shift to intra-unit cell coupling that was not considered in the design of the unit cell. In Chapter 4 I show that phase error can occur when spatial dispersion is neglected. Future work might incorporate corrections to compensate for this error in a manner similar to the one that I demonstrate in Section 4.4.
  - Future work on this design could also involve an extension to 3D. As previously stated, my current design is limited to 2D operation. Additionally, the corrugations prohibit further generalization. Therefore, a 3D implementation would require another method to generate the necessary paramagnetic responses.
- I designed, fabricated, and experimentally characterized the aforementioned cloak, and showed approximately 50% reduced scattering from the cloaked object.

– My cloak required a parallel-plate waveguide to function. However, I asserted that the cloak could be implemented in free space by stacking identical copies of the cloak and taper combination in the the out-of-plane direction, (i.e. the direction of the incident wave polarization.), this cloak could then be measured in a conventional anechoic chamber or compact range.

4

The Discrete Dipole Approximation for Metamaterial Design

This chapter describes the Discrete Dipole Approximation for the analysis and design of TO-derived metamaterial devices. My contributions to this topic are as follows:

- I extend the work of Bowen et. al. [86] to analyze MM structures using the Discrete Dipole Approximation. I apply the Poisson summation technique to accelerate the convergence of Green's function calculations.

- I extend the work of [32, 87, 88] to derive the dispersion relation for Bloch modes in a magneto-dielectric lattice. I use this expression to find microscopic polarizabilities that improve the performance of TO-designed devices with a non-zero lattice spacing.

- I reformulate the DDA in terms of coupled circuits. This allows me to use partial knowledge of metamaterial unit cells to increase the accuracy of the DDA for dense arrays whose interactions are more complex than those of point dipoles.

In essence, the Discrete-Dipole Approximation (DDA) is a numerical modeling tool motivated by physical reality. Purcell and Pennypacker [89] introduced the DDA to solve the scattering problem from irregularly shaped intersteller grains [89]. They noted that the permittivity of a cubic crystalline structure is given by the Clausius-Mossotti equation:

$$\varepsilon = \varepsilon_0 + \frac{3}{d^3}\frac{\alpha}{1-3\alpha}, \tag{4.1}$$

meaning that the permittivity is determined by the average polarization of the ensemble, but the dipolar responses, $(\mathbf{p}_i)$, of individual elements i are influenced by all of the other elements in its vicinity. They noted that a specified ε could be achieved on a relatively coarse grid by re-scaling the polarizabilities α_i to satisfy 4.1.

For a finite scatterer of arbitrary shape, both the polarization $\mathbf{P}$ and fields $\mathbf{E}$ and $\mathbf{H}$ will vary with position $\mathbf{r}$. However, a linear system of equations may be constructed to solve for the individual $\mathbf{p}_i$ in the structure for a known incident field $\mathbf{E}_0$. Once the dipole moments are determined, the scattered fields may be found from the superposition of equivalent-source dipole fields.

It was subsequently shown that the DDA was equivalent to other numerical methods, such as the VFIE and digitized Green's function method. However, the DDA has evolved relatively independently of these other techniques due to its early adoption by the astrophysics community, relative simplicity, and use in open-source codes. Over the past forty years, a number of modifications have been introduced to increase the capabilities of the method. Yurkin presented a comprehensive overview of the development of the DDA in [90].

Despite these advances, the DDA still suffers in comparison to other numerical tools. Performance drops sharply as the electrical size of the scatterer is increased [91, 92]. The DDA has been greatly hindered by its simplistic formulation and the numerical problems associated with the inversion the dense interaction matrices.

Fortunately, we do not want to use the DDA as a method to model continuum scatterers. Instead, we use the DDA to model and understand some of the approximations inherent to TO-MM design. Some initial efforts have already been made in this direction. Bowen et. al. [86] used the DDA to investigate artifacts due to nonzero lattice spacing and crystalline defects on cylindrical cloaks. We proceed along similar lines in our initial development and verification. However, we go on to show that the DDA may serve as a conceptual tool to improve both the accuracy of MM-TO models and the performance of physical devices.

4.1 The Discrete Dipole Approximation in 2D

The fundamental magneto-dielectric DDA equations are given by[93, 94, 86]

$$\left(\bar{\bar{\boldsymbol{\alpha}}}^{ee}\right)_i^{-1}\mathbf{p}_i = \mathbf{E}_0\left(\mathbf{r}_i\right) + \epsilon_0^{-1}\sum_{j\neq i}\bar{\bar{\mathbf{G}}}_{ij}^{ee}\mathbf{p}_i + \sum_{j\neq i}\bar{\bar{\mathbf{G}}}_{ij}^{em}\mathbf{m}_i, \tag{4.2a}$$

$$\left(\bar{\bar{\boldsymbol{\alpha}}}^{mm}\right)_i^{-1}\mathbf{m}_i = \mathbf{H}_0\left(\mathbf{r}_i\right) + \sum_{j\neq i}\bar{\bar{\mathbf{G}}}_{ij}^{me}\mathbf{p}_i + \mu_0^{-1}\sum_{j\neq i}\bar{\bar{\mathbf{G}}}_{ij}^{mm}\mathbf{m}_i, \tag{4.2b}$$

where $\bar{\bar{\mathbf{G}}}$ is the dyadic Green's function of the type indicated by the superscripts e and m. From reciprocity, $\bar{\bar{\mathbf{G}}}^{ee} = \bar{\bar{\mathbf{G}}}^{mm}$ and $\bar{\bar{\mathbf{G}}}^{em} = -\bar{\bar{\mathbf{G}}}^{me}$. This form of the DDA equation is sufficient for our purposes, but a more general formulation that includes local bianisotropy may be found in [93, 95]. In this development, we will restrict ourselves to TM^z fields and consider each element i to represent a z-oriented infinite column of scatterers with a periodicity a_z. In this case, the DDA equations can be written [86], e.g., for Eq. 4.2a:

$$\begin{aligned}\left[\left(\bar{\bar{\boldsymbol{\alpha}}}^{ee}\right)_i^{-1} - \varepsilon_0^{-1}{\sum_{n=-\infty}^{\infty}}'\bar{\bar{\mathbf{G}}}^{ee}\left(na_z\hat{\mathbf{z}}\right)\right]\mathbf{p}_i = \mathbf{E}_0\left(\mathbf{r}_i\right) + \varepsilon_0^{-1}\sum_{j\neq i}\sum_{n=-\infty}^{\infty}\bar{\bar{\mathbf{G}}}\left(\boldsymbol{\rho}_{ij} + na_z\hat{\mathbf{z}}\right)\mathbf{p}_i \\ + \sum_{j\neq i}\sum_{n=-\infty}^{\infty}\bar{\bar{\mathbf{G}}}^{em}\left(\boldsymbol{\rho}_{ij} + na_z\hat{\mathbf{z}}\right)\mathbf{m}_i,\end{aligned} \tag{4.3}$$

and a similar equation exists for Eq. 4.2b. The summation over n on the LHS represents the response of all the identical elements in column i, and the prime ($'$) indicates that we are omitting the dipole at the origin. The summation over n on the RHS corresponds to the sum over identical dipoles in remote column j. We have written Eq. 4.3 in a leading way to show that the self-contribution on the LHS may be inserted into an effective polarizability representing each column. We label this interaction constant $\mu_0 C_{yy}^{(1)}$. Methods exist for calculating this term efficiently, but we have relegated their explicit forms to the Appendix A.

Let us consider the field radiated by a single column of dipoles. The Hertzian potential, (e.g., along z), will be of the form:

$$G = \frac{1}{4\pi} \sum_{n=-\infty}^{\infty} \frac{\exp -jk\left[\sqrt{x^2 + y^2 + (z - na_z)^2}\right]}{\sqrt{x^2 + y^2 + (z - na_z)^2}}. \tag{4.4}$$

In order to calculate the potential or derived fields at any point, we must explicitly sum Eq. 4.4 until we reach suitable convergence. Unfortunately, this convergence will be relatively slow since the fields decay only as R^{-1}. On the other hand, we expect the fields far from the column to be those of a dipolar line current since the spacing a_z is, (presumably), below $\lambda/2$. Therefore, we recast the potential in terms of its discrete spectral components using the Poisson summation technique:

$$\sum_{n=-\infty}^{\infty} f(\alpha n) = \frac{1}{\alpha} \sum_{n=-\infty}^{\infty} F\left(\frac{2n\pi}{\alpha}\right). \tag{4.5}$$

Applying equation 4.5 to equation 4.4, we find:

$$G = \sum_{n=-\infty}^{\infty} \frac{1}{2\pi a_z} K_0(c_n \rho) e^{jz\frac{2\pi n}{a_z}}, \tag{4.6}$$

where $c_n = \sqrt{\frac{2\pi n}{a_z} - k^2}$ and K_0 is the modified Bessel function of the second kind, or

Macdonald function. The Macdonald function is exponentially decaying and propagating for real and imaginary arguments, respectively, so only the $n = 0$ term contributes in the far-field, as expected. The summation will converge quickly due to the exponential decay of the higher-order terms. In analogous fashion to sinusoids, the fields derived from this potential function will also show exponential convergence.

Eqs. 4.4-4.6 represent the simplest case of the more general Ewald technique that combines both spatial and spectral terms [96]. The purely spectral method will be sufficient for our purposes since meta-atoms are typically spaced below the Bragg diffraction limit at the frequencies of operation.

4.2 Polarizability Retrieval

The DDA is useful since it can accurately simulate a true physical system. It should also allow us to evaluate deviations from the optimum configuration present in our design. Such deviations can either stem from absorption in the meta-atoms, or constraints on material and fabrication that cause polarizabilities to deviate from the design value. It follows that we can only use the DDA for design if we can discern the polarizabilities of our elements in some fashion.

In conventional MM design, material parameters are often retrieved from numerical simulation. A number of methods are available to retrieve these parameters [97, 98, 33, 99, 100, 101, 102], but we will base our modified retrieval on the inversion of scattering parameter data [103, 104] based on the Nicholson-Ross-Weir (NWR) experimental extraction method [105, 106].

Essentially, the NWR method inverts the known dependence of the S-Matrix to the material parameters of a slab of thickness d. In simulation, this process is typically performed on an infinite 2D array of MM elements. For a 2D array, the slab "thickness" is not well-defined, but it is often considered to be equal to the lattice parameter of a 3D cubic array. Additionally, this process implicitly assumes that the

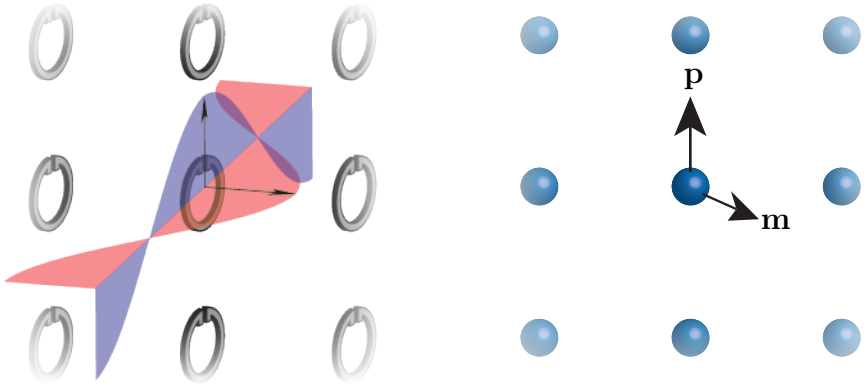

(a) Physical Scattering Problem (b) Point Dipole Response Approximation

effective material parameters are local, and seemingly unphysical artifacts appear in the retrieved parameters [107, 108, 109, 88].

One of the fundamental limitations of this process is that element interactions are only accounted for in two directions. The retrieved parameters from a one-unit-cell-thick slab therefore do not accurately reflect the behavior of a bulk array. Additional unit cells may be added in the third dimension, but this adds complexity to the retrieval [110] as well as substantial artifacts due to small numerical errors in the S-parameters [111, 112]. In order to mitigate this problem, we extract the individual elements directly from the response of the array [113, 114]. This method attempts to account for the interaction of all the elements in the array in a manner consistent with the point dipole model.

In Fig. 4.1(a) we plot a typical array of SRRs. We assume that the SRRs may be accurately modeled as zero-extent polarizable elements α_{yy}^{mm} and α_{zz}^{ee} such that the response is given by Fig. 4.1(b). A plane wave is incident as shown Fig. 4.1(a). Due to the symmetry of the problem, magnetic and electric dipole responses are decoupled, and we may consider them separately. The local field exciting a magnetic

element located at the origin is given by:

$$H_y^{loc}(0) = \mu_0^{-1} C_{yy}^{(2D)} m_y = \sum_{m=-\infty}^{\infty} \sum_{n=-\infty}^{\infty} G_{yy}(\mathbf{r}_{mn})\, m_y, \tag{4.7}$$

where $\mathbf{r}_{mn} = ma_y\hat{\mathbf{y}} + na_z\hat{\mathbf{z}}$ and $C_{yy}^{(2D)}$ is the interaction constant for the 2D array. As before, we seek a form more amenable to numerical computation. An explicit expression may be found in Appendix A. The form of $C_{zz}^{(2D)}$ is identical and is found immediately upon the substitution $(a_y, a_z) \rightarrow (a_z, a_y)$ in the expression for $C_{yy}^{(2D)}$.

We may incorporate all of these interactions simply via introducing an effective polarizability given by:

$$\tilde{\alpha}_{yy}^{mm} = \frac{\alpha_{yy}^{mm}}{1 - \mu_0^{-1} C_{yy}^{2D} \alpha_{yy}^{mm}}. \tag{4.8}$$

Far from the array plane at (x=0), we expect the electric and magnetic dipoles to radiate as electric and magnetic current sheets, respectively. The scattered electric fields at observation points $\pm d$ will therefore be:

$$E_z^{(s)}(x = \pm d) = \frac{j\omega}{2a_y a_z} \left(\eta p_z \mp m_y\right) e^{\mp jk_0 d}, \tag{4.9}$$

so that the S-parameters are given by:

$$\begin{aligned} S_{11} &= \frac{E_z^{(s)}}{E_z^{(0)}} = \frac{-j\omega}{2a_y a_z} \left(\eta \tilde{\alpha}_{zz}^{ee} - \eta^{-1} \tilde{\alpha}_{yy}^{mm}\right) e^{-j2k_0 d} \\ S_{21} &= \frac{E_z^{(0)} + E_z^{(s)}}{E_z^{(0)}} = \left(\frac{-j\omega}{2a_y a_z} \left(\eta \tilde{\alpha}_{zz}^{ee} + \eta^{-1} \tilde{\alpha}_{yy}^{mm}\right) + 1\right) e^{-j2k_0 d}. \end{aligned} \tag{4.10}$$

We recognize these as the S-parameter equations [103, 104] for a magneto-electric slab in the limit of vanishing thickness but nonzero polarization. It is a simple matter to invert these equations to arrive at our effective polarizabilities:

$$\tilde{\alpha}_{zz}^{ee} = j\frac{a_y a_z}{\omega\eta}\left(+S_{11} - S_{21} - 1\right)e^{j2k_0 d}$$
$$\tilde{\alpha}_{yy}^{mm} = -j\frac{a_y a_z \eta}{\omega}\left(1 + S_{11} + S_{21}\right)e^{j2k_0 d}. \tag{4.11}$$

Using Eq. 4.11 and the known interaction constants, we can discern the polarizabilities of the element. The clear limitation of this method is that the dipole must be spaced such that higher-order interactions are negligible. However, this method neatly side-steps the problem of interactions out-of-plane since these interactions will be automatically included in the DDA analysis of finite structures and in the Eigenmodal analysis presented in the next section.

4.3 Bloch Modes in a 3D Magnetic or Electric Lattice

Design, material, and fabricational constraints will force our meta-atoms to have a non-zero lattice spacing with respect to the wavelength. Limitations on available materials and fabricational tolerances will also require the meta-atoms to have some electrical size, which in turn enforces some minimum separation between elements. Additionally, the DDA formulation only considers dipolar interactions between meta-atoms. This requires considerable separation between adjacent elements to ensure that higher-order multipole coupling is negligible.

On the other hand, our polarizability prescriptions are based on the Clausius-Mossotti relationship which is applicable only in the limit of infinite wavelength and vanishing lattice constant. Therefore, it is natural to seek an improved formulation that considers both the discrete lattice spacing and finite wavelength. Draine et. al. [115] considered this problem for a dielectric-only lattice in an attempt to improve the accuracy of DDA simulations. They suggested a polarizability prescription such that the refractive index of an infinite lattice was the same as a continuous dielectric along the direction of a given incident wave $\mathbf{k}_0$. They showed improved accuracy in their

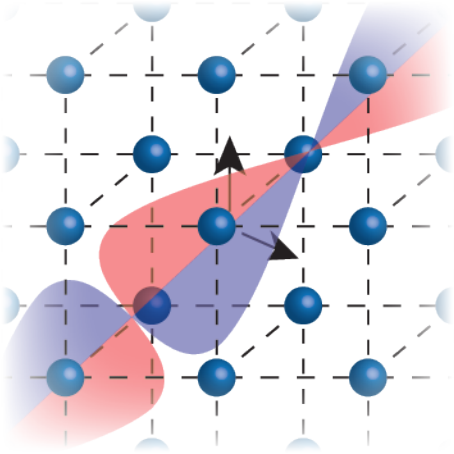

FIGURE 4.1: A 3D lattice of dipolar elements

simulations for modest lattice spacings and low-index materials. However, as the index increased, this approximation proved less useful since appreciable scattering occurred in directions removed from $\mathbf{k}_0$.

Clearly, Draine's prescription is not well-suited for TO design since we will inevitably require high indices of refraction. However, Draine's success emboldens us to proceed in a similar fashion. We will attempt to find a polarizability prescription that produces the same *anisotropic* index of refraction along the principal axes of our meta-atoms. Constraining ourselves to the principal axes will greatly simplify the derivation, and we will never be able to match the index in all directions as we approach the band-edge of our crystal lattice. We will begin by considering a purely magnetic lattice. Consider a 3D array of scatterers with polarizabilites a_{yy}^{mm} as shown in Fig. 4.3. We assume a wave propagate in $\mathbf{x}$, and the fields are TM^z. The local field acting on an element at the origin will consist of contributions from the 2D arrays of dipoles in the planes $x = \pm a_x, \pm 2a_x, \pm 3a_x$, etc., as well as those from the other dipoles in the array $x = 0$.

We have already determined the interaction constants for the dipoles in the plane $x = 0$, and we simply include them in a renormalized polarizability $\tilde{\alpha}_{yy}^{mm}$ as before.

We retain the dyadic subscripts since we anticipate that we will need to use other vector components later on. We now consider the contributions from dipoles in the other planes. The dipole moments in the other planes must obey the Bloch condition:

$$m_y\left(la_x\right) = m_y\left(0\right)e^{-jqa_x}, \tag{4.12}$$

where q is the unknown Bloch wave-number. The field exciting element at the origin is therefore

$$H_y'\left(0\right) = \mu_0^{-1}\sum_{l=-\infty}^{\infty}{}' G_{yy}\left(\mathbf{r}_{lmn}\right)m_y e^{(-jql_a x)}, \tag{4.13}$$

where the primes, ($'$), indicate that we are omitting the dipoles in the plane $x = 0$, and $\mathbf{r}_{lmn} = la_x\hat{\mathbf{x}} + ma_y\hat{\mathbf{y}} + na_z\hat{\mathbf{z}}$. The dispersion relation for this system is then

$$\left(\tilde{\alpha}_{yy}^{mm}\right)^{-1} - \mu_0^{-1}C_{yy}^{(3)} = 0, \tag{4.14}$$

where $C_{yy}^{(3)}$ is given by equation A.15 for a unit dipole. Clearly, we cannot use an unmodified version of the triply-periodic Green's function represented by Eq. A.15 since q is unknown. Instead, we use techniques similar to those described the previous section to obtain an alternative form:

$$\begin{aligned} C_{yy}^{(3)} = \\ \frac{1}{2\pi a_y}\sum_{n=-\infty}^{\infty}\sum_{m=-\infty}^{\infty}{}'\sum_{l=-\infty}^{\infty}{}'\left[k^2 - \left(\frac{2\pi m}{a_y}\right)^2\right]K_0\left(c_m\Gamma_{ln}\right)e^{-jqla_x} \\ + \frac{k^2}{2a_y a_z}\sum_{n=-\infty}^{\infty}{}'\sum_{l=-\infty}^{\infty}{}'\frac{e^{-c_n|l|a_x - jqla_x}}{c_n} \\ + \frac{k}{2a_y a_z}\frac{\sin ka_x}{\cos ka_x - \cos qa_x}. \end{aligned} \tag{4.15}$$

The derivation of Eq. 4.15 is given in the appendix Eq. A. Surprisingly, the complicated expression for C_{yy}^{mm} will give us some insight into the behavior of the system.

The first two lines represent the contributions from evanescent waves generated by the completed dipole arrays. The last line represents the contributions from homogeneous plane waves generated by sheets of dipolar current $jm_y/(a_y a_z)$. For $ax \gg ay, az$ we find that the dispersion relation reduces to:

$$\cos qa_x = \cos ka_x - \frac{\tilde{\alpha}_y^m \omega}{2\eta a_y a_z} \sin ka_x, \tag{4.16}$$

which is equivalent to Eq. 13 in [88]. It is also straightforward to show that Eq. 4.15 reduces to the static interaction constant of a 3D dipole array given in [116] in the limit $qa_x \to 0$.

Unsurprisingly, the phase delay between adjacent planes of dipoles introduces spatial dispersion into the model. However can now use Eq. 4.15 and Eq. 4.14 to determine the effective index $n \equiv q/k_0$ for a given lattice and polarizability. Alternatively, we can use the equations to find the polarizability that gives us $n = \sqrt{\mu_r}$, where μ_r is the desired effective permeability. We expect that using this corrected polarizability for a given lattice spacing will more closely resemble a continuous medium of relative permeability μ_r then when the polarizability assigned by Clausius-Mossotti. The DDA, in turn, can be used to assess this improvement.

In Fig. 4.2, we compare DDA simulations of magnetic cylinders with and without this correction. The lattice spacing of $a = \lambda_0/10$ represents a typical spacing of meta-atoms. We see that the forward SCS of the uncorrected model yields a five-dB error for the relatively modest permeablity $\mu_r = 4$. The nonlocal correction yields a two-dB error in the same direction. This is some improvement, but it is probably insufficient for most designs.

This error persists for two reasons. The first is spatial dispersion: even though we have corrected the refractive index along the principal axes of our lattice, we can not force the isofrequency contours to be correct for all $\mathbf{q}$. However, we do not expect this to be a large source of error, since the dispersion remains quite

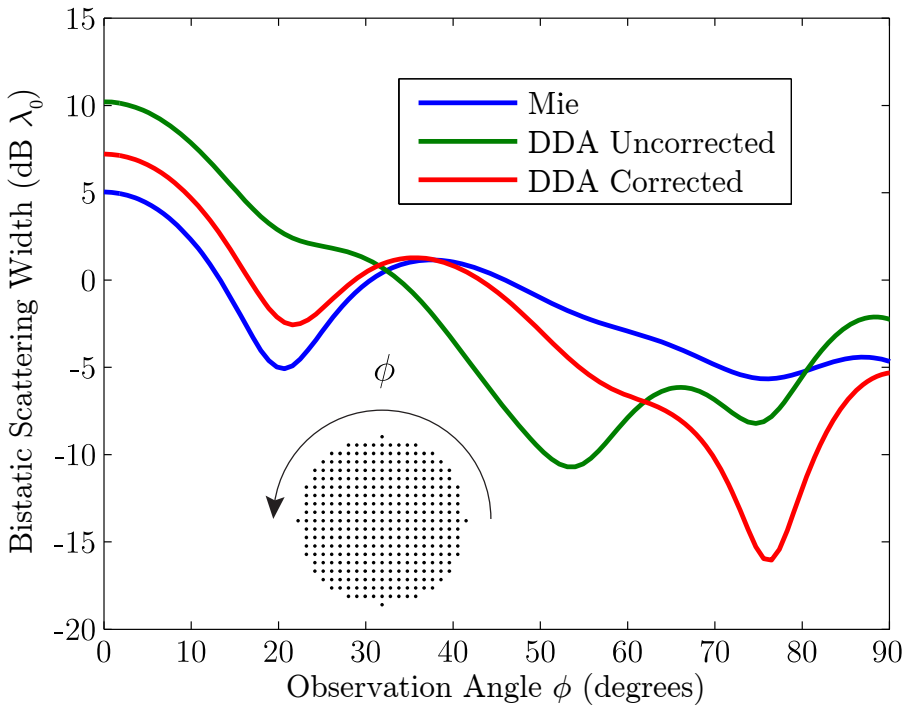

FIGURE 4.2: Comparison of simulated magnetic cylinders with nonlocality corrections. The simulated cylinder had a radius $R = \lambda_0$ and $\mu_r = 4$. The lattice constant for the DDA simulations was $a = \lambda_0/10$.

elliptical even as we approach the band-edge [87]. Instead, we attribute most of the error to the electromagnetic interactions at the boundary of the cylinder. The electromagnetic environment for the meta-atoms at the boundary differs considerably from those deep in the interior. These boundary elements are often termed Drude transition layers [117], and their effective properties can be drastically different from the interior, especially when the polarizability of the atoms is considerable. Moreover, as we leave the effective-medium limit, we lose the concept of a well-defined wave impedance [34, 118, 85], and scattering at the surface will be somewhat unpredictable. This is seen in Fig. 4.2, as we now explain. The nonlocal correction gives the most improvement in the forward SCS, and agreement worsens as the observation angle increases. In a transparent material, the forward SCS is primarily determined by the phase delay of the wave transmitted through the material. However, reflections play

a more prominent role as we move away from the forward direction. Therefore, we expect that our correction will quickly yield diminishing returns as the polarizabilities become more extreme.

However, this correction may still prove a good initial step towards intelligent optimization of devices, especially when used in conjunction with DDA analysis. If the primary error in our prescription is due to error at the surface, then it behooves us to concentrate our optimization efforts on the surface polarizabilties and assign the polarizabilities using our method. We will show the validity of this method in the next section after we develop a more general model suitable for TO design.

4.4 Bloch Modes in a 3D Magnetic-electric Lattice

Our analysis for the magneto-electric case will proceed in a similar fashion to the previous section. However, we may no longer consider the magnetic and electric interaction constants separately since we are no longer guaranteed that magnetic and electric elements will not interact. In fact, it has been shown in [88] that infinite arrays of magnetoelectric sheets will exhibit a nonlocal bianisotropic response due their nonvanishing separation. Our treatment will show a similar bianisotropy encapsulated by a magneto-electric dynamic interaction constant.

Following the methods of the previous section, we find local magnetic and electric fields at the origin are given by:

$$H_y'(0) = \sum_{l=-\infty}^{\infty}{}' \sum_{m=-\infty}^{\infty} \sum_{n=-\infty}^{\infty} \left[G_{yz}^{me}(\mathbf{r}_{lmn})\, p_z + \mu_0^{-1} G_{yy}(\mathbf{r}_{lmn})\, m_y \right] e^{(-jql_a x)} \tag{4.17a}$$

$$E_z'(0) = \sum_{l=-\infty}^{\infty}{}' \sum_{m=-\infty}^{\infty} \sum_{n=-\infty}^{\infty} \left[G_{zy}^{em}(\mathbf{r}_{lmn})\, p_z + \varepsilon_0^{-1} G_{zz}(\mathbf{r}_{lmn})\, m_y \right] e^{(-jql_a x)}. \tag{4.17b}$$

This system of equations may be written more compactly as:

$$\begin{bmatrix} \mu_0^{-1} C_{yy}^{(3)}(q) - \left(\tilde{\alpha}_{yy}^{mm}\right)^{-1} & C_{yz}^{me}(q) \\ C_{zy}^{em}(q) & \varepsilon_0^{-1} C_{zz}^{(3)}(q) - \left(\tilde{\alpha}_{zz}^{ee}\right)^{-1} \end{bmatrix} \begin{bmatrix} m_y \\ p_z \end{bmatrix} = \mathbf{0}, \tag{4.18}$$

where $C_{yy}^{(3)}$ and $C_{zz}^{(3)}$ are given as before, and $C_{yz}^{me} = C_{zy}^{em}$ as required by reciprocity. Once again, we develop our expression for C_{zy}^{em} in the appendix. The final expression is:

$$\begin{aligned} C_{zy}^{em} = -j\omega \frac{\partial G_y}{\partial x} = -\frac{j\omega a_x}{2\pi a_y} \sum_{n=-\infty}^{\infty} \sum_{m=-\infty}^{\infty}{}' \sum_{l=-\infty}^{\infty}{}' e^{-jqla_x} \frac{c_m l K_1(c_m \Gamma_{ln})}{\Gamma_{ln}} \\ -\frac{j\omega}{2a_y a_z} \sum_{n=-\infty}^{\infty}{}' \sum_{l=-\infty}^{\infty}{}' \operatorname{sgn}(l)\, e^{-c_n \Gamma_{ln}} e^{-jqla_x} \\ +\frac{\omega}{2a_y a_z} \frac{\sin qa_x}{\cos ka_x - \cos qa_x}. \end{aligned} \tag{4.19}$$

As before, we see that the interaction consists of both homogenous and inhomogeneous plane-wave terms. However, in the limit $q_a x \to 0$, the evanescent terms become the antisymmetric function in l, and these terms vanish identically.

We find the dispersion relation for this system by enforcing $|\mathbf{C}| = 0$:

$$\left[\mu_0^{-1} C_{yy}^{(3D)}(q) - \left(\tilde{\alpha}_{yy}^{mm}\right)^{-1}\right] \left[\varepsilon_0^{-1} C_{zz}^{(3D)}(q) - (\tilde{\alpha}_{zz}^{ee})^{-1}\right] - \left(C_{zy}^{me}\right)^2 = 0. \tag{4.20}$$

Once again, we must resort to numerical techniques to find the $q(\omega)$. Some simplification is possible if we assume the plane-wave interaction dominates, in which case Eq. 4.20 reduces to:

$$\begin{aligned} \cos qa_x = \cos ka_x - \frac{\omega}{4a_y a_z} \left(\tilde{\alpha}^e \eta^2 + \tilde{\alpha}^m\right) \sin^2 ka_x \\ \pm \frac{\omega}{2a_y a_z} \sqrt{\left(\tilde{\alpha}^e \eta^2 - \tilde{\alpha}^m\right)^2 \sin^2 ka_x + \tilde{\alpha}^e \tilde{\alpha}^m \sin^2 qa_x}, \end{aligned} \tag{4.21}$$

which is equivalent to Eq. 49 in [88]. We verify our derivation via application to

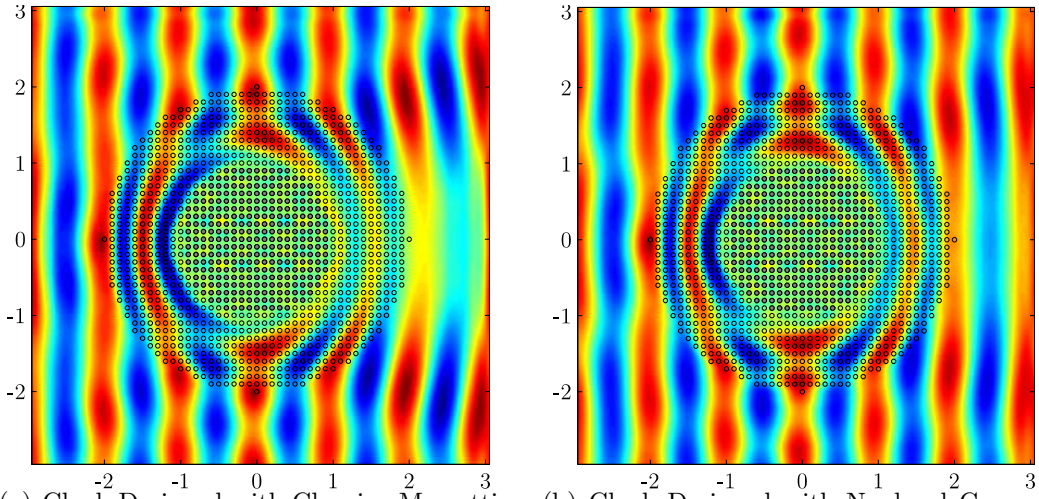

(a) Cloak Designed with Clausius Mossotti (b) Cloak Designed with Nonlocal Corrections

FIGURE 4.3: (a) DDA simulation of a cloak designed with Clausius-Mossotti. (b) The same simulation but with polarizabilities corrected to account for nonlocal wave interactions. The shaded circles represent the quasi-PEC dipoles that comprise the cloaked object.

a TO device. For a cylindrical cloak of inner radius R_1 and outer radius R_2, the relevant material parameters are:

$$\begin{aligned} \varepsilon_z &= \left(\frac{R_2}{R2 - R_1}\right)\frac{\rho - R_1}{\rho} \\ \mu_\phi &= \frac{\rho - R_1}{\rho} \\ \mu_\rho &= \frac{\rho}{\rho - R_1}. \end{aligned} \tag{4.22}$$

Assuming our elements lay in a cubic array of lattice constant a, the polarizabilites at each site may be determined by inserting Eq. 4.22 into the Clausius-Mossotti equation. We plot the simulated results from such a device on the left of Fig. 4.3. We have included highly conductive elements the interior of the cloak to create a quasi-PEC scatterer. We see cloaking performance is poor even for the relatively modest lattice spacing of $a = \lambda_0/10$. By eye, it seems that the phase fronts are not properly combined upon exiting the cloak. Instead, the transmitted waves appear

to be "refracted" at an angle away from the incident direction. This indicates that the locally-varying anisotropic index of refraction is not correct. Since phase error accumulates as the wave traverses the cloaking volume, it is most apparent as it exits on the right. Fig. 4.4 also shows performance continues to degrade as the electrical size of the cloak is increased and the phase errors increase.

In order to correct these aberrations, we must first define a locally-varying, anisotropic index of refraction $n\left(\hat{\mathbf{q}}\right)$ such that

$$\begin{aligned} n\left(\rho, \hat{\mathbf{q}} = \hat{\boldsymbol{\rho}}\right) &= \sqrt{\varepsilon_z \mu_\phi} \\ n\left(\rho, \hat{\mathbf{q}} = \hat{\boldsymbol{\phi}}\right) &= \sqrt{\varepsilon_z \mu_\rho}. \end{aligned} \tag{4.23}$$

This definition immediately implies that we are in the eikonal limit and such a prescription is valid. We may then numerically invert Eq. 4.20 to find the polarizabilities that yield the correct n. For simplicitly, we use α_z^e as specified by Clausius-Mossotti, and solve for α_ϕ^m or α_ρ^m. Fixing α_z^e in this fashion guarantees that we will converge to the quasi-static solution as a is decreased. We plot the simulated results on the right hand side of Fig. 4.3. We immediately see improved cloaking performance: the wave fronts are properly combined upon exiting the cloak on the right, although a faint shadow is still visible. The performance improvement is confirmed when we calculate the scattering-cross section for both designs in Fig. 4.4. The SCS has been normalized to that of the quasi-PEC core, and thus the corrected cloak has a normalized SCS of 0.25, whereas the uncorrected cloak has an SCS of 0.80. Additionally, the corrected cloaking performance is quite consistent as the size of the cloak is decreased. We expect that performance will eventually degrade as the cloak size is increased due to residual scattering from the surface and small errors in the refractive index.

Despite these small imperfections, our results clearly demonstrate improved performance over a conventional cloaking design. Since we can only rigourously specify the index of refraction in one direction, we expect that this method would be more

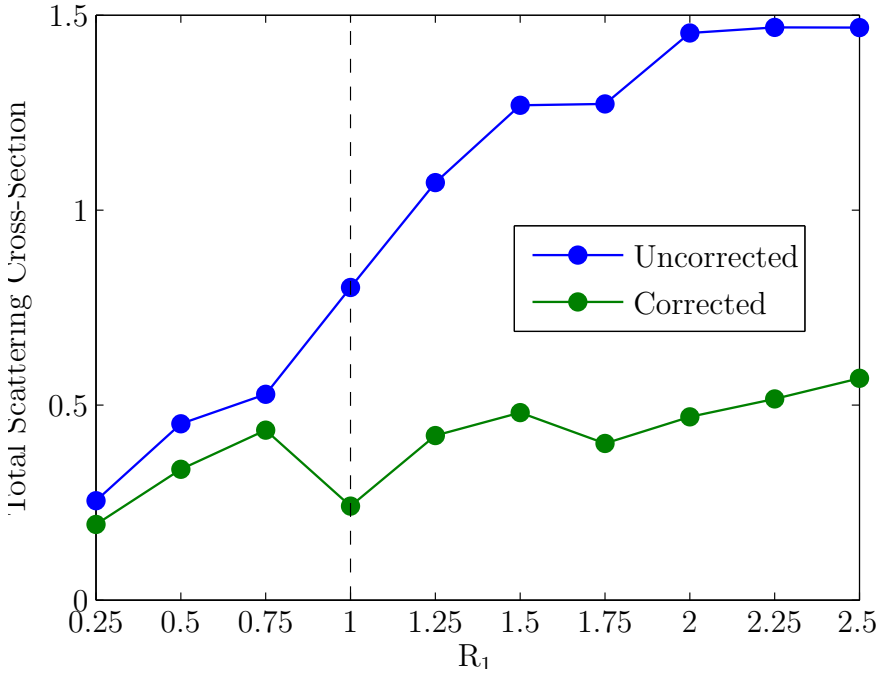

FIGURE 4.4: Cross-Section Comparison of Cloaks with- and without- corrections. The vertical dashed line indicates the cloaks simulated in Fig. 4.3

ideally suited for the unidirectional design of Chapter. 3. However, the cylindrical design presented above could certainly be used as the basis for further numerical optimization.

4.5 Extensions for the DDA

Our formulation for the DDA makes several assumptions. Specifically, it assumes that elements only interact via their dipolar responses, and that the excitation fields are uniform over the element volume. To ensure the validity of these assumptions, we require highly sub-wavelength elements that are separated by distances that are at least comparable to the element size. Highly sub-wavelength elements in turn require very fine features, and the relatively large element spacing will dilute the material response. We therefore seek improvements to our approximation that would allow us to use larger elements in close proximity.

One solution is to incorporate the interaction of higher-order multipoles into the DDA. This was pursued in [119], but we note that their analysis was restricted to spherical elements for which the induced quadrupoles could be calculated analytically. Additionally, higher-order terms will inevitably increase the numerical complexity of the problem, which in turn decreases the advantages gained using our method. Instead, we consider improvements to our approximations that stem from additional knowledge about the meta-atoms themselves.

For instance, many meta-atoms consist of simple shapes arrayed in some regular pattern. If we once again restrict ourselves to the quasi-static regime, then we can make use of the physical models of the elements themselves to increase the accuracy of our simulations *without* increasing the number of interacting terms. We now discuss two specific examples to clarify our method.

4.5.1 Coaxial Ring Resonators

Consider a loop of area $S_1 = \pi R_1^2$. A uniform incident H-field induces an EMF:

$$V_{ind} = -j\omega\mu_0 H_0 S_1 = j\omega L_1 I + I R_r. \tag{4.24}$$

The polarizability is therefore:

$$\alpha = \frac{I_1 S_1}{H_0} = -\frac{j\omega\mu_0 S_1^2}{Rr + j\omega L_1}. \tag{4.25}$$

If we introduce another loop $S_2 = \pi R_2^2$, this will also contribute some flux:

$$\begin{array}{l} V_0(r_1) - j\omega\mu_0 \int \mathbf{H}_{12} \cdot dS_1 = I_1 Z_{11}, \\ V_0(r_2) - j\omega\mu_0 \int \mathbf{H}_{21} \cdot dS_2 = I_2 Z_{22}. \end{array} \tag{4.26}$$

From reciprocity, the mutual impedances are the same, and we have:

$$Z_{12} = j\omega M_{12} = j\omega\mu_0 \int \mathbf{H}_{12} \cdot dS_1, \tag{4.27}$$

$$M_{12} = \mu_0 \oint \left[\int \bar{\bar{\mathbf{G}}} \mathbf{I}_2 \right] \cdot \mathbf{S}_1. \tag{4.28}$$

In this context, the DDA assumes that the distance between loops r_{12} is sufficiently great that the field originating form the second loop is uniform over the first loop, (and vice-versa). However, this may fail when the two loops are very close to one another. When the loops are positioned arbitrarily, we are forced to evaluate Eq. 4.28 explicitly. Fortunately, in most real circumstances, the loops will be positioned with some sort of regularity. Specifically, if the two loops are positioned coaxially, we may approximate this term analytically.

If $r_{12} \ll \lambda_0$, Eq. 4.28 reduces to the Nuemann form, and the mutual inductance has the analytical solution:

$$M_{12}^{QS} = \mu_0 \sqrt{R_1 R_2} \left[\left(\frac{2}{k} - k \right) K(\kappa) - \frac{2}{k} E(\kappa) \right] \tag{4.29}$$

where

$$\kappa^2 = \frac{4 R_1 R_2}{r_{12}^2 + (R_1 + R_2)^2}, \tag{4.30}$$

and K() and E() are the complete elliptical integrals of the first and second kind, respectively.

In the DDA, the mutual inductance term is given by:

$$M_{12}^{DDA} = \frac{\mu_0}{2\pi} \frac{e^{-jk_0 r_{12}}}{r_{12}} \left(\frac{jk_0}{r_{12}} + \frac{1}{r_{12}^2} \right) S_1 S_2. \tag{4.31}$$

We note that in the same quasi-static approximation, Eq. 4.31 reduces to:

$$M_{12}^{DDA,near} \approx \frac{\mu_0}{2\pi} \frac{1}{r_{12}^3} S_1 S_2. \tag{4.32}$$

Conversely, if we are at large distances, $\kappa^2 \approx 4R_1R_2/r_{12}$ the asymptotic forms for $K(\kappa)$ and $E(\kappa)$ yield:

$$M_{12}^{QS,far} \approx \frac{\mu_0}{2\pi}\frac{1}{r_{12}^3}S_1S_2 \tag{4.33}$$

This suggests that we should use:

$$M_{12}^{DDA+QS} = M_{12}^{QS}e^{-jk_0r_{12}} + \frac{jk_0\mu_0}{\pi}\frac{e^{-jk0r_{12}}}{r_{12}^2}S_1S_2 \tag{4.34}$$

to improve the accuracy of our simulations. Using this circuit analysis, and restricting ourselves to the scalar magnetic problem, we can rewrite the DDA equation 4.2 as:

$$I_iZ_i = V_0(r_i) - \sum_j I_jZ_{ij}. \tag{4.35}$$

We would like to be able to incorporate this correction directly into our DDA equation. We therefore define the effective interaction term:

$$\tilde{G}_{ij} = \frac{M_{ij}}{S_iS_j}, \tag{4.36}$$

which differs from the regular DDA equation only for coaxial resonators.

We evaluate our method by simulating a 2D infinite array of loops and extracting the polarizabilities for various separations a_y[1]. We perform this extraction with both the conventional interaction constant C, and one that incorporates our modifications, (derivation in the appendix A). We expect that the conventional polarizability retrieval will fail when the loops are tightly packed. This error will manifest as a variation of the retrieved polarizability as a function of a_y. On the other hand, our modified interaction $\tilde{C}$ should show little- to no-variation. These expectations are

[1] We simulate the full array rather than two loops in isolation since the port boundaries are perfectly matched for homogeneous plane waves, and the higher-order modes fall off exponentially away from the array. By comparison, the scattered fields from two isolated loops would only fall off as r^2, and we would be forced to increase the size of the calculation domain to compensate for these imperfect absorbing boundaries.

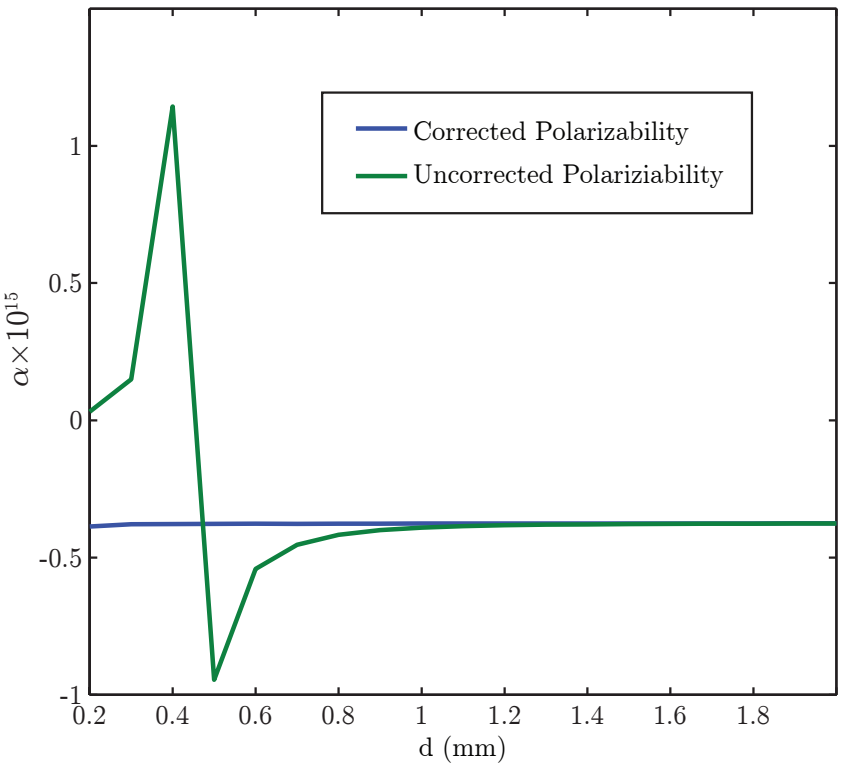

FIGURE 4.5: Comparisons of retrieved polarizabilities with and without corrections to the mutual inductance between loops.

confirmed in Fig. 4.5. The conventional method begins to fail when the separation is about one loop radius. Past that point, the retrieved polarizability varies rapidly and even changes signs as the separation becomes substantially smaller than r. On the other hand, the polarizability retrieved via our corrected method is virtually unchanged for all simulated separations. We note a slight deviation in the retrieval when the separation is very small; the self-inductance of the loop is no longer well-represented by that of an isolated loop, and the finite trace width becomes significant.

4.6 Conclusions

In this Chapter, we have developed the idea of using DDA analysis for metametarial elements. We have shown that the DDA can be used to diagnose some of the artifacts that occur when we violate the limits of our quasi-static approximations. However, we have also shown that the DDA is more than a simple diagnostic tool. Using the dipolar model, we have developed a method of design that begins to correct some of these troubling artifacts. Moreover, we have shown that the DDA is amenable to additional manipulation that allows us to use our own physical insight as a guide to increase the accuracy of our simulations. Specifically:

- I have improved upon the 2D-DDA method introduced by Bowen et. al.[86] by incorporating acceleration techniques for Green's functions and self-interaction terms.
  - Future work would to extend the magneto-electric DDA to optically-large, 3D structures. This is a challenging problem since it involves the solution of a dense system of linear equations. Iterative methods may be used for larger domains [120], but to our knowledge, these methods have not been applied to the analysis of TO structures.
- I derived an expression for the Bloch modes in a lattice of magneto-electric point dipoles. I used this dispersion relation to calculate corrections to the assigned polarizabilities in a metamaterial cloak. For optically large cloaks, ($R_1 \geqslant 1$), this correction allows for over a 50% reduction in total scattering cross-section.
  - Future work would include designing a specific metamaterial unit cell and phyisical implementation of the corrected design. Since the corrections are small for a $\lambda_0/10$ spacing, I would attempt to use even larger unit

cells so that the correction is larger, and therefore hopefully less sensitive to realistic design tolerances.

- I have shown that the DDA can be generalized to include knowledge of the quasistatic interactions between canonical geometries. I demonstrated the accuracy of this technique by retrieving the correct polarizability from a dense array of split-ring resonators.
  - Future work would extend this method to capacitively-coupled resonators.
  - Future work would also use this method for the design and analysis of a physical TO optic.

5

Complementary Metamaterial Devices

5.1 Introduction

In this chapter, I make the following contributions to the study of complementary metamaterials (C-MMs):

- I examine Babinet's principle and apply it to the analysis of C-MMs. I discuss the limitations of this approach and I introduce an alternative circuit model based on fictitious magnetic currents.

- I extend the polarizability retrieval method of Scher et. al. [113] to complementary metamaterials. I verify the validity of this approach by retrieving polarizabilities from C-MM structures in full-wave numerical simulations.

- I modify the DDA method of Chapter 4 to the analysis of C-MM TO structures. I demonstrate the accuracy of this method by comparing my DDA simulations to results from full-wave simulations.

- I use my modified DDA algorithm to analyze TO devices implemented with C-MMs. I demonstrate that the tendency of C-MMs to scatter into free-space

modes limits their utility in TO device design.

5.2 Complementary Metamaterials

In 1944, Hans Bethe considered the electromagnetic problem of diffraction through an electrically small aperture in a conducting plane [121]. By introducing fictitious magnetic currents and charges in place of the aperture, he concluded that he could assign both magnetic and electric polarizabilities to the aperture, and that the transmitted field could be determined by the dipole moments induced by the incident field. This theory has since been generalized to apertures of arbitrary shape [116], and apertures have found use both as couplers [122, 123] and frequency selective surfaces [124].

However, these apertures did not enter the realm of metamaterials until 2004. Falcone et. al. used Babinet's principle to show that apertures patterned in the shape of split ring resonators would provide a resonant *electric* response [125]. This greatly simplified the analysis of these apertures since the theory was able to bring to bear all of prior research on conventional metamaterials and metasurfaces. We label these elements complementary metamaterials (C-MMs) to highlight this duality. It has since been shown that the complements of electrically-coupled elements similarly provide a magnetic response [126]. This latter result has generated a great deal of interest since it introduced a straightforward means of providing a relatively broadband paramagnetic response, a feature split-ring resonators lack. For instance, Yang et. al used a complementary metamaterial to both miniaturize and increase the performance of a conventional microstrip antenna [127].

The duality between conventional metamaterials and CMMs is a bit more complex than the simple exchange of the effective material tensors $\bar{\bar{\boldsymbol{\varepsilon}}}$ and $\bar{\bar{\boldsymbol{\mu}}}$. We illustrate some of these new complexities via a concrete example. The complementary split-ring resonator (C-SRR) introduced by Falcone et. al. [125] was the first example of a complementery metamaterial, so we will use it as a tool in our analsyis. We will

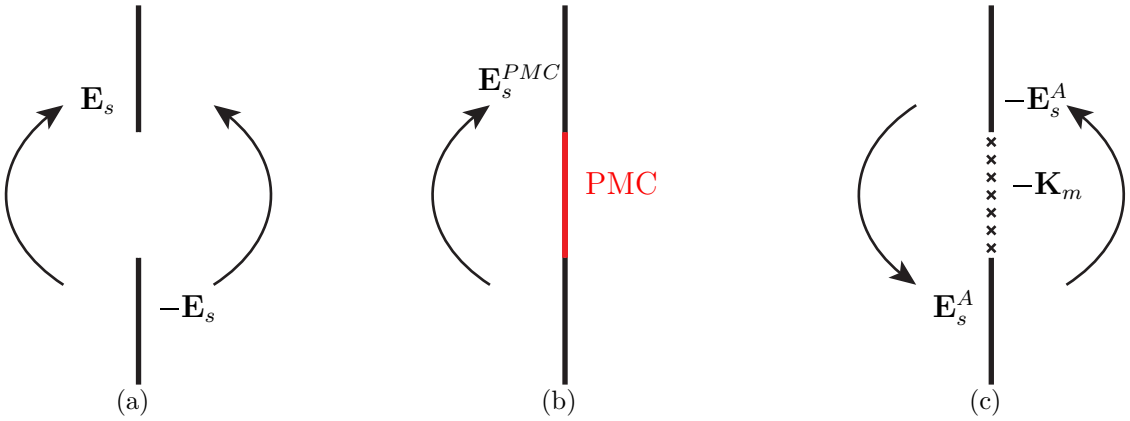

FIGURE 5.1: (a) Field scattered from an aperture in a PEC plane. (b) Fields scattered from a PMC surface of the same dimensions embedded in a PEC plane. (c) Fields radiated by a magnetic surface current source $-\mathbf{K}_m$.

first analyze this structure in terms of Babinet's principle, and we will show that Babinet's principle limited in it's applicability. To over come the limits of such a model, present an analysis based on an equivalent circuit model. Finally, we will examine some subtlties that arise from our point-dipole description of the aperture

5.2.1 Babinet's Principle in Electromagnetism

Consider the aperture in a PEC plane as shown in Fig. 5.1(a). An electromagnetic wave is incident from the left, causing currents to flow in the PEC, which in turn generate fields on both sides of the aperture. We begin by filling the aperture with a fictitious magnetic conductor (PMC) as shown in Fig. 5.1(b)The boundary conditions on the PMC surface are:

$$\hat{\mathbf{n}} \times \mathbf{H}_0 = -\hat{\mathbf{n}} \times \mathbf{H}_s^{PMC} \tag{5.1a}$$

$$\hat{\mathbf{n}} \cdot \mathbf{E}_0 = -\hat{\mathbf{n}} \cdot \mathbf{E}_s^{PMC}, \tag{5.1b}$$

where $\hat{\mathbf{n}}$ is taken as the surface normal pointing left. The scattered fields are determined by the induced magnetic currents and charges on the PMC:

$$\rho_m = \hat{\mathbf{n}} \cdot \mathbf{B}_s^{PMC} \tag{5.2a}$$

$$\mathbf{K}_m = -\hat{\mathbf{n}} \times \mathbf{E}_s^{PMC}. \tag{5.2b}$$

If we now open the aperture, we see that these fields no longer satisfy the boundary conditions of the problem. For instance, $\hat{\mathbf{n}} \times \mathbf{E}$ is not continuous across the aperture. However, if we place a magnetic current source $-\mathbf{K}_m$ in the *open* aperture, then we have:

$$\hat{\mathbf{n}} \times \mathbf{H}_1^A = \hat{\mathbf{n}} \times \mathbf{H}_2^A \tag{5.3a}$$

$$-\mathbf{K}_m = -\hat{\mathbf{n}} \times \left(\mathbf{E}_2^A - \mathbf{E}_1^A\right). \tag{5.3b}$$

If we combine the fields scattered by the PMC surface with the fields radiated by the current source $-\mathbf{K}_m$, we have:

$$\hat{\mathbf{n}} \times \left(\mathbf{H}_0 + \mathbf{H}_s^{PMC} + \mathbf{H}_1^A\right) = \hat{\mathbf{n}} \times \mathbf{H}_2^A \tag{5.4a}$$

$$\hat{\mathbf{n}} \times \left(\mathbf{E}_0 + \mathbf{E}_s^{PMC} + \mathbf{E}_1^A\right) = \hat{\mathbf{n}} \times \mathbf{E}_2^A. \tag{5.4b}$$

Referring to Eq. 5.4a, the tangential components of $\mathbf{H}^{PMC} = \mathbf{H}_0 + \mathbf{H}_s^{PMC}$ are identically zero according to 5.1a, so Eq. 5.4a reduces to Eq. 5.3a and we have preserved continuity of $\mathbf{H}$. Similarly, combining Eq. 5.2b and Eq. 5.3b yields $\mathbf{E}_s^{PMC} = \mathbf{E}_1 - \mathbf{E}_2$. Inserting this into Eq. 5.4b shows that tangential $\mathbf{E}$ is likewise preserved. We have therefore found a solution that obeys the imposed boundary conditions, and uniqueness ensures that our solution is the only one.

The preceding derivation is equivalent to Babinet's principle, but we have not related the scattering of the aperture directly to the scattering from a conventional structure. However, for the special case that the material parameters are the same on both sides of the aperture, we have $\mathbf{E}_1^A = -\mathbf{E}_2^A$, and the total scattered field is shown to be $\mathbf{E}_s = \pm\mathbf{E}_s^{PMC}/2$, and similarly for $\mathbf{H}_s$. Since the scattered aperture

fields are one-half those of the shaped PMC surface, we conclude that the scattering characteristics will be dual to a PEC scatterer of the same geometry. Explicitly, for the case of a flat, PEC SRR, the magnetic dipole moment is given by:

$$\mathbf{m} = \int \mathbf{r} \times \mathbf{K} dS, \tag{5.5}$$

where $\mathbf{K}$ is the electric surface current. For the PMC case, the *electric* dipole moment is given by:

$$\mathbf{p} = \int \mathbf{r} \times \mathbf{K}_m dS. \tag{5.6}$$

A similar relationship holds for the electric dipole moment of the SRR and the magnetic moment of the PMC SRR. The complementary SRR (C-SRR) scatters as a magnetic dipole of half the strength of the electric dipole moment of the SRR.

5.2.2 Quasi-static Model of a Complementary Split-Ring Resonator

While Babinet's principle provides a rigorous theoretical basis for properties of complementary metamaterials, it is somewhat difficult to extract a meaningful cause-and-effect relationship between the incident field and scattering properties of the apertures through that principle alone. Additionally, we only obtain an explicit relationship between the aperture and its complement when the materials are the same on both sides of the aperture. In reality, these apertures will be typically be fabricated on a substrate, and the dielectric function will suffer a large discontinuity directly at the aperture surface. Finally, we cannot immediately ascribe effective medium properties to an array of such apertures, since the effective dipole moments exist in the presence of an infinite PEC surface. This PEC surface must be accounted for in some manner in our homogenization scheme.

Owing to these limitations, We would prefer to develop our understanding by creating quasi-static circuit models as has been done for conventional metamateri-

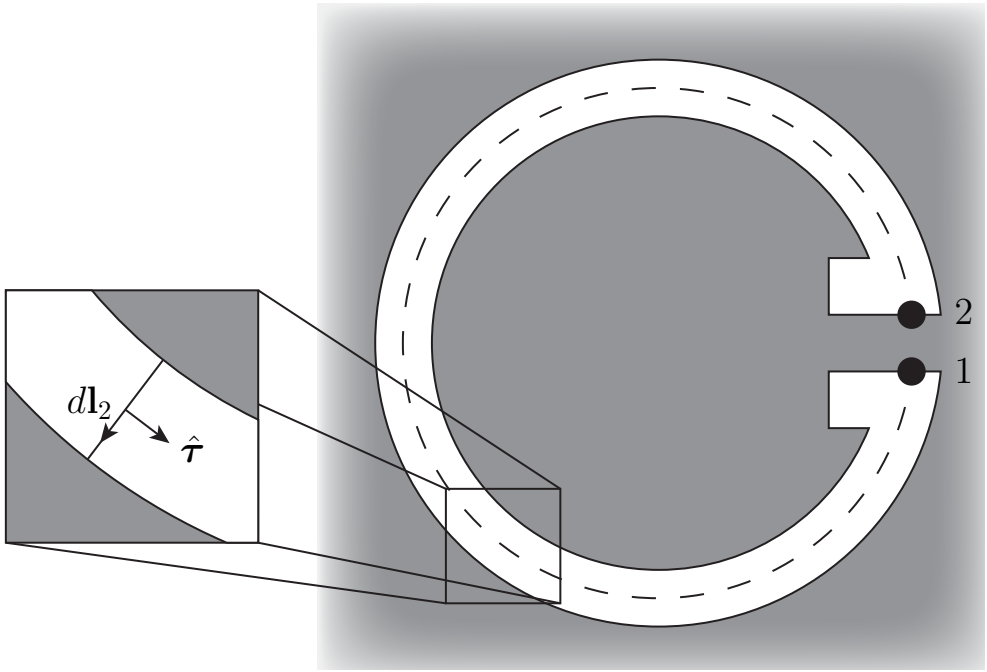

FIGURE 5.2: A C-SRR showing the integration contour for our circuit analysis.

als elements. Our development parallels the derivation that we presented for the convectional SRR in Section 1.2.

When an incident electromagnetic wave encounters the aperture, electric and magnetic fields develop to satisfy the boundary conditions presented. In particular, in-plane electric fields and out-of-plane magnetic fields must exist to satisfy the Dirichlet boundary conditions on the tangential and normal components of $\mathbf{H}$ and $\mathbf{E}$, respectively.

On the source-free aperture surface, $\nabla \cdot \mathbf{D} = 0$ and $\mathbf{D}$ may be written as the curl of an auxiliary vector potential $\mathbf{F}$ [26]. It follows that:

$$\mathbf{H}_0 + \mathbf{H}_s = \mathbf{H}_0 - \nabla\phi_m^s - j\omega\mathbf{F}_s = \mathbf{0}. \tag{5.7}$$

In order to obtain a cause-and-effect relationship as before, we integrate from points 1 to 2 as indicated Fig. 5.2:

$$\int_1^2 \mathbf{H}_0 \cdot d\mathbf{l} = \int_1^2 \nabla\phi_m^s \cdot d\mathbf{l} + j\omega \int_1^2 \mathbf{F}_s \cdot d\mathbf{l}. \tag{5.8}$$

The first term on the LHS,

$$\int_1^2 \mathbf{H}_0 \cdot d\mathbf{l}, \tag{5.9}$$

once again represents the source. We now assume that we can close the integral in E without effecting its solution, (the integration of $\mathbf{H}_0$ over the narrow PEC "gap" is negligible). We can then use Stoke's theorem and Ampere's law to find:

$$\int \mathbf{H}_0 \cdot d\mathbf{l} = j\omega \int \mathbf{D}_0 \cdot \mathbf{dS}. \tag{5.10}$$

We note that this still holds when there are currents associated with the incident field, (such as in a parallel plate), since they will be confined to the plane. Upon comparison of Eq. 5.10 and Eq. 1.7, we see that the source in the C-SRR is indeed the electric field as the magnetic field is considered the source in the conventional SRR.

We now move on to the first term on the RHS. Once more assume that we can close the integral without perturbing our solution. We find that:

$$j\omega \oint \mathbf{F} \cdot d\mathbf{l} = j\omega \int \nabla \times \mathbf{F} \cdot d\mathbf{S} = j\omega \int \mathbf{D} \cdot d\mathbf{S}. \tag{5.11}$$

The term on the RHS is the "electrical flux" through our circuit. However, this term presents a complication: $\mathbf{D}$ is abruptly discontinuous on the PEC surface, and our flux calculation will differ depending on which side of the surface we choose to perform the calculation. This is an important aspect of our description, as the circuit will only present a self-consistent solution on the side that we perform our calculations. We must therefore take care to specify the proper surface normal and half-space in our analysis.

With this complication in mind, we define our "electrical inductance" as:

$$L_e = j\omega \frac{\int \mathbf{D} \cdot \hat{\mathbf{n}} dS}{I_m}, \tag{5.12}$$

where we have introduced the "magnetic current" I_m. We have used the concept of magnetic current already in our development of Babinet's principle, but we now explore the concept a bit farther. To explicitly calculate I_m from its definition in Eq. 5.2b:

$$I_m = \int \mathbf{K}_m \cdot \hat{\boldsymbol{\tau}} dl = -\int (\hat{\mathbf{n}} \times \mathbf{E}_s) \cdot \hat{\boldsymbol{\tau}} dl = -\int E_s \cdot d\mathbf{l}_2, \tag{5.13}$$

where the integration is depicted along the contour shown in the inset of Fig. 5.2. So we see that physically, the so-called magnetic current corresponds to the potential difference on either side of the C-SRR "wire" due the presence of induced charges. From Faraday's law, we have

$$\hat{\mathbf{n}} \cdot (\nabla \times \mathbf{E}) = \nabla \cdot (-\hat{\mathbf{n}} \times \mathbf{E}) = -j\omega (\hat{\mathbf{n}} \cdot \mathbf{B}), \tag{5.14}$$

or

$$\nabla \cdot \mathbf{J}_m = -j\omega \rho_m, \tag{5.15}$$

and we have recovered a continuity equation for our fictitious current. If we assume that the physical currents are contained in the "complementary gap" of the C-SRR, then the irrotational magnetic fields will also be localized there. From this continuity equation, we therefore see that I_m will be constant elsewhere in the circuit, and our definition of electrical inductance is consistent with the conventional case.

This leads us to our final term, which unsurprisingly corresponds to a magnetic capacitance:

$$\int \nabla \phi_m \cdot d\mathbf{l} = \frac{Q_m}{C_m}, \tag{5.16}$$

where the so-called "magnetic charge" Q_m only appears due to our incomplete integration around the SRR. Our circuit model will allow us to immediately calculate the dipole moments using Eq. 5.6.

Our formulation is limited in that it does not directly relate to real physical quantities, but it allows us to use our well-developed intuition regarding conventional

circuits in the analysis of complementary structures. The physical currents in the C-SRR are distributed over the entire PEC surface and do not follow a simple or intuitive path. By comparison, the fictitious magnetic currents follow the same well-defined path as electrical currents in true wire circuits.

This formulation also has the benefit that it exists independently of a well-defined transmission line. For instance, when used as couplers, apertures are often modeled as series or shunt inductive loads. However, the loading effect of a finite aperture in an infinite parallel plate waveguide is somewhat ill-defined since only the impedance per-unit-length is defined for such as structure.

We will not develop this circuit concept further, but we note that it could be useful for design and analysis in conjunction with the modified DDA methods that we introduce later in this chapter.

5.2.3 Energy Balance and the Modified Sipe-Kranendonk Condition

Our quasistatic model does not consider the effect of radiation damping. This effect typically manifest as a loss term in circuit descriptions of antennas. Similarly, in scattering calculations, a losseless element will have a nonvanishing imaginary part to its polarizability determined by the relationship:

$$\mathrm{Im}\left[\frac{1}{\alpha}\right] = \frac{k^3}{6\pi\varepsilon}, \tag{5.17}$$

which is sometimes referred to as the Sipe-Kranendonk condition [128]. This condition must be satisfied for a self-consistent description of a passive scatterer due to power balance considerations. We will demonstrate that this condition must be modified when considering small apertures as polarizable elements. This modified condition will be integral to our understanding of the behavior of these apertures, and it will also be necessary to any implementation of discrete-dipole analysis. Consider the problem of an electromagnetic wave impinging on a PEC surface, creating two

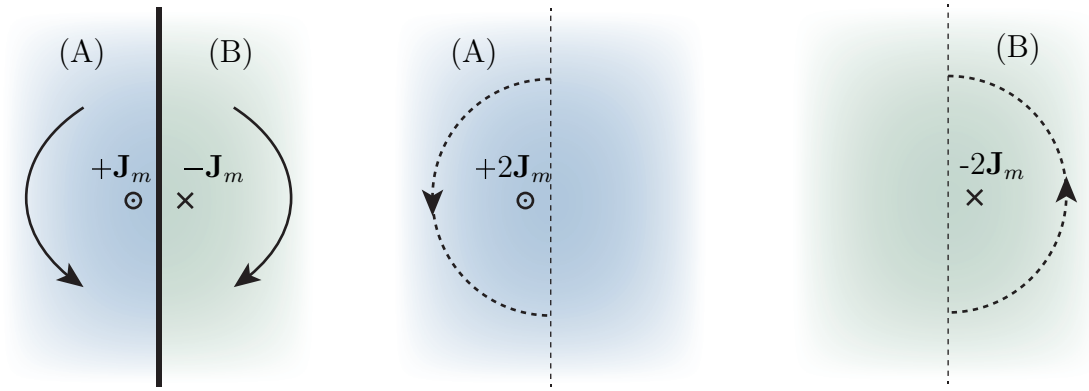

(a) Sources in (A) and (B) (b) Intregation for (A) (c) Intregation for (B)

FIGURE 5.3: Integration of power radiated by equivalent magnetic sources

.

dielectric half-spaces, (A) and (B). An aperture exists in the PEC such that it is described by a magnetic polarizability $\bar{\bar{\boldsymbol{\alpha}}} = \alpha\hat{\mathbf{z}}\hat{\mathbf{z}}$. The incident field is on side (A). The problem reduces to the scalar form, and we will forgo the dyadic subscripts for the sake of compactness. The induced magnetic dipole m is produced on either side of the PEC surface as shown in Fig. 5.3(a). The power expended by the plane wave on the induced current is given by[1]:

$$P^{ext} = \frac{1}{2}\mathbf{J}_m^* \cdot \mathbf{H}_0. \tag{5.18}$$

We see the power expended to excite the dipole is given by:

$$\begin{aligned} P^{ext} &= \frac{1}{2}Re\left[J_m^* H_0\right] = \frac{1}{2}Re\left[-j\omega m^* H_0\right] \\ &= \frac{1}{2}Re\left[-j\omega\alpha^*\right]|H_0|^2 = -\frac{\omega}{2}Im\left[\alpha\right]|H_0|^2. \end{aligned} \tag{5.19}$$

We now need to determine the power radiated by a complementary metamaterial. The scattered fields are those of a point magnetic current source $M = +j\omega m$ on top of a PEC ground plane on side (A). Using image theory, this is equivalent to a point

[1] We note that Eq. B.1 may not be obvious at first glance. We therefore include a short derivation in Appendix B.

current of twice the amplitude radiating in free-space. We can then integrate the Poynting vector in the far-field using the free-space magnetic Green's function:

$$P^{rad,A} = \int_0^{\pi}\int_0^{\pi} \frac{1}{2} Re\left[E_\phi H_\theta^*\right] \rho^2 \sin\theta d\phi d\theta = \frac{\omega^2 k^2}{6\pi\eta}|m|^2 = \frac{\omega^2 k^2}{6\pi\eta}|\alpha|^2|H_0|^2 \tag{5.20}$$

where the integration is only over the top half-space, as shown in Fig. 5.3(b). However, the dipole will also radiate into the bottom half-space (B), as shown in Fig. 5.3(c). The total radiated power is therefore

$$P^{rad} = \frac{\omega}{6\pi\mu_0}\left(k_A^3 + k_B^3\right)|\alpha|^2|H_0|^2. \tag{5.21}$$

In the lossless case, $P^{ext} = P^{rad}$ and

$$Im\left[\alpha\right] = -\frac{k_A^3 + k_B^3}{3\pi\mu_0}, \tag{5.22}$$

or

$$Im\left[\frac{1}{\alpha^{mm}}\right] = \frac{k_A^3 + k_B^3}{3\pi\mu_0}. \tag{5.23}$$

A similar analysis leads to a similar condition on the electrical polarizability:

$$\mathrm{Im}\left[\frac{1}{\alpha^{ee}}\right] = \frac{k_A^3 + k_B^3}{3\pi\varepsilon}. \tag{5.24}$$

Since the DDA operates on the inverse polarizability, we need only add this quantity to the nominal value to obey conservation of energy, (half this value with the re-normalized polarizability that we introduce in the next section). If the polarizability is retrieved via simulation, this condition should be satisfied automatically. However, if the electrical size of the element is considerable, the point-dipole description might fail, and the radiation condition might not be satisfied. Additionally, elements such as the SRR have considerable quadrupole moments that are not considered in retrieval

[27, 28], and this condition will not be met in our retrieved polarizability [114]. We can at least enforce self-consistency in our model by making the substitution:

$$\frac{1}{\alpha^{e(m)}} = Re\left[\frac{1}{\alpha_{sim}}\right] + j\frac{k^3 + k_0^3}{3\pi\varepsilon(\mu)}. \tag{5.25}$$

The DDA model is very sensitive to this parameter, especially near resonance. However, enforcing this condition can yield surprisingly good accuracy for structures with dimensions upwards of $\lambda/5$.

5.3 DDA Simulation

Since complementary elements may be described by electric and magnetic polarizabilities, they should be amenable to DDA simulations. Indeed, we shall find that we can use the 2D formulation from Section 4.1 with only minor modifications. We will then demonstrate the power of this method by comparing our DDA results to those of full-wave simulations. Finally, we will attempt to design a CMM cloak with our knowledge of the modified interactions in these apertures.

5.3.1 Interactions in a CMM-loaded Waveguide

We will constrain our analysis to the scalar problem by considering elements with only an appreciable magnetic response along y. The axes are as depicted in Fig. 5.4. We begin by considering a PEC plane separating two dielectric half-spaces (A) and (B), with corresponding dielectrics constants ϵ_r^A and ϵ_r^B, as shown in Fig. 5.4(a). We etch an aperture in this plane, so that the cross-section is as shown. A TM^z wave is incident on this aperture from side (A). In (A), the incident magnetic fields induce magnetic dipoles as expected from our circuit model. The scattered fields are therefore those of a Hertzian point source m radiating in the presence of a conducting sheet. By image theory [26], these fields will be identical to fields radiated by point

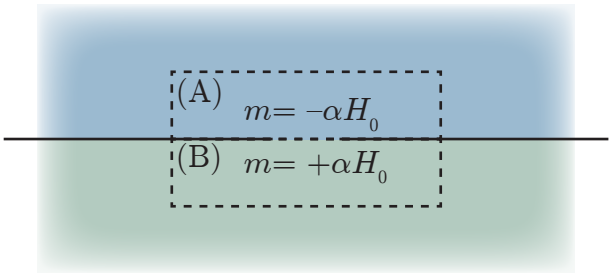

(a) The Physical Problem

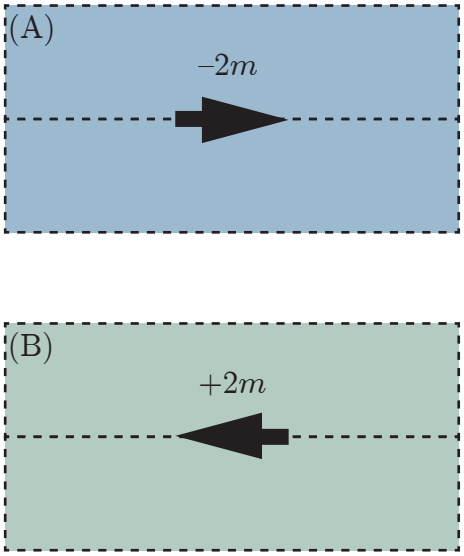

(b) Equivalent Problem in (A) and (B)

FIGURE 5.4: Application of the surface equivalence principle and image theory to CMMs.

sources $2m$ in a homogeneous medium, as shown in Fig. 5.4(b). We can therefore use the Green's function of a homogenous medium to calculate the scattered fields as long as we double the effective magnetic dipole moments generating the fields. On side (B), the magnetic dipole will be equal in magnitude, but opposite in sign, of that on side (A). The scattered fields on side (B) will therefore be the same as those from a dipole $-2m$. We can absorb the factor of 2 that comes from the image dipole if we simultaneously double our effective polarizability $\tilde{\alpha}$, and effective dipole moment $\tilde{m}$. This will be useful since all fields will be calculated using the effective dipole moment.

We now add another PEC plane in (A) to form a parallel plate waveguide of height h as shown in Fig. 5.5(a). The Green's function on side (B) will be unchanged, but

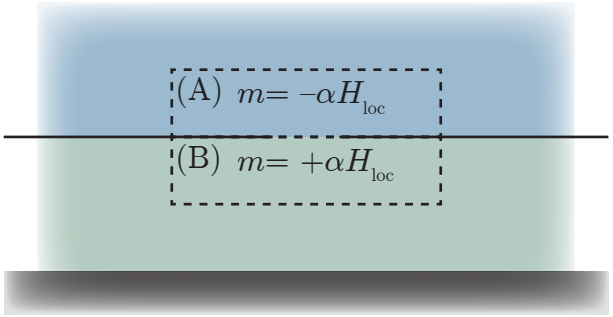

(a) The Physical Problem

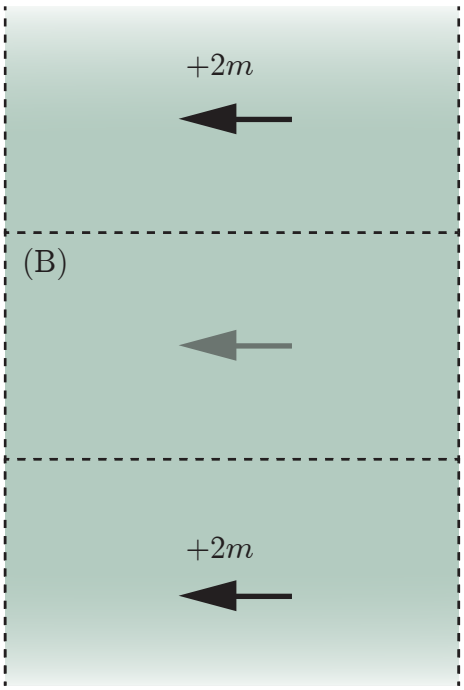

(b) Contribution from Image Dipoles

FIGURE 5.5: The scattering problem for an isolated aperture. (Left) The original scattering problem. (Right) The equivalent-source problem for the scattered fields

.

that off side (A) will be modified by the new boundary condition. Using image theory once again, we see that the presence of the two plates is equivalent to the presence of infinite columns of identical dipoles. We have therefore recreated the 2D system that we discussed in Section 4.1, and we may use the Green's functions that we developed in that section to describe the interactions of dipoles on side (A). Additionally, the image dipoles will contribute to the local field exciting the aperture, so we will once again include those interactions as part of an effective polarizability, $\tilde{\alpha}$.

We now pattern additional apertures of polarizabilities $\tilde{\alpha}_i$. Each aperture i will be excited by the incident field as well as those generated by the columns of dipoles j on side (A). However, the dipoles on side (B) will also contribute to the local field.

These fields act against the fields in (A), but they are also generated by dipoles of the opposite sign, so the overall contribution is once again positive. We have depicted these interaction mechanisms graphically on the right of Fig. 5.5. The local field acting on an element i is therefore:

$$\tilde{\alpha}_i^{-1}\tilde{m}_i = H_0\left(\mathbf{r}_i\right) + \sum_{j\neq i}\tilde{m}\left[\tilde{G}^A\left(\boldsymbol{\rho}_{ij}\right) + G^B\left(\boldsymbol{\rho}_{ij}\right)\right], \tag{5.26}$$

where $\tilde{G}$ represenents the Green's function corresponding to a column of dipoles, and $k^{A,B} = \sqrt{\epsilon_r^{A,B}}k_0$ is the dielectric-loaded wave-number.

Once we have computed the dipole moments, the scattered field is found by summing up the contribution from the all the columns:

$$H_s^A(\boldsymbol{\rho}) = \sum_i \tilde{m}_i \tilde{G}_r^A\left(\boldsymbol{\rho} - \boldsymbol{\rho}_i\right), \tag{5.27}$$

and the radiated field will be given by:

$$H_s^B(\mathbf{r}) = -\sum_i \tilde{m}_i G^B\left(\mathbf{r} - \mathbf{r}_i\right). \tag{5.28}$$

Now that we have deduced how these dipoles interact, we can modify the 2D interaction constants from Section A.1 to retrieve the polarizability of a simulated structure, as shown in Fig. 5.6(b). The mirroring effect of the PEC and PMC boundary conditions on side (A) create an infinite 2D array of polarizability elements that contribute to the local field exciting the element. From Section 4.2, we know that these contributions are encapsulated in the interaction constant C. However, we now must add the contributions from side (B):

$$C_m^{(B)} = C_m^{(1)} = \sum_{m=1}^{\infty} \frac{e^{-jk^{(B)}ma_y}}{4\pi\mu_0}\left(\frac{jk^{(B)}}{a_y^2m^2} + \frac{1}{a_y^3m^3}\right). \tag{5.29}$$

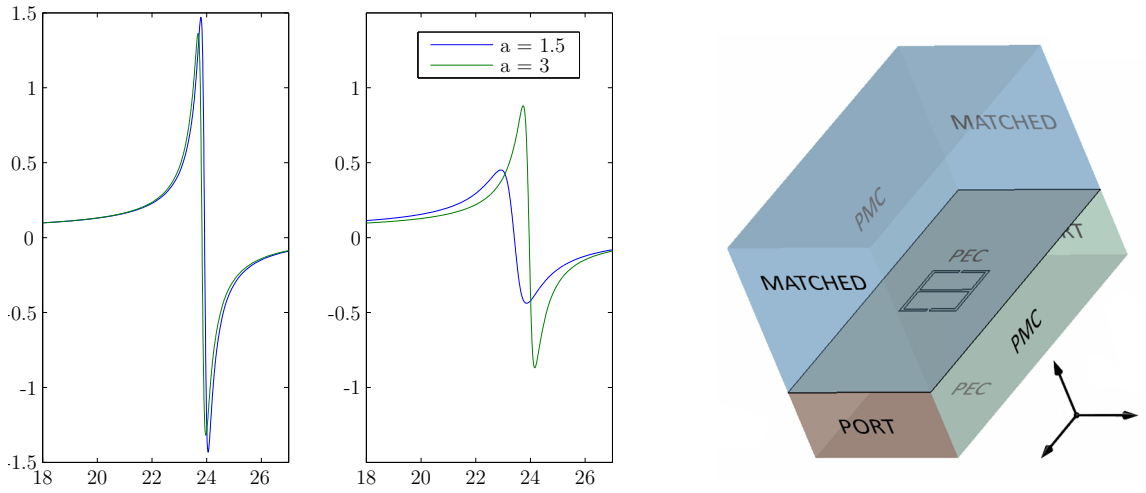

(a) Retrieved Magnetic Polarizability (b) Simulation Domain

FIGURE 5.6: Polarizability Retrieval of CMMs

.

We then simply add this interaction constant to that of a conventional array. As before, we verify the accuracy of the retrieval by performing it on the same aperture for two different lattice spacings as shown in Fig.5.6(a). As before, the retrieved element polarizability is essentially unchanged for both lattice constants (the resonance frequency changes by less than 100 MHz. On the other hand, $\tilde{\alpha}$ is clearly affected by the interactions of the other dipoles in the array; the resonance frequency has blue-shifted by 820 MHz as the the spacing is increased. We also observe significant variation in the overall amplitude of $\tilde{\alpha}$: The maximum value increases by 192%.

We are finally in a position to simulate a physical device. As a test, we simulate a device of modest electrical size so that we can compare to full wave simulations. This device consists of a 3×3 array of C-ELCs as shown in Fig. 5.7. We confine the simulation domain with a rectangular fence of metallic vias, and we excite the structure with two probes using the model that we developed in the previous section. In order to increase the accuracy of the simulations, we have included the effect of

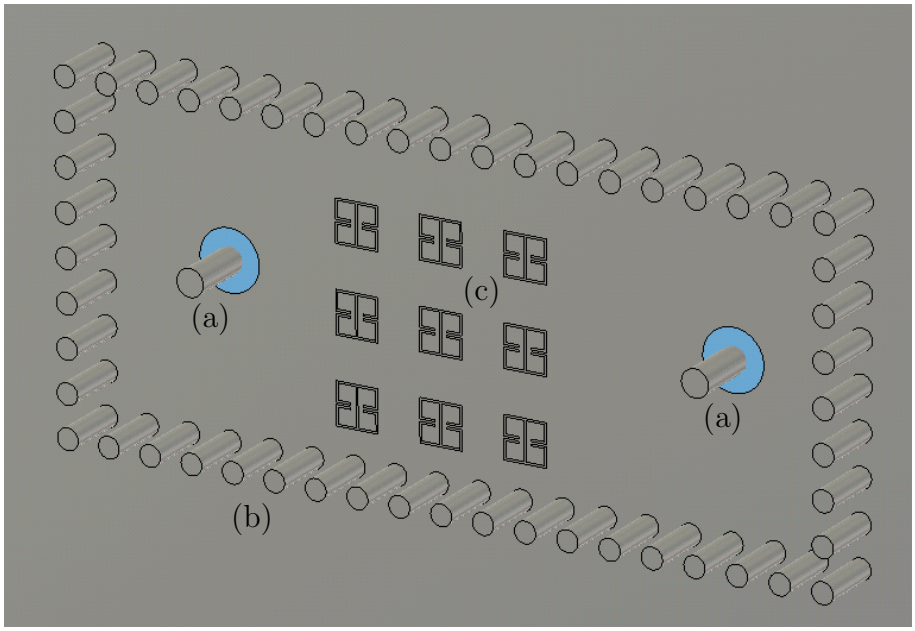

FIGURE 5.7: Diagram of CMM-DDA Test Device. (a) Coax Probe; (b) PEC Via; (c) C-ELC.

the magnetic polarizability of the vias:

$$\alpha_{xx}^{mm} = \alpha_{yy}^{mm} - 2\mu_0 a^2, \tag{5.30}$$

as well as the electrical polarizabilities of the C-ELCs.

In Fig. 5.8 we compare the two-port S-parameters to those calculated in CST Microwave Studio. Details for the calculation of network parameters in the DDA may be found in the Appendix C, along with a model for the coaxial probe. The agreement is quite good across the entire simulated frequency range, though some error in our model is apparent past the resonance at 24 GHz. We quantify this agreement by comparing the null in S_{11} between simulations. The lowest frequency null in S_{11} at 20.9 GHz is in perfect agreement to the descretization level of our simulations (100 MHz). The second null shows similar agreement. However, there is a discrepancy of 200 MHz between simulations at the high-frequency null. This error appears because we are approaching the magnetic quadrupoles' resonance in

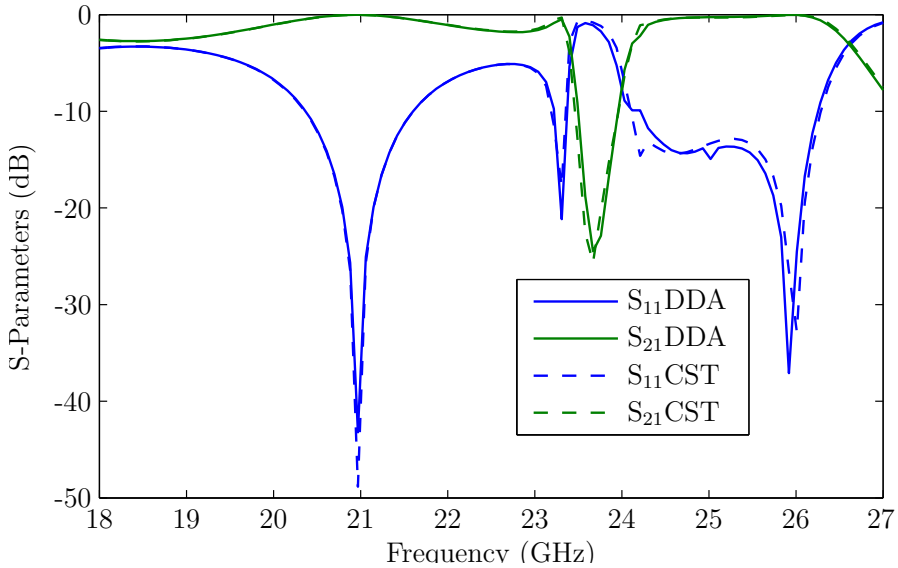

FIGURE 5.8: Comparison of DDA Code to Full-Wave Simulation

our structure, and we have neglected it in our model. The agreement improves at lower frequencies since the behavior of the system is dominated by both the probe and the vias characteristics, which are well-described by our model.

5.3.2 TO Design with CMMs

In the previous Subsection, we showed that the DDA simulations of CMMs compare favorably with full-wave numerical solvers. We have also shown that a CMMs may be regarded as effective material fillings in a parallel plate waveguide. Therefore, we might reasonably expect that we could fashion TO devices by patterning CMMs on one- or both-sides of a parallel plate waveguide. Indeed, this has already been demonstrated in [18]. We will reach similar conclusions with some qualifications.

In the previous section, we noted that the DDA and retrieval process had to be modified to account for coupling between CMMs both inside and outside the parallel-plate waveguide. This modification took the form of additional terms in our interaction constants. Additionally, we noted in Subsection 5.2.3 that the imaginary part of the polarizability differed from the conventional case. Both of these differ-

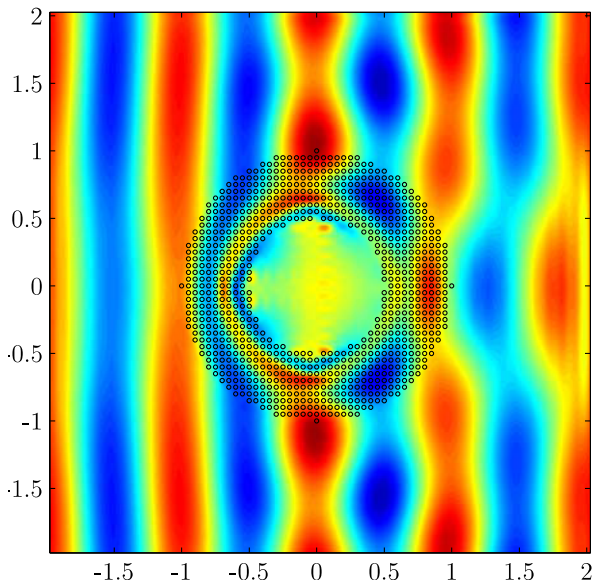

FIGURE 5.9: Cloak designed with CMMs and $C = \mathbf{I}\frac{1}{3}$

.

ences must be considered when designing a TO device. We can immediately see the effect of this complication if we ignore it and attempt to design a cloak using the conventional Clausius-Mosotti relationship. We plot a DDA simulation of such a cloak in Fig. 5.3.2. Clear phase errors appear in the forward direction. This does not appear to be caused by nonlocal interactions between elements: we have used a small lattice parameter $a = 0.05$, and we have reduced the overall size of the cloak relative to the one in Section 4.4. Instead, the error is due to our use of Clausius-Mossotti with an interaction constant $C = \mathbf{I}\frac{1}{3}$, which does not accurately account for all the interactions between the elements. We must therefore develop a modified version to design a cloak.

To simplify our analysis, we will restrict ourselves to quasi-static interactions between elements in a cubic lattice. For a conventional lattice, the interaction constant has the approximate form [116]:

$$C_{xx}^{(A)} = C_{yy}^{(A)} = C_{zz}^{(A)} \approx \frac{.3365}{a^3}. \tag{5.31}$$

This would be the correct interaction constant for our system if we only included the interactions of dipoles in the waveguide. On the other side of the parallel plate, we have to include the interaction effects of a infinite 2D lattice with its surface normal directed in $\mathbf{z}$. For the $x-$ or $y-$ directed magnetic dipoles, this interaction constant takes the form [116]:

$$C_{xx}^{(B)} = C_{yy}^{(B)} \approx \frac{0.3589}{a^3}. \tag{5.32}$$

Therefore, the total interaction constant is, (e.g. for C_{yy}):

$$C_{yy} = C_{yy}^{(A)} + C_{yy}^{(B)} \approx \frac{0.6954}{a^3}. \tag{5.33}$$

We see that the contributions from (B) have increased the interaction constant: the additional dipole fields add constructively to the local field exciting the element. On the other hand, for the z-directed electric dipoles,

$$C_{zz}^{(B)} \approx -\frac{0.7179}{a^3}. \tag{5.34}$$

This reflects the depolarizing effects of a plane of dipoles oriented in the same direction as the surface normal of that plane.

We can now enter the modified interaction constants in the Clausius-Mossotti equation to determine the necessary polarizabilities. We plot the DDA simulation results in Fig. 5.10(a) for the same lattice parameter $a = 0.025$. The results are not particularly encouraging. We may have slightly reduced the phase error, but now there is a strong forward shadow due to an apparent attenuation of the transmitted fields.

We can explain this result qualitatively. Our improved interaction constant provides us with a better impedance-match to free space, and back-scattering is somewhat reduced. However, the CMMs scatter into free-space modes on side (B) that

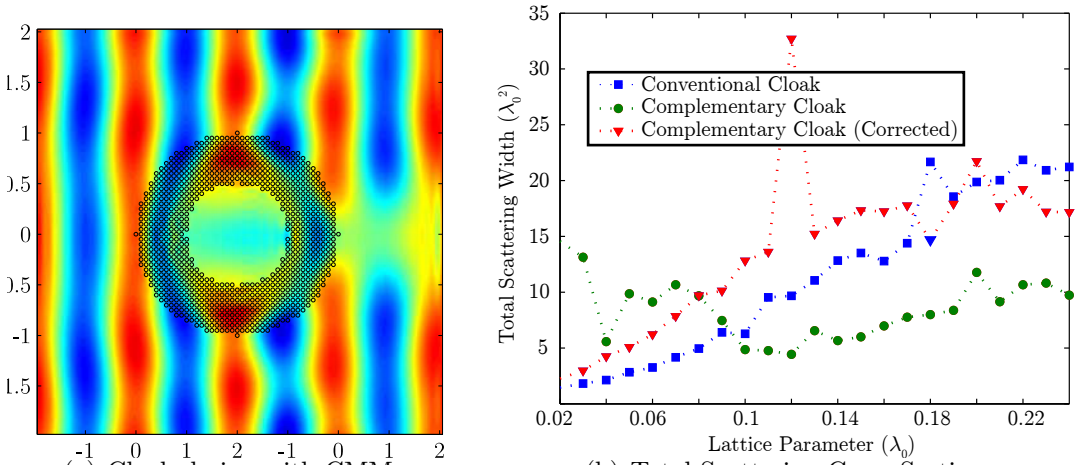

(a) Cloak design with CMMs (b) Total Scattering Cross-Section

FIGURE 5.10: Comparison of CMM cloaks

manifest as an effective loss term in the guided waves. This is reflected in the modified Sipe-Kranendonk condition: the imaginary part of the 3D interaction constant no longer balances the imaginary constant as it would in a conventional array [87], and the guided wave amplitude is attenuated. This should come as no surprise since $q < k_0$ in the device, and we have created an odd leaky-wave antenna[129].

Despite this complication, the total SCS *does* decrease as the lattice parameter is decreased, as shown in Fig. 5.10(b), though the convergence towards zero SCS is a bit slower than for the conventional case, (also shown). Nevertheless, it is a clear improvement over our initial design. We therefore conclude that a complementary cloak is feasible theoretically, though the required unit cell size might not be compatible with current lithographic techniques. However, it may be possible to mitigate the radiative loss by other means[130], though this would require more modifications to the DDA method.

5.4 Conclusions

In this chapter, we have examined complementary metamaterials. At the element level, we have related them to conventional metamaterial circuit elements by developing a circuit model based on fictitious magnetic currents. We have shown that the peculiarities of CMMs requires us to modify the DDA retrieval and simulation methods that we developed in Chapter 4. Finally, we have shown the TO design is possible with CMMs, though it may not be possible to design a high-performance device at this time. My specific contributions included:

- I have shown that the strict duality between conventional and complementary MMs is limited. I have therefore introduced an alternative description based on quasistatic magnetic currents.
  - This technique could be generalized in future work. This would include applying it to the design of magnetically-coupled apertures.
- I have demonstrated the accuracy of a polarizability retrieval algorithm for C-MMs.
  - Future work would improve the accuracy of this method by accounting for non-dipolar interactions between C-MM elements. This could be accomplished by incorporating higher-order multipole interactions or by modifying the circuit approach of Section 4.5.
- I extended the DDA method to simulate structures containing C-MMs. I verified the accuracy of this technique by simulating a small C-ELC array with the DDA and comparing it to full-wave simulation.
  - Future work would generalize this technique in a similar manner as for my polarizability retrieval algorithm, i.e., it would include interactions

beyond the dipole-dipole coupling term to increase the accuracy of the simulations for distributed structures in dense arrays.

- I used my modified DDA algorithm to analyze TO devices implemented with C-MMs. Additionally, I showed the interaction constant in the Clausius-Mossotti relationship must be modified in C-MM arrays. However, even with this correction, I demonstrated that the tendency of C-MMs to scatter into free-space modes limits their utility.
  - My modified interaction constant was determined for a quasistatic array of C-MMs. This method could be generalized in future work in a manner that would parallel my work in Section 4.4.
  - In [130], we showed that radiative loss can be mitigated in some C-MM unit cell designs. Future work could incorporate these modifications into DDA analysis and the design of C-MM structures.

6

Conclusions

The TO design process is simple, intuitive, and elegant; coordinate transformations provide the required material parameters to create a device. This simplicity comes at the cost of correspondingly high complexity in the resulting metamaterial development process. In the preceding chapters, I have presented several methods to address this complexity. I capitalized on freedoms in both the metamaterial design and in the transformations themselves. I now briefly reiterate my contributions and possible directions for future work on the subject:

In Chapter 2, I explored freedoms in the mappings themselves, using high frequency approximations to minimize the complexity of necessary responses in my device. I investigated the impact of these approximations and concluded that a high-performance lens could be fashioned from a material using only one magnetic response, as opposed to the three required by most TO designs:

- I extended practical TO design to 3D by applying the quasiconformal mapping method to azimuthally-symmetric systems. Using the eikonal approximation, I simplified 3D-TO design by reducing the nonvanishing material responses from six to three. Only one of these remaining responses is magnetic, which further

reduces the complexity of design.

- I built on the designs presented by Schurig [53] and Kundtz [59] by flattening the focal surface of a Luneburg lens using the aforementioned QC method in 3D. Using both ray-tracing and full-wave numerical analysis techniques, I have shown that the reduced-parameter lens provides diffraction limited-performance out to 30° for apertures over twenty-five wavelengths in diameter. Future work on this design would consist of experimental verification and generalization to higher frequencies. The specific steps would include:
  - To design a metamaterial unit cell to provide the range of magnetic and dielectric responses required by the reduced-parameter lens design.
  - Verification of unit cell performance by incorporating the retrieved polarizability in a discrete-dipole simulation (Chapter 4) of the full 3D lens.
  - Fabrication and characterization of the reduced-parameter lens at microwave or higher frequencies.
  - Generalization of the design to higher frequencies. At infrared frequencies and above, metallic losses may preclude the used of artificial magnetism [68, 69], and alternative methods may be needed to generate the necessary anisotropy in the lens.

In Chapter 3, I exploited the electromagnetic environment of my apparatus to provide me with one of three necessary parameters to create an impedance-matched cloak:

- I have created a metamaterial unit cell with two distinct magnetic responses that I implemented in a full-parameter unidirectional cloak.
  - Measured data revealed that the optimal cloaking frequency had shifted from the designed frequency of 10 GHz to 10.2 GHz. I attributed this

shift to intra-unit cell coupling that was not considered in the design of the unit cell. In Chapter 4 I show that phase error can occur when spatial dispersion is neglected. Future work might incorporate corrections to compensate for this error in a manner similar to the one that I demonstrate in Section 4.4.

  - Future work on this design could also involve an extension to 3D. As previously stated, my current design is limited to 2D operation. Additionally, the corrugations prohibit further generalization. Therefore, a 3D implementation would require another method to generate the necessary paramagnetic responses.

- I designed, fabricated, and experimentally characterized the aforementioned cloak, and showed approximately 50% reduced scattering from the cloaked object.

  - My cloak required a parallel-plate waveguide to function. However, I asserted that the cloak could be implemented in free space by stacking identical copies of the cloak and taper combination in the the out-of-plane direction, (i.e. the direction of the incident wave polarization.), this cloak could then be measured in a conventional anechoic chamber or compact range.

I have also developed several tools that allow me to probe the effects of various material designs independently of a specific metamaterial implementation. In Chapter 4, I showed that errors can manifest in TO structures even in the conventional effective medium regime. However, I were able to use these same tools to obtain a correction to the assigned parameters, and restore a great deal of performance to a given TO-design:

- I have improved upon the 2D-DDA method introduced by Bowen et. al.[86] by incorporating acceleration techniques for Green's functions and self-interaction terms.
  - Future work would to extend the magneto-electric DDA to optically-large, 3D structures. This is a challenging problem since it involves the solution of a dense system of linear equations. Iterative methods may be used for larger domains [120], but to our knowledge, these methods have not been applied to the analysis of TO structures.
- I derived an expression for the Bloch modes in a lattice of magneto-electric point dipoles. I used this dispersion relation to calculate corrections to the assigned polarizabilities in a metamaterial cloak. For optically large cloaks, ($R_1 \geqslant 1$), this correction allows for over a 50% reduction in total scattering cross-section.
  - Future work would include designing a specific metamaterial unit cell and phyisical implementation of the corrected design. Since the corrections are small for a $\lambda_0/10$ spacing, I would attempt to use even larger unit cells so that the correction is larger, and therefore hopefully less sensitive to realistic design tolerances.
- I have shown that the DDA can be generalized to include knowledge of the quasistatic interactions between canonical geometries. I demonstrated the accuracy of this technique by retrieving the correct polarizability from a dense array of split-ring resonators.
  - Future work would extend this method to capacitively-coupled resonators.
  - Future work would also use this method for the design and analysis of a physical TO optic.

Similarly, in Chapter 5, I developed methods to analyze the behavior of complementary structures, and their applicability in TO design. I highlighted some of the subtleties of working with these apertures, and I offered a method to modify my designs to accommodate their odd behavior:

- I have shown that the strict duality between conventional and complementary MMs is limited. I have therefore introduced an alternative description based on quasistatic magnetic currents.
  - This technique could be generalized in future work. This would include applying it to the design of magnetically-coupled apertures.
- I have demonstrated the accuracy of a polarizability retrieval algorithm for C-MMs.
  - Future work would improve the accuracy of this method by accounting for non-dipolar interactions between C-MM elements. This could be accomplished by incorporating higher-order multipole interactions or by modifying the circuit approach of Section 4.5.
- I extended the DDA method to simulate structures containing C-MMs. I verified the accuracy of this technique by simulating a small C-ELC array with the DDA and comparing it to full-wave simulation.
  - Future work would generalize this technique in a similar manner as for my polarizability retrieval algorithm, i.e., it would include interactions beyond the dipole-dipole coupling term to increase the accuracy of the simulations for distributed structures in dense arrays.
- I used my modified DDA algorithm to analyze TO devices implemented with C-MMs. Additionally, I showed the interaction constant in the Clausius-Mossotti

relationship must be modified in C-MM arrays. However, even with this correction, I demonstrated that the tendency of C-MMs to scatter into free-space modes limits their utility.

- My modified interaction constant was determined for a quasistatic array of C-MMs. This method could be generalized in future work in a manner that would parallel my work in Section 4.4.
- In [130], we showed that radiative loss can be mitigated in some C-MM unit cell designs. Future work could incorporate these modifications into DDA analysis and the design of C-MM structures.

Many of these complexities have forced me to abandon a purely material description. The nonlocal interactions between elements in Chapter 4 caused me to concentrate on the Bloch waves in the structure instead of attempting to create a local description of my system. In Chapter 5, I had to consider the effects of scattering loss, a phenomenon absent in a typical homogeneous medium. Finally, my cloaking "material" in Chapter 3 only had meaning for the fundamental guided mode in a a parallel-plate waveguide. Not only would my cloak be ineffective for other modes at the same frequency, but I could not even describe the system with the same effective medium properties.

I therefore conclude that metamaterials may be fruitfully applied to transformation optical design. However, my goal is neither to design a TO device, nor is it to create a metamaterial that is only described by local material properties. My goal is to design devices that meet the required metrics in performance. Therefore, both TO and MM are most useful as a point of departure for more complex analysis and design.

Appendix A

Evaluation of Dynamic Interactions Constants in a Magneto-Dielectric Lattice

A.1 Evaluation of 2D Interaction Constants

We begin by considering an infinite 2D of identical elements with an assigned magnetic polarizability α_m and electric polarizability α_e immersed in a dielectric ε. An incident electromagnetic wave $E_0\mathbf{z}\exp(-jkx)$ will excite magnetic dipoles m_y and electric dipoles p_z. From the symmetry of the problem, the magnetic and electric responses are decoupled and they may be treated separately. We will first consider the magnetic response.

The local field exciting an element located at the origin of our coordinate system may be written:

$$H_y^{loc}(0) = \mu_0^{-1} C_{yy} = \mu_0^{-1} \left(k^2 + \frac{\partial^2}{\partial y^2}\right) G(\mathbf{r}_{mn})\Big|_{y=0}, \tag{A.1}$$

where G is the scalar Green's function:

$$G = \frac{1}{4\pi}\frac{e^{-jkr}}{r}. \tag{A.2}$$

Equation A.1 is a doubly infinite sum consisting of the contribution from all the dipoles excluding the one under consideration. We break the sum into two parts $C_{yy}^{(2D)} = C_{yy}^{(1)} + C_{yy}^{(2)}$, and similarly for G_y. $G_y^{(1)}$ consists of the contribution from the elements in the column ($z = 0$), and $G_y^{(2)}$ consists of the contributions from all of the other columns. The explicit expression for $C_{yy}^{(1)}$ is

$$C_{yy}^{(1)} = \sum_{m=1}^{\infty} \frac{e^{-jkma_y}}{4\pi} \left(\frac{jk}{a_y^2 m^2} + \frac{1}{a_y^3 m^3} \right). \tag{A.3}$$

These geometric series have known analytical solutions [116]. The calculation for $C_{yy}^{(2)}$ is substantially more involved. Our initial expression for $G_y^{(2)}$ is:

$$G_y^{(2)} = \frac{1}{4\pi} \sum_{n=-\infty}^{\infty}{}' \sum_{m=-\infty}^{\infty} \frac{\exp\left\{-jk_0 \left[n^2 a_z^2 + (y - ma_y)^2\right]^{1/2}\right\}}{\left[n^2 a_z^2 + (y - ma_y)^2\right]^{1/2}}, \tag{A.4}$$

where ($'$) indicates that we are omitting the dipole at the origin. Using the Poisson summation technique, we calculate the contributions from all remote columns:

$$G_y^{(2)} = \frac{1}{2\pi a_y} \sum_{n=-\infty}^{\infty}{}' \sum_{m=-\infty}^{\infty} e^{j2\pi my/a_y} K_0 \left(c_m \left|na_z\right|\right) \tag{A.5}$$

where $c_m = \left[(2m\pi/a_y)^2 - k_0^2\right]$. When $m = 0$ the summation over n will have poor convergence since the MacDonald Function with imaginary arguments decays asypmtotically as $\rho^{-1/2}$. We therefore separate it from the others:

$$G_y^{(2)} = \frac{1}{2\pi a_y} \sum_{n=-\infty}^{\infty}{}' K_0 \left(jk_0 na_z\right) + \frac{2}{\pi a_y} \sum_{m=1}^{\infty} \sum_{n=1} e^{j2\pi my/a_y} K_0 \left(c_m na_z\right). \tag{A.6}$$

We can improve the convergence of the first term in A.6 by using the method of dominant series. We do this by allowing x to vary and then taking the limit as $x \to 0$. We first use the Poisson Summation technique again:

$$\frac{1}{2\pi a_y} \sum_{n=-\infty}^{\infty}{}' K_0 \left[jk_0 \left(x^2 + n^2 a_z^2\right)\right] = \frac{1}{2a_y a_z} \sum_{n}^{\infty} \frac{e^{-c_n x}}{c_n} - \frac{1}{2\pi a_y} K_0 \left(jk_0 x\right), \tag{A.7}$$

where $c_n = \left[(2n\pi/a_z)^2 - k_0^2\right]$. We note that for large n/a_z, $cn \approx 2n\pi/a_z$. We are therefore motivated to break up the first term in Eq. A.7 to reflect this fact:

$$\frac{1}{2a_y a_z}\sum_n \frac{e^{-c_n x}}{c_n} = \frac{e^{jk_0 x}}{j2k_0 a_y a_z} + \sum_{n=1} \frac{e^{-2\pi n x/a_z}}{2\pi n a_y} + \sum_{n=1}^{\infty}\left[\frac{e^{-c_n x}}{a_y a_z c_n} - \frac{e^{-2\pi n x/a_z}}{2\pi m a_y}\right]. \tag{A.8}$$

The second summation will converge rapidly as it represents the difference between the true series and its approximate representation. The approximate series is geometric and may be summed explicitly:

$$\sum_{n=1}^{\infty} \frac{e^{-2\pi n x/a_z}}{2\pi m a_y} = -\frac{\log\left(1 - e^{-2\pi x/a_z}\right)}{2\pi\mu_0 a_y}. \tag{A.9}$$

It may be shown that the logarithmic singularity in Eq. A.9 will cancel the singularity in the MacDonald function in Eq. A.7 in the limit $x \to 0$. The final expression for $G_y^{(1)}$ is therefore:

$$\begin{aligned} G_y^{(2)} = {} & \frac{\gamma + \log\left(jk_0 a_z/4\pi\right)}{4\pi a_y} - \frac{j}{4k_0 a_y a_z} \\ & + \sum_{n=1}^{\infty}\left[\frac{1}{2a_y a_z c_n} - \frac{1}{4\pi n a_y}\right] \\ & + \frac{1}{\pi a_y}\sum_{m=1}^{\infty}\sum_{n=1}^{\infty} e^{j2\pi m y/a_y} K_0\left(c_m n a_z\right). \end{aligned} \tag{A.10}$$

Inserting Eq. A.10 into Eq. A.2, we find that

$$\begin{aligned} C_{yy}^{(2)} = \frac{k_0^2}{2a_y}\Bigg[& \frac{\gamma + \log\left(jk_0 a_z/4\pi\right)}{2\pi} - \frac{j}{2k_0 a_z} + \sum_{n=1}^{\infty}\left(\frac{1}{a_z c_n} - \frac{1}{2\pi n}\right)\Bigg] \\ & + \frac{1}{\pi a_y}\sum_{m=1}^{\infty}\sum_{n=1}^{\infty}\left[k_0^2 - \left(\frac{2\pi m}{a_y}\right)^2\right] K_0\left(c_m n a_z\right). \end{aligned} \tag{A.11}$$

We note that the remaining series in Eq. A.10 may be neglected for moderate or large dipole spacings.

The calculations for the other component of the interaction tensor C_{zz} will have an identical form upon the substitution $(ay, az) \rightarrow (az, ay)$.

In 4.5.1, we develop a modified version of the DDA that uses the analytical form of the mutual inductance between coaxial loops. We incorporate this modification into our interaction constant by adding the analytic term (Eq. 4.29) as a correction series to Eq. A.3:

$$\tilde{C}_{yy}^{(2)} = \sum_{m=1}^{\infty} \frac{e^{-jk_0 m a_y}}{\pi} \left(\frac{jk_0}{a_y^2 m^2} + \frac{1}{a_y^3 m^3} \right) + \sum_{m=1}^{\infty} e^{-jk_0 m a_y} \left[\frac{2M^{QS}(ma_y)}{S^2} - \frac{1}{\pi a_{,y}^3 m^3} \right] \tag{A.12}$$

which should converge rapidly due to the asymptotic behavior of M^{QS} discussed in the main text.

A.2 Evaluation of 3D Interaction Constants

We have already calculated the interaction constants for dipoles in a 2D array centered at the origin. We have also developed the potential function corresponding to a complete sheet of magentic dipoles, (Eq. A.5 with a complete sum at nonzero x):

$$G_y^{(3)} = \frac{1}{2\pi a_y} \sum_{n=-\infty}^{\infty} \sum_{m=-\infty}^{\infty} {\sum_{l=-\infty}^{\infty}}' e^{-jqla_x} e^{j2\pi my/a_y} K_0 \left[c_m \sqrt{(x - la_x)^2 + n^2 a_z^2} \right], \tag{A.13}$$

where q is the unknown wavenumber of the Bloch-Floquet mode propagating in the lattice. Once again, we separate out the propagating MacDonald Functions:

$$\begin{aligned} \sum_{n=-\infty}^{\infty} {\sum_{l=-\infty}^{\infty}}' K_0 \left[jk \sqrt{(x - la_x)^2 + n^2 a_z^2} \right] &= \frac{\pi}{a_z} \sum_{n=-\infty}^{\infty} {\sum_{l=-\infty}^{\infty}}' \frac{e^{-c_n |x - la_x|}}{c_n} \\ &= \frac{\pi}{a_z} {\sum_{n=-\infty}^{\infty}}' {\sum_{l=-\infty}^{\infty}}' \frac{e^{-c_n |x - la_x|}}{c_n} + \frac{\pi}{a_z} {\sum_{l=-\infty}^{\infty}}' \frac{e^{-jk|x - la_x|}}{jk}, \end{aligned} \tag{A.14}$$

where $c_n = \sqrt{\left(\frac{2\pi l}{a_z}\right) - k^2}$. We calculate the H-field:

$$\begin{aligned}
\mu_0 C_{yy}^{(3)} &= \left(k^2 + \frac{\partial^2}{\partial y^2}\right) G_y^{(3)} \\
&= \frac{1}{2\pi a_y} \sum_{n=-\infty}^{\infty} \sum_{m=-\infty}^{\infty}{}' \sum_{l=-\infty}^{\infty}{}' \left[k^2 - \left(\frac{2\pi m}{a_y}\right)^2\right] K_0\left(c_m \Gamma_{ln}\right) e^{-jqla_x} \\
&\quad + \frac{k^2}{2a_y a_z} \sum_{n=-\infty}^{\infty}{}' \sum_{l=-\infty}^{\infty}{}' \frac{e^{-c_n|l|a_x - jqla_x}}{c_n} \\
&\quad - \frac{jk}{2a_y a_z} \sum_{l=-\infty}^{\infty}{}' e^{-jk|l|a_x - jqla_x}
\end{aligned} \tag{A.15}$$

where $\Gamma_{ln} = \sqrt{l^2 a_x^2 + n^2 a_z^2}$. The last term on the RHS we sum explicitly:

$$\frac{jk}{2a_y a_z} \sum_{l=-\infty}^{\infty}{}' = \frac{k}{2a_y a_z} \frac{\sin k a_x}{\cos k a_x - \cos q a_x} \tag{A.16}$$

to obtain the result given in the main text.

In a similar fashion, we calculate the local E-field at the origin:

$$\begin{aligned}
C_{zy}^{em} = -j\omega \frac{\partial G_y}{\partial x} &= -\frac{j\omega a_x}{2\pi a_y} \sum_{n=-\infty}^{\infty} \sum_{m=-\infty}^{\infty}{}' \sum_{l=-\infty}^{\infty}{}' e^{-jqla_x} \frac{c_m l K_1\left(c_m \Gamma_{ln}\right)}{\Gamma_{ln}} \\
&\quad - \frac{j\omega}{2a_y a_z} \sum_{n=-\infty}^{\infty}{}' \sum_{l=-\infty}^{\infty}{}' \operatorname{sgn}(l)\, e^{-c_n \Gamma_{ln}} e^{-jqla_x} \\
&\quad + \frac{\omega}{2a_y a_z} \frac{\sin q a_x}{\cos k a_x - \cos q a_x}.
\end{aligned} \tag{A.17}$$

Once agin, $C_{zz}^{(3)}$ will have an identical form as Eq. A.17 upon the substitution $(ay, az) \rightarrow (az, ay)$. We note that in the limit $qa_x \rightarrow 0$, the first two terms in equation A.17 become antisymmetric and vanish identically. However, the plane wave terms persist as discussed in the main text.

A.3 Interaction Constants for a CMM-Loaded Waveguide

As discussed in Section 5.3, the interaction constant of CMMs is given by that of a conventional MM array with the addition of the contribution from dipoles on the other side of the PEC surface. We label this side (B) for consistency with our previous description. The potential function from the unit dipoles on side (B) is therefore:

$$G_y^{(3)} = \frac{1}{2\pi a_y} \sum_{m=-\infty}^{\infty} {\sum_{l=-\infty}^{\infty}}' e^{-jqla_x} e^{j2\pi my/a_y} K_0\left(c_m \left|l\right| a_x\right), \tag{A.18}$$

where $c_m = \left[\left(2m\pi/a_y\right)^2 - k_0^2\right]$. Once more, we separate out the propagating terms:

$$\sum_{l=-\infty}^{\infty} e^{-jqla_x} K_0\left[jk_0\left(z^2 + l^2a_x^2\right)^{1/2}\right] - K_0\left(jk_0\left|z\right|\right) \tag{A.19}$$

$$\sum_{l=-\infty}^{\infty} e^{-jqla_x} K_0\left[jk_0\left(z^2 + l^2a_x^2\right)^{1/2}\right] = \frac{\pi}{a_x} \sum_{l=-\infty}^{\infty} \frac{e^{-\alpha_l|z|}}{\alpha_l}, \tag{A.20}$$

where $\alpha_l = \sqrt{\left(\frac{2\pi l}{a_x} + q\right)^2 - k_0^2}$, and we choose the branch of the square root according to $\mathrm{Re}\left[\sqrt{\ }\right] > 0$.

Assuming $kd \ll 1$ and $qd \ll 1$,

$$\frac{\pi}{a_x} \sum_{l=-\infty}^{\infty} \frac{e^{-\alpha_l|z|}}{\alpha_l} \approx -j\frac{\pi}{a_x}\frac{1}{\sqrt{k_0^2 - q^2}} + \sum_{l=1}^{\infty} \frac{e^{-2\pi l/ax|z|}}{l}. \tag{A.21}$$

The final term on the RHS we can sum as before:

$$\sum_{l=1}^{\infty} \frac{e^{-2\pi l/ax|z|}}{l} = -\log\left(1 - e^{-2\pi|z|/a_x}\right). \tag{A.22}$$

This term cancels the logarithmic singularity in Eq. A.19 in the limit $z \to 0$. We can then use the approximation in Eq. A.20 as a dominant series so that the final

expression for the potential is:

$$G_y^{(3,B)} = \frac{1}{2\pi a_y} \sum_{m=-\infty}^{\infty}{}' \sum_{l=-\infty}^{\infty}{}' e^{-jqla_x} e^{j2\pi my/a_y} K_0\left(c_m \left|l\right| a_x\right)$$
$$-\frac{1}{2\pi a_y}\left[j\frac{\pi}{a_x}\frac{1}{\sqrt{k_0^2-q^2}} + \gamma + \log\frac{2\pi k}{a_x} + j\frac{\pi}{2}\right] \tag{A.23}$$
$$+\frac{1}{2\pi a_y}\sum_{l=1}^{\infty}\left(\frac{2\pi}{\alpha_l a_x} - \frac{1}{l}\right)$$

$$C_{yy}^{(3,B)} = \frac{1}{2\pi a_y} \sum_{m=-\infty}^{\infty}{}' \sum_{l=-\infty}^{\infty}{}' \left[k_0^2 - \left(\frac{2\pi m}{a_y}\right)^2\right] e^{-jqla_x} e^{j2\pi my/a_y} K_0\left(c_m \left|l\right| a_x\right)$$
$$-\frac{k_0^2}{2\pi a_y}\left[j\frac{\pi}{a_x}\frac{1}{\sqrt{k_0^2-q^2}} + \gamma + \log\frac{2\pi k}{a_x} + j\frac{\pi}{2}\right] \tag{A.24}$$
$$+\frac{k_0^2}{2\pi a_y}\sum_{l=1}^{\infty}\left(\frac{2\pi}{\alpha_l a_x} - \frac{1}{l}\right).$$

Appendix B

Power Expended by a Plane Wave on an Induced Current Source

Our derivation for the modified Sipe-Kranendonk condition is based on the fact that the power spent by a wave exciting an element is described by:

$$P^{ext} = \frac{1}{2}\mathbf{J}_m^* \cdot \mathbf{H}_0, \tag{B.1}$$

which is equal to the power radiated by the dipole acting as a source. We consider an electromagnetic wave $\mathbf{E}_0$ impinging on a magnetic element. We consider the total fields to be given by:

$$\mathbf{E} = \mathbf{E_0} + \mathbf{E_s}, \tag{B.2}$$

and similarly for $\mathbf{H}$. The incident fields satisfy Maxwell's equations in the absence of the source, and the the scattered fields satisfy Maxwell's equations in the absence of the incident fields with the induced dipole acting as a source $\mathbf{M}$. The integral form of Poynting's theorem may then be written as:

$$\begin{aligned}\frac{1}{2}\oint [\mathbf{E}_0 \times \mathbf{H}_0^*] \cdot d\mathbf{S} + \frac{1}{2}\oint [\mathbf{E}_s \times \mathbf{H}_s^*] \cdot d\mathbf{S} + \frac{1}{2}\oint [\mathbf{E}_0 \times \mathbf{H}_s^* + \mathbf{E}_s \times \mathbf{H}_0^*] \cdot d\mathbf{S} \\ = -\frac{1}{2}\int (\mathbf{H}^* \cdot \mathbf{J}_m)\, dV.\end{aligned} \tag{B.3}$$

The first term on the LHS of is identically zero since no power is generated in the absence of the dipole. The second term is the power radiated by the source $\mathbf{M}$. The term on the RHS is the power absorbed. The remaining term on the LHS bears more investigation. We first write this term in differntial form Using Guass's Theorem:

$$\frac{1}{2}\oint[\mathbf{E}_0\times\mathbf{H}_s^*+\mathbf{E}_s\times\mathbf{H}_0^*]\cdot d\mathbf{S}=\frac{1}{2}\int\nabla\cdot[\mathbf{E}_0\times\mathbf{H}_s^*+\mathbf{E}_s\times\mathbf{H}_0^*]\cdot dV. \tag{B.4}$$

Using the vector identity $\epsilon_{ijk}\partial_i A_j B_k = \epsilon_{ijk}A_i\partial_j B_k - \epsilon_{ijk}B_i\partial_j A_k$ and Maxwell's Equations, we find the integrand reduces to:

$$\nabla\cdot[\mathbf{E}_0\times\mathbf{H}_s^*+\mathbf{E}_s\times\mathbf{H}_0^*]=-\mathbf{H}_0\cdot\mathbf{J}_m^*. \tag{B.5}$$

From conservation of power, this must be equal to the negative of the power expended by the incident field, P^{ext}, and we may use Eq. B.1 with confidence.

Appendix C

Network Parameters and the Discrete Dipole Approximation

In Chapter 4, we developed our DDA model based on the assumption that the incident fields were specified. However, we must take additional steps to integrate the DDA into a fully-realized network model. This model must self-consistently account for all possible excitation modes for a DDA array, as well as the effect of the array on other subsystems.

In this Appendix, we develop just such a model for the case of MMs in a parallel plate waveguide. We go on to derive a semi-analytical for a common excitation source; a coaxial probe. We show that a small probe can be integrated self-consistently into DDA simulations to compute network parameters in a single step.

C.1 Antenna Reciprocity in a Parallel Plate Waveguide

In this section we briefly reproduce from [131] a derivation for the transmit and receive property of an antenna in a parallel plate waveguide in terms of the cylindrical harmonics of the fundamental TM^z mode of the guide. The antenna geometry is

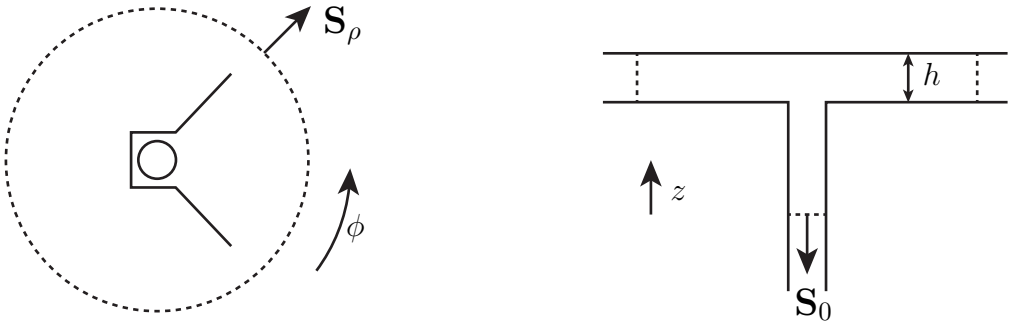

(a) Top View (b) Side View

FIGURE C.1: Geometry for the derivation of T_n and R_n. An arbitrary antenna is placed at the origin of our coordinate system.

shown in Fig. C.1.

We first consider the contribution from the fields in the waveguide. We assume only a single mode propagates in the waveguide so that the contribution from higher-order modes is negligible at the surface S_0. We define equivalent voltages and currents such that the tangential fields are given by:

$$\begin{aligned} \mathbf{E}_t &= V\mathbf{e}_t \\ \mathbf{H}_t &= I\mathbf{h}_t, \end{aligned} \tag{C.1}$$

subject to the normalization condition $\oint\!\!\!\!\!\!\int \mathbf{e}_t \times \mathbf{h}_t^* d\mathbf{S} = 1$.

For the first set fields, we consider the antenna to be operating in the transmit mode. In general, there will exist a forward travelling wave from the source and a reflected wave from the impedance mismatch between the waveguide and the antenna. We define the forward travelling voltage amplitude as a_0 and reflected amplitude as b_0. Defining our terminal plane at S_0, we then have:

$$\begin{aligned} V^{(1)} &= a_0 + b_0 \\ I^{(1)} &= Y_c \left(a_0 - b_0\right), \end{aligned} \tag{C.2}$$

where Y_c is the characteristic impedance of the waveguide mode. For our second set of fields (2) we assume that the antenna is receiving and so only backwards travelling

waves of amplitude b_0' exist in the guide. We therefore have on S_0:

$$\begin{aligned} V^{(2)} &= b_0' \\ I^{(2)} &= -b_0'. \end{aligned} \tag{C.3}$$

Since there are no sources within the surfaces $\mathbf{S}_\rho$ and $\mathbf{S}_0$, the Lorentz Reciprocity theorem reduces to:

$$\oint \left(\mathbf{E}^{(1)} \times \mathbf{H}^{(2)} - \mathbf{E}^{(2)} \times \mathbf{H}^{(1)}\right) \cdot d\mathbf{A} = 0. \tag{C.4}$$

The total contribution to Eq.C.4 from S_0 is then:

$$\int_{S_0} \left(\mathbf{E}^{(1)} \times \mathbf{H}^{(2)} - \mathbf{E}^{(2)} \times \mathbf{H}^{(1)}\right) = -2Y_c a_0 b_0'. \tag{C.5}$$

We now turn to the cylindrical surface in the parallel plate,S_ρ,. On this surface, the fields may be decomposed in the cylindrical harmonics so that:

$$\begin{aligned} E_z^{(1)} &= \sum_{n=-\infty}^{\infty} H_n^{(2)}(k\rho)\, e^{jn\phi} \\ E_z^{(2)} &= \sum_{m=-\infty}^{\infty} \left[a_m J_m(k\rho) + b_m' H_m^{(2)}(k\rho)\right] e^{jm\phi}, \end{aligned} \tag{C.6}$$

where the height h of the parallel-plate is such that only the TM^z modes propagate. The ϕ-component of $\mathbf{H}$ is given by $H_\phi = -j\left(\omega\mu_0\right)^{-1} \partial_\rho E_z$. Inserting these expressions for the fields into Eq. C.4 and using the orthogonality of complex exponentials, we find the contribution from S_ρ may be written:

$$2\pi\rho \left(E_z^{(1)} H_\phi^{(2)} - E_z^{(2)} H_\phi^{(1)}\right) = -j\rho\,(-1)^n\, a_{-n} b_n \left(jY_n' J_n - J_n' Y_n\right) \tag{C.7}$$

where we have used the identities $J_{-n}(x) = J_n(x)$ and $H_n^{(2)}(x) = J_n(x) - jY_n(x)$. Using the Wronskian for Bessel functions:

$$J_p Y_p' - J_p' Y_p = \frac{2}{\pi x}, \tag{C.8}$$

we find that the C.7 reduces to

$$\frac{4}{k\eta}\left(-1\right)^{n} a_{-n} b_{n}. \tag{C.9}$$

Defining $b_n = T_n a_0$ as our transmitting vector and $b_0' = R_n a_n$ as our receiving vector,

$$R_n = 2\frac{Z_c}{k\eta h}\left(-1\right)^{n} T_{-n}, \tag{C.10}$$

where Z_c is the characteristic impedance of the waveguide.

C.1.1 Network Parameters for the DDA

We begin by considering an arbitrary junction between a waveguide of arbitrary cross-section and the top or bottom of a parallel plate waveguide of height h. We consider this waveguide to be connected to a source so that the junction can be consider an antenna radiating in the parallel plate environment. Both h and the waveguide dimensions are determined so that a single mode propagates in each. We begin by drawing a cylindrical surface around the antenna. The radius of this surface is sufficiently great that the fields on the surface are solely those of the fundamental TM^z modes of the parallel plate. On this surface, the electric field can be written in terms of the cylindrical harmonics:

$$E_z = \sum_{n=-\infty}^{\infty} \left[a_n J_n\left(k\rho\right) + b_n H_n^{(2)}\left(k\rho\right)\right] e^{jn\phi} \tag{C.11}$$

where b_n represent sources inside or on the surface of the probe antenna and a_n represent the fields scattered from the MM array. In practice, we will consider only a finite number of modes N. As in Chapter 2.5, we only need to keep enough terms in our summation to account for the cylindrical modes at the evaluation boundary:

$$N = \text{Ceil}\left(k\rho_0\right) + 6. \tag{C.12}$$

There must be a linear relationship between the vectors **a** and **b**:

$$\mathbf{a} = \mathbf{S}^{(DDA)}\mathbf{b}, \tag{C.13}$$

where $\mathbf{S}^{(DDA)}$ is a scattering matrix that relates the vectors exciting the MM array and the fields scattered by the array. We use the DDA to calculate the dipole moments that are created for an excitation b_n. Thes dipole moments can be translated into the coefficients a_n directly, as we now show.

Consider an isolated element that can be described by a polarizability-per-unit-length, such as a metallic via in our parallel plate. Using the addition theorem for Bessel functions, an element located at ρ' and ϕ' may be expressed as:

$$E^s_{mn} = -j\left(\alpha_e/l\right) E^i_n\Big|_{\rho',\phi'} \frac{k^2}{4\epsilon}\sum_m M\left(k\rho\right) H^{(2)}_m\left(k\rho'\right) e^{jm(\phi-\phi')}. \tag{C.14}$$

where $E^i_n\Big|_{\rho',\phi'} = H^{(2)}_n\left(k\rho'\right) e^{jn\phi'}$. The matrix elements S^{DDA}_{mn} are therefore:

$$S^{(DDA)}_{mn} = -j\left(\alpha_e/l\right)\frac{k^2}{4\epsilon} H^{(2)}_m\left(k\rho'\right) H^{(2)}_n\left(k\rho'\right) e^{j(n-m)\phi'} \tag{C.15}$$

In the case of multiple dipoles, we no longer use the polarizability and incident fields directly, but we instead calculate the dipole moments using the DDA method. Each DDA simulation for an excitation mode $H^{(2)}_n\left(k\rho\right)$ returns a list of dipole moments $l = (1, 2, ...L)$. The matrix elements are therefore:

$$S^{(DDA)}_{mn} = -j\frac{k^2}{4a_z\epsilon}\sum_l p^{(n)}_l H^{(2)}_m\left(k\rho_l\right) e^{-jm\phi_l}, \tag{C.16}$$

The contributions from magnetic dipoles may be included in a similar manner. The field radiated by a per-unit-length dipole **m** at the origin is given by:

$$E_z = \frac{k}{2a_z}\left[\left(jm_x - m_y\right) H^{(2)}_1 e^{j\phi} + \left(jm_x + m_y\right) H^{(2)}_{-1} e^{-j\phi}\right] \tag{C.17}$$

Using the addition theorem again, we find that the total scattering matrix is given by:

$$S_{mn}^{(DDA)} = \frac{k}{2a_z}\sum_i \left\{ \frac{-jk}{2\epsilon} p_i^{(n)} H_m^{(2)}\left(k\rho_i\right) e^{-jm\phi_i} \right.$$

$$\left. + \left[\left(jm_x - m_y\right) H_{m+1}\left(k\rho_i\right)^{(2)} e^{j(m+1)\phi} + \left(jm_x^{(n)} + m_y^{(n)}\right) H_{m-1}\left(k\rho_i\right)^{(2)} e^{-j(m-1)\phi} \right] \right\} \tag{C.18}$$

We must now relate these scattered fields to the signal in the waveguide that excites our antenna. Un the waveguide, the fields will consist of an excitation wave of amplitude a_0 traveling towards the antenna and an oppositely-directed wave of amplitude b_0 that contains contributions from the parallel plate modes exciting the antenna and any impedance mismatches between the waveguide and antenna. The waves propagating away from the antenna in the parallel plate will consist of both the waves transmitted by the antenna and waves scattered by the antenna from the MM array:

$$b_n = T_n a_0 + \sum_m S_{nm} a_m, \tag{C.19}$$

where $\mathbf{S}^{(A)}$ is now the scattering matrix for the antenna itself[1] and $\mathbf{T}$ is the transmitting row vector. Similarly, our receive vector R is a column vector that maps the antenna excitation modes in the parallel plate to the waveguide mode b_0:

$$b_0 = \Gamma_0 a_0 + R_n a_n, \tag{C.20}$$

where Γ_0 is the input reflection for the junction in the absence of the array. In general, The quantities $\mathbf{T}$ and $\mathbf{S}^{(A)}$ must be determined through numerical simulation of the antenna. The transmission vector $\mathbf{T}$ is simply the coefficients of the outgoing Hankel

[1] We note that the elements of the S-matrix do not have the same meaning as in standard network theory since the coefficients a_n and b_n do not relate directly to power flow in the device. Yaghjian defines this matrix as the *source* scattering matrix to highlight this difference. The benefit to this formulation is that the b_n calculated represent the outgoing waves that directly excite the array.

functions in the absence of the array with unit incident waveguide amplitude. These coefficients are found using the orthogonality of exponentials:

$$T_n = \frac{1}{2\pi H_n^{(2)}\left(k\rho'\right)} \int_0^{2\pi} E\left(\rho', \phi\right) e^{-jn\phi} d\phi. \tag{C.21}$$

Similarly, $\mathbf{S}^{(A)}$ may be calculated from:

$$S_{mn}^{(A)} = \frac{1}{2\pi H_m^{(2)}\left(k\rho'\right)} \int_0^{2\pi} E_n\left(\rho', \phi\right) e^{-jm\phi} d\phi \tag{C.22}$$

$\mathbf{R}$ is calculated via reciprocity according to Eq.C.10:

$$R_n = (-1)^{-n} \frac{2Z_0}{k\eta_0 h} T_{-n} \tag{C.23}$$

We may combine Eqs. C.19 and C.20 into a single matrix equation that describes the junction:

$$\begin{pmatrix} b_0 \\ \mathbf{b} \end{pmatrix} = \begin{pmatrix} \Gamma_0 & \mathbf{R} \\ \mathbf{T} & \mathbf{S^{(A)}} \end{pmatrix} \begin{pmatrix} a_0 \\ \mathbf{a} \end{pmatrix} \tag{C.24}$$

Ideally, we would calculate the input reflection coefficient:

$$\Gamma = \Gamma_0 + \frac{\mathbf{Ra}}{a_0} \tag{C.25}$$

And all the array excitation coefficients

$$\mathbf{b} = \left(\mathbf{I} - \mathbf{S}^{(1)}\mathbf{S}^{(2)}\right)^{-1} \mathbf{T} a_0, \tag{C.26}$$

which in turn allows us to determine the dipole moments in the array.

However, this formulation requires us to perform a DDA calculation for all N cylindrical harmonics to account for both the fields radiated by the antenna as well as the fields caused by multiple scattering events between the array and antenna. If we assume that these back scattered fields are weak, then the fields scattered by

FIGURE C.2: Comparison of Network Model to 2D Full-Wave Simulation. The inset shows the displacement of the scatterer with respect to the antenna.

the antenna will be negligible and we can neglect the scattering matrix $\mathbf{S}^{(1)}$ in our calculations[132]. Our approximation is therefore:

$$\mathbf{b} \approx \mathbf{T} a_0, \tag{C.27}$$

and

$$\Gamma \approx \Gamma_0 + \mathbf{R}\mathbf{S}^{(2)}\mathbf{T}. \tag{C.28}$$

We test this approximate model using a simple 2D simulation in COMSOL, as shown in the inset to Fig. C.2. The antenna consists of a PEC cylinder with a portion cut-out to provide a well-defined waveguide region. The walls of the waveguide are PMC to that the mode in the waveguide is TEM. Our scatter is a single small PEC cylinder. The polarizability per-unit-length is calculated directly from Mie theory:

$$\alpha_e = \frac{2\pi\epsilon a_z}{k^2\left[\log\left(0.89ka\right) + j\pi/2\right]}, \tag{C.29}$$

where a is the cylinder radius.

In COMSOL, we simulate the antenna in isolation and use Eq. C.21 and Eq. C.22 to calculate the relevant parameters (Γ_0 is returned autmomatically by COMSOL). We then simulate the antenna with the small scatterer placed at various separations and compare our model against COMSOL. Fig. C.2 shows the variation in the real part of Γ as a function of this displacement. Both the full model (Eq. C.26 and Eq. C.25 and the approximate model (Eq. C.27 and Eq. C.28) show excellent agreement to the COMSOL model. Residual error may be due to our omission of the magnetic polarizability.

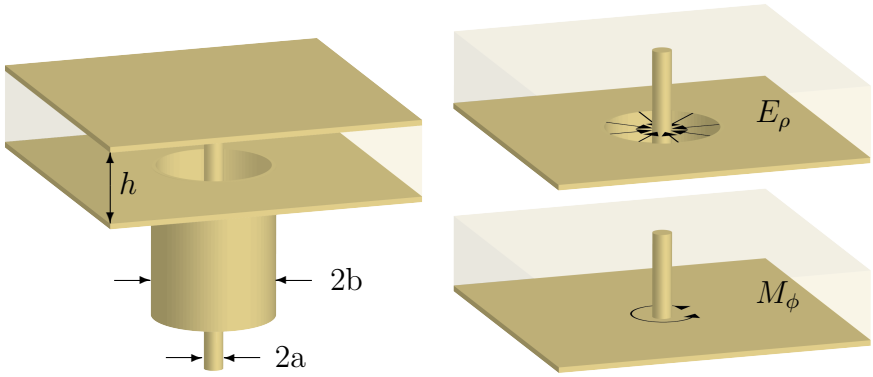

FIGURE C.3: (Left)Diagram of a coaxial probe in a parallel-plate waveguide.(Right) Magnetic frill model for probe radiation and scattering. (Top,Right) The presumed aperture field. (Bottom,Right) The magnetic frill current equivalent.

C.1.2 Probe Coupling and Scattering Model

In our simulations, we need to know at least three parameters of the probe antenna at each frequency: the transmission coefficient, the receive coefficient, and the scattering coefficient. This assumes that only the TEM mode propagates in the probe and that the probe scatters appreciably into the zeroth order cylindrical mode of the parallel plate. For larger probes, it may be necessary to include the response to the $m = \pm 1$ modes which can be represented by a magnetic polarizability.

These quantities may be determined numerically, but multiple simulations must be performed at every frequency of interest. Any changes made to the electrical characteristics of the probe or the waveguide will require a new set of simulations. Additionally, power conservation enforces strict relationships between the various probe parameters. Any numerical error might cause the DDA simulations to become unstable. We therefore develop a semi-analytical model for the probe. While approximate, this model guarantees stability in our simulations and allows us to make changes to the geometry without running additional simulations on the probe itself. Our model is based on the theoretical development presented in [133] for the input

impedance of a transmitting probe. We will first reproduce this derivation, and then we will extend to include the receiving and scattering parameters.

Consider the probe as shown in Fig. C.3. The symmetry of the problem allows us to restrict our consideration to TM^z modes propagating in both the coaxial cable and the parallel plate.

It will also prove beneficial to first consider a related problem. We replace the aperture with an infinitesimal gap between the closed bottom conductor and the center pin. The impressed field in is given by $E_z(a,z) = -\delta(z)$ since E_z is zero on the pin surface. away from the pin, the fields are given by:

$$E_z(\rho,z) = \sum_{m=0}^{\infty} B_m H_0^{(2)}(k_m\rho)\cos\frac{m\pi z}{h} \tag{C.30}$$

where $k_m = \sqrt{k^2 - \left(\frac{m\pi z}{h}\right)^2}$. The coefficients B_m are found with standard techniques. We set equation C.30 equal to $-\delta(z)$ on the pin surface and the orthogonality of cosines yields:

$$B_m = \frac{-2}{h(1+\delta_{m0})H_0^{(2)}(k_m a)}. \tag{C.31}$$

We now turn our attention back to the original problem. We assume that the field at the junction between the coaxial cable and the bottom plate can be represented by the fundamental mode of the probe, normalized to produce one volt at the aperture. This constitutes the only approximation in our formulation, but it greatly simplifies the rest of the derivation. Love's equivalence principle allows us close the aperture and replace it with a magnetic surface current:

$$K_\phi^{(m)} = -\frac{1}{\rho\log b/a}. \tag{C.32}$$

The input admittance is simply the current flowing in on the inner conductor of the poin for the 1V impressed potential. The current may be found using reciprocity

arguments. Our first set of solutions for the reciprocity theorem are the impressed magnetic current given by Eq. C.32 and it's fields. We designate a "test" ring of magnetic current $I_m = \delta(\rho - a)\,\delta(z)$ and its fields as our second set. The reciprocity theorem then reads

$$I_z^m = H_\phi^{(1)} = \int_0^{2\pi} \int_a^b H_\phi^{(2)} M_\phi^{(1)} \rho d\rho d\phi, \tag{C.33}$$

where

$$H_\phi^{(2)}(\rho, 0) = -\frac{j}{\omega\mu_0} \sum_{m=0}^{\infty} B_m k_m H_0^{(2)'}(k_m \rho), \tag{C.34}$$

since the ring of magnetic current is equivalent to the infinitesimal gap previously discussed. Inserting Eq. C.32, Eq.C.31, and Eq. C.34 into Eq. C.33 yields:

$$Y_{in} = -\frac{j4\pi k}{h\eta \log b/a} \sum_{m=0}^{\infty} \frac{H_0^{(2)}(k_m b) - H_0^{(2)}(k_m a)}{k_m^2 (1 + \delta_{m0}) H_0^{(2)}(k_m a)}. \tag{C.35}$$

To determine the the transmission coefficients of the probe, we must know how the frill radiates in the presence of the pin. Unfortunately, we can not use Eqs. C.30 and C.31 since these are only valid for a ring of zero thickness.

Instead, we use reciprocity again. The frill will generate fields that consist of all TM^z modes, but only the fundamental TEM mode will radiate. The magnetic surface current at the aperture is:

$$K_\phi^{(m)(1)} = -\frac{2Z_c}{Z_c + Zi} \frac{1}{\rho \log b/a}, \tag{C.36}$$

where we have use the aperture voltage $V = 1 + \Gamma$ has been calculated from the known impedance Z_i. We then designate the corresponding fields as:

$$\begin{aligned} E_z^{(1)} &= T_0 H_0^{(2)}(k\rho) \\ H_\phi^{(1)} &= \frac{k}{j\omega\mu} T_0 H_0'^{(2)}(k\rho), \end{aligned} \tag{C.37}$$

where T_0 is the to-be-determined transmission coefficient. We choose our second set of fields as those of an incident field $E_z^i = J_0(k\rho)$ and the scattered fields from the metal pin:

$$\begin{aligned} E_z^{(2)} &= J_0(k\rho) - \Gamma_{00} H_0^{(2)}(k\rho) \\ H_\phi^{(2)} &= \frac{k}{j\omega\mu}\left[J_0'(k\rho) - \Gamma_{00} H_0'^{(2)}(k\rho)\right], \end{aligned} \tag{C.38}$$

where $\Gamma_{00} = J_0(ka)/H_0^{(2)}(ka)$. The Lorentz Reciprocity Theorem in integral form reduces to:

$$\oint \left(E_z^{(1)} H_\phi^{(2)} - E_z^{(2)} H_\phi^{(1)}\right) \rho d\phi dz = \int \left(H_\phi^{(2)} M_\phi^{(1)}\right) \rho d\rho d\phi \tag{C.39}$$

Evaluation of the RHS is trivial. Using the Wronskian of Bessel functions on the LHS, we find:

$$T_0 = \frac{Z_i}{Z_i + Z_c} \frac{\pi}{h \log b/a} \frac{J_0(0,kb)\, Y_0(0,ka) - J_0(0,ka)\, Y_0(0,kb)}{H_0^{(2)}(0,ka)} \tag{C.40}$$

The last quantity of interest is the polarizability of the probe. To find this quantity, we once again assume an incident field $E_z^i = J_0(k\rho)$. Fields will be scattered due to the presence of the pin and the surrounding aperture. However, these scattered fields are not independent; the scattering from either obstacle must be determined in the presence of the other.

We begin by closing the aperture and replacing the aperture field with an unknown magnetic surface current density. The total scattered fields are now seen to be a superposition of the magnetic current radiating in the presence of the pin and the fields scattered by the pin in the absence of the aperture. This magnetic current is determined by the aperture fields in the receive mode of the antenna, which we have already calculated.

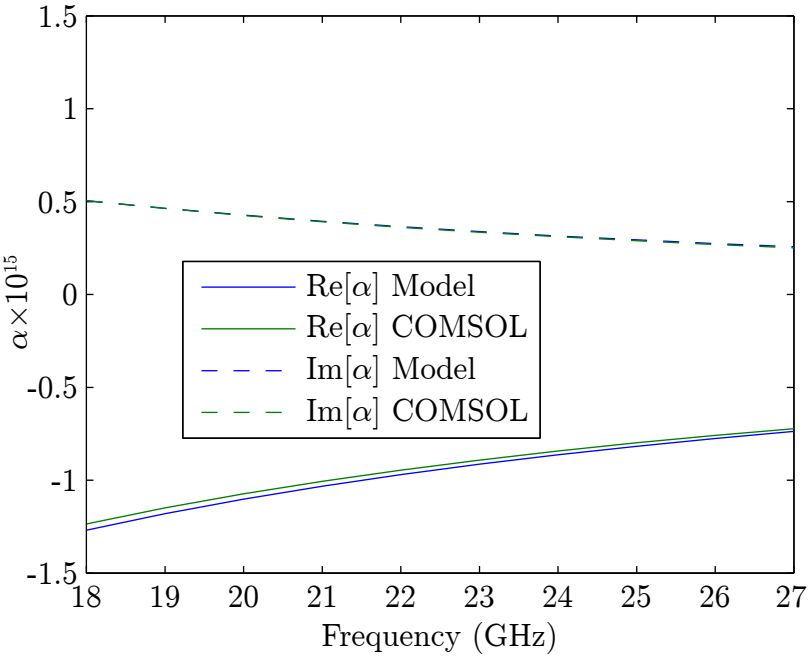

FIGURE C.4: Comparison of Probe Models

The receiving coefficient from Eq. C.23 is:

$$R_0 = \frac{2Z_c}{k\eta h} T_0 \tag{C.41}$$

The received signal is simply R_0, so the field at the aperture is simply $-\frac{R_0}{\rho \log b/a}$. This field radiates in the same manner as the transmit antenna. We then add to this the scattered field from the pin to and compare to the field radiated by a p.u.l dipole to determine the polarizability:

$$\alpha = j\frac{4\epsilon Z_c}{k^3 \eta h} T_0^2 + \alpha_{00}, \tag{C.42}$$

where α_{00} is the polarizability of the isolated pin calculated from Eq. C.29. Fig.C.4 shows the retrieved polarizability from as standard probe simulated COMSOL and the polarizability calculated from our model. Agreement is excellent for all the frequencies simulated, and we may confidently use our model in design.

We are fortunate that most coaxial probes are electrically small and therefore well characterized by an electrical polarizability. This allows us to include them in our DDA simulations self-consistently without forcing us to run multiple simulations to account for all the different excitation and scattering modes.

Specifically, we run a simulation using a normalized source centered at the probe. There is clearly a singularity in the field at this position, but we set the excitation field to be identically zero at this point since the probe does not scatter from its own excitation. Once we have performed our simulation, the signal recieved by the probe is determined by the local field exciting the probe in the parallel plate, i.e.

$$V_s = R_0 \frac{p_z}{\alpha_{zz}^{ee}} \tag{C.43}$$

In this manner we are able to calculate the S-parameters for the device shown in the main text.

Bibliography

[1] Landy, N. I., Urzhumov, Y. A., and Smith, D. R., Quasi-Conformal Approaches for Two and Three-Dimensional Transformation Optical Media, in *Transformation Electromagnetics and Metamaterials*, Springer US, 2014.

[2] Landy, N. I. and Smith, D. R., Nature Mater. **12** (2013) 25.

[3] Kundtz, N. B., *Advances in Complex Artificial Electromagnetic Media*, PhD thesis, Duke University, 2009.

[4] Schurig, D., Pendry, J. B., and Smith, D. R., Opt. Express **14** (2006) 9794.

[5] Prost, E. J., *Formal Structure of Electromagnetics*, Dover Publications, 1997.

[6] Pendry, J. B., Schurig, D., and Smith, D. R., Science (New York, N.Y.) **312** (2006) 1780.

[7] Zhang, B., Luo, Y., Liu, X., and Barbastathis, G., Phys. Rev. Lett. **106** (2011) 033901.

[8] Chen, X. et al., Nat. Commun. **2** (2011) 176.

[9] Schurig, D. et al., Science (New York, N.Y.) **314** (2006) 977.

[10] Liu, R. et al., Science (New York, N.Y.) **323** (2009) 366.

[11] Ma, Y. G., Ong, C. K., Tyc, T., and Leonhardt, U., Nature Mater. (2009) 1.

[12] Valentine, J., Li, J., Zentgraf, T., Bartal, G., and Zhang, X., Nature Mater. **8** (2009) 568.

[13] Li, C., Liu, X., and Li, F., Phys. Rev. B **81** (2010) 115133.

[14] Ma, H. F. and Cui, T. J., Nat. Commun. **1** (2010) 21.

[15] Ma, H. F. and Cui, T. J., Nat. Commun. **1** (2010) 124.

[16] Fischer, J., Ergin, T., and Wegener, M., Opt. Lett. **36** (2011) 2059.

[17] Tichit, P.-H., Burokur, S. N., Germain, D., and de Lustrac, A., Phys. Rev. B **83** (2011) 155108.

[18] Hunt, J., Kundtz, N. B., Sun, B., and Smith, D. R., **8021** (2011) 80210O.

[19] Hunt, J., Jang, G., and Smith, D. R., J. Opt. Soc. Am. B **28** (2011) 2025.

[20] Hunt, J. et al., Opt. Express **20** (2012) 1706.

[21] Driscoll, T. et al., Opt. Express **20** (2012) 28.

[22] Yang, F., Mei, Z. L., Jin, T. Y., and Cui, T. J., Phys. Rev. Lett. **109** (2012) 053902.

[23] Shelkunoff, S. A. and Friis, H. T., *Antennas: Theory and Practice*, Wiley, New York, 1952.

[24] Pendry, J. B., Holden, A. J., Robbins, D. J., and Stewart, W. J., IEEE Trans. Microw. Theory Tech. **47** (1999) 2075.

[25] Ramo, S., Whinnery, J., and Van Duzer, T., *Fields and Waves in Communication Electronics*, John Wiley & Sons, 3rd edition, 1994.

[26] Balanis, C., *Advanced Engineering Electromagnetics*, John Wiley & Sons, New York, 1989.

[27] Petschulat, J. et al., Phys. Rev. A **78** (2008) 043811.

[28] Simovski, C. R. and Tretyakov, S. A., Phot. Nano. Fund. Appl. **8** (2010) 254.

[29] Marqués, R., Medina, F., and Rafii-El-Idrissi, R., Phys. Rev. B **65** (2002) 144440.

[30] Smith, D. R., Gollub, J. N., Mock, J. J., Padilla, W. J., and Schurig, D., J. Appl. Phys. **100** (2006) 024507.

[31] Padilla, W. J., Opt. Express **15** (2007) 1639.

[32] Tretyakov, S. A., *Analytical Modeling in Applied Electromagnetics*, Artech House, 2003.

[33] Smith, D. R. and Pendry, J. B., J. Opt. Soc. Am. B **23** (2006) 391.

[34] Simovski, C. R., Metamaterials **1** (2007) 62.

[35] Smith, D. R. et al., Appl. Phys. Lett. **82** (2003) 1506.

[36] Raab, R. E. and De Lange, O. L., *Multipole theory in electromagnetism: classical, quantum, and symmetry aspects, with applications*, Clarendon Press, 2005.

[37] Smith, D. R., Urzhumov, Y. A., Kundtz, N. B., and Landy, N. I., Opt. Express **18** (2010) 21238.

[38] Rahm, M., Cummer, S. A., Schurig, D., Pendry, J. B., and Smith, D. R., Phys. Rev. Lett. **100** (2008) 063903.

[39] Thompson, J., Soni, B., and Weatheri, N. P., editors, *Handbook of Grid Generation*, CRC Press, Boca Raton, 1999.

[40] Li, J. and Pendry, J. B., Phys. Rev. Lett. **101** (2008) 203901.

[41] Knupp, P. and Steinberg, S., *Fundamentals of Grid Generation*, CRC Press, Boca Raton, 1994.

[42] Tang, L. et al., Opt. Express **19** (2011) 15119.

[43] Chang, Z., Zhou, X., Hu, J., and Hu, G., Opt. Express **18** (2010) 6089.

[44] Zhang, B., Chan, T., and Wu, B.-I., Phys. Rev. Lett. **104** (2010) 233903.

[45] Tang, W., Argyropoulos, C., and Kallos, E., IEEE Trans. Antennas. Propag. **58** (2010) 3795.

[46] Kong, F. et al., Appl. Phys. Lett. **91** (2007) 253509.

[47] Mei, Z. L., Bai, J., and Cui, T. J., New J. Phys. **13** (2011) 063028.

[48] García-Meca, C., Martínez, A., and Leonhardt, U., Opt. Express **19** (2011) 23743.

[49] Roberts, D. A., Rahm, M., Pendry, J. B., and Smith, D. R., Appl. Phys. Lett. **93** (2008) 251111.

[50] Rahm, M., Roberts, D. A., Pendry, J. B., and Smith, D. R., Opt. Express **16** (2008) 11555.

[51] Landy, N. I. and Padilla, W. J., Opt. Express **17** (2009) 14872.

[52] Ma, Y. G., Wang, N., and Ong, C. K., J. Opt. Soc. Am. A **27** (2010) 968.

[53] Schurig, D., New J. Phys. **10** (2008) 115034.

[54] Sluijter, M., de Boer, D. K. G., and Braat, J. J. M., J. Opt. Soc. Am. A **25** (2008) 1260.

[55] Sluijter, M., de Boer, D. K., and Paul Urbach, H., J. Opt. Soc. Am. A **26** (2009) 317.

[56] Damaskos, N., IEEE Trans. Antennas. Propag. **30** (1982) 991.

[57] Landy, N. I., Kundtz, N. B., and Smith, D. R., Phys. Rev. Lett. **105** (2010) 193902.

[58] Luneburg R., *Mathematical Theory of Optics*, Univ of California Press, 1964.

[59] Kundtz, N. B. and Smith, D. R., Nature Mater. **9** (2010) 129.

[60] Jacob, Z., Alekseyev, L. V., and Narimanov, E. E., J. Opt. Soc. Am. A **24** (2007) A52.

[61] Press, W. H., Teukolsky, S. A., Vetterling, W. T., and Flannery, B. P., *Numerical Recipes 3rd Edition: The Art of Scientific Computing*, volume 1, 2007.

[62] Halimeh, J. C., Ergin, T., Mueller, J., Stenger, N., and Wegener, M., Opt. Express **17** (2009) 19328.

[63] Ergin, T., Halimeh, J. C., Stenger, N., and Wegener, M., Opt. Express **18** (2010) 20535.

[64] Leonhardt, U., Science (New York, N.Y.) **312** (2006) 1777.

[65] Urzhumov, Y. A., Landy, N. I., and Smith, D. R., J. Appl. Phys. **111** (2012) 053105.

[66] Andreasen, M., IEEE Trans. Antennas. Propag. (1965).

[67] Youngworth, K. and Brown, T., Optics express **7** (2000) 77.

[68] Zhou, J. et al., Phys. Rev. Lett. **95** (2005) 223902.

[69] Tretyakov, S. A., Metamaterials (2007).

[70] Cai, W., Chettiar, U. K., Kildishev, A. V., Shalaev, V. M., and Milton, G. W., Appl. Phys. Lett. **91** (2007) 111105.

[71] Cai, W., Chettiar, U. K., Kildishev, A. V., and Shalaev, V. M., Nature Photon. **1** (2007) 224.

[72] Smolyaninov, I. I., Smolyaninova, V., Kildishev, A. V., and Shalaev, V. M., Phys. Rev. Lett. **102** (2009) 213901.

[73] Yan, M., Ruan, Z., and Qiu, M., Phys. Rev. Lett. **99** (2007) 233901.

[74] Luo, Y., Zhang, J., Chen, H., and Ran, L., IEEE Trans. Antennas. Propag. **57** (2009).

[75] Xi, S., Chen, H., Wu, B.-i., and Kong, J. A., IEEE Microw. Wirel. Compon. Lett. **19** (2009) 131.

[76] Popa, B.-I. and Cummer, S. A., Phys. Rev. B **83** (2011) 224304.

[77] Cummer, S. A., Popa, B.-i., and Hand, T. H., IEEE Trans. Antennas. Propag. **56** (2008) 127.

[78] Kabiri, A., Yousefi, L., and Ramahi, O. M., IEEE Trans. Antennas. Propag. **58** (2010) 2345.

[79] Kildal, P.-S., Electron. Lett. **24** (1988) 3.

[80] Kildal, P.-S., IEEE Trans. Antennas. Propag. **38** (1990).

[81] Kildal, P.-S., Kishk, A. A., and Tengs, A., IEEE Trans. Antennas. Propag. **44** (1996).

[82] Justice, B. J. et al., Opt. Express **14** (2006) 8694.

[83] Miligan, T. A., *Modern Antenna Design*, Wiley, New York, 2nd edition, 2005.

[84] Kundtz, N. B., Gaultney, D., and Smith, D. R., New J. Phys. **12** (2010) 043039.

[85] Simovski, C. R., Opt. Spectrosc. **107** (2009) 726.

[86] Bowen, P. T., Driscoll, T., Kundtz, N. B., and Smith, D. R., New J. Phys. **14** (2012) 033038.

[87] Belov, P. A. and Simovski, C. R., Phys. Rev. E **72** (2005) 026615.

[88] Smith, D. R., Phys. Rev. E **81** (2010) 036605.

[89] Purcell, E. and Pennypacker, C., Astrophys. J. **186** (1973) 705.

[90] Yurkin, M. and Hoekstra, A. G., Journal of Quantitative Spectroscopy and Radiative Transfer (2007).

[91] Yurkin, M. a., Hoekstra, A. G., Brock, R. S., and Lu, J. Q., Opt. Express **15** (2007) 17902.

[92] Liu, C., Bi, L., Panetta, R. L., Yang, P., and Yurkin, M. A., Opt. Express **20** (2012) 16763.

[93] Lakhtakia, A., Astrophys. J. **394** (1992) 494.

[94] Mulholland, G., Bohren, C., and Fuller, K., Langmuir **10** (1994).

[95] de La Osa, R. A., Albella, P., and Saiz, J., Opt. Express **18** (2010) 23865.

[96] Ewald, P. P., Ann. Phys. **369** (1921) 253.

[97] Reinert, J. and Jacob, A. F., IEEE Trans. Antennas. Propag. **49** (2001) 1532.

[98] Jelinek, L. and Baena, J. D., Proc. 36th Microw. Conference **0** (2006) 983.

[99] Silveirinha, M. G., Phys. Rev. B **83** (2011) 165104.

[100] Rockstuhl, C. et al., Phys. Rev. B **83** (2011) 245119.

[101] Fietz, C., Urzhumov, Y. A., and Shvets, G., Opt. Express **19** (2011) 9681.

[102] Andryieuski, A., Ha, S., Sukhorukov, A. A., Kivshar, Y. S., and Lavrinenko, A. V., Phys. Rev. B **86** (2012) 035127.

[103] Smith, D. R. and Schultz, S., Phys. Rev. B **65** (2002) 195104.

[104] Smith, D. R., Vier, D. C., Koschny, T., and Soukoulis, C. M., Phys. Rev. E **71** (2005) 036617.

[105] Nicolson, A. M. and Ross, G. F., IEEE Transactions on Instrumentation and Measurement **19** (1970) 377.

[106] Weir, W. B., Pro. IEEE **62** (1974).

[107] Koschny, T., Markoš, P., Smith, D. R., and Soukoulis, C. M., Phys. Rev. E **68** (2003) 065602.

[108] Koschny, T. et al., Phys. Rev. B **71** (2005) 245105.

[109] Liu, R., Cui, T. J., Huang, D., Zhao, B., and Smith, D. R., Phys. Rev. E **76** (2007) 026606.

[110] Chen, X., Grzegorczyk, T. M., Wu, B.-I., Pacheco, J., and Kong, J. A., Phys. Rev. E **70** (2004) 016608.

[111] Qi, J. and Kettunen, H., IEEE Antenn. Wireless Propag. Lett. **9** (2010) 1057.

[112] Liu, X.-X., Powell, D. A., and Alù, A., Phys. Rev. B **84** (2011) 235106.

[113] Scher, A. D. and Kuester, E. F., Metamaterials **3** (2009) 44.

[114] Karamanos, T. D. and Dimitriadis, A., Advanced Electromagnetics (2012).

[115] Draine, B. T. and Goodman, J., Astrophys. J. **405** (1993) 685.

[116] Collin, R. E., *Field Theory of Guided Waves*, IEEE Press, New York, 2nd edition, 1991.

[117] Vinogradov, A. P., Ignatov, A. I., Merzlikin, A. M., Tretyakov, S. A., and Simovski, C. R., Opt. Express **19** (2011) 6699.

[118] Simovski, C. R. and Tretyakov, S. A., Phys. Rev. B **75** (2007) 195111.

[119] Lemaire, T., J. Opt. Soc. Am. A **14** (1997) 470.

[120] Goodman, J., Draine, B. T., and Flatau, P. J., Opt. Lett. **16** (1991) 1198.

[121] Bethe, H., Phys. Rev. (1944).

[122] Collin, R. E., *Foundations for Microwave Engineering*, John Wiley & Sons, New York, 2000.

[123] Pozar, D. M., *Microwave Engineering*, John Wiley & Sons, New York, 3rd edition, 2005.

[124] Monk, B., *Frequency Selective Surfaces: Theory and Design*, John Wiley & Sons, New York, 2000.

[125] Falcone, F. et al., Phys. Rev. Lett. **93** (2004) 197401.

[126] Hand, T. H., Gollub, J. N., Sajuyigbe, S., Smith, D. R., and Cummer, S. A., Appl. Phys. Lett. **93** (2008) 212504.

[127] Yang, X. M. et al., IEEE Trans. Antennas. Propag. **59** (2011) 373.

[128] Sipe, J. E. and Kranendonk, J. V., Phys. Rev. A **9** (1974).

[129] Oliner, A. A. and Jackson, D. R., Leaky Wave Antennas, in *Modern Antenna Handbook*, pages 325–368, 2008.

[130] Landy, N. I., Hunt, J., and Smith, D. R., Phot. Nano. Fund. Appl. (2013).

[131] Yaghjian, A. D., *Near-field Antenna measurements on a cylindrical surface: a source-scattering matrix formulation*, 1977.

[132] Giovampaola, C. D., Martini, E., Toccafondi, A., Member, S., and Maci, S., IEEE Trans. Antennas. Propag. **60** (2012) 4316.

[133] Xu, H., Jackson, D. R., and Williams, J. T., IEEE Trans. Antennas. Propag. **53** (2005) 3229.

[134] Landy, N. I. and Chen, H.-T., Infrared and Millimeter Waves, 2007 and the 2007 15th International Conference on Terahertz Electronics. IRMMW-THz. Joint 32nd International Conference on. IEEE, 2007 (2007).

[135] Landy, N. I., Sajuyigbe, S., Mock, J. J., Smith, D. R., and Padilla, W. J., Phys. Rev. Lett. **100** (2008) 207402.

[136] Tao, H., Landy, N. I., and Bingham, C., Opt. Express **16** (2008) 1494.

[137] Landy, N. I. et al., Phys. Rev. B **79** (2009) 125104.

[138] Hunt, J., Kundtz, N. B., Landy, N. I., and Smith, D. R., Appl. Phys. Lett. **97** (2010) 024104.

[139] Hunt, J. et al., Sensors (Basel, Switzerland) **11** (2011) 7982.

[140] Urzhumov, Y. A., Landy, N. I., Driscoll, T., Basov, D. N., and Smith, D. R., Opt. Lett. **38** (2013) 1606.

[141] Urzhumov, Y. A., Landy, N. I., Ciracì, C., and Smith, D. R., Going Beyond Axisymmetry :2 . 5D Vector Electromagnetics, in *COMSOL*, pages 1–4.

Biography

Nathan Ingle Landy was born on August 3, 1983 in Newton, Massachusetts. He graduated from Weston High School in his hometown of Weston, Massachusetts in June of 2002. Nathan earned a Bachelor of the Arts in Physics from Swarthmore College in Swarthmore, Pennsylvania, in 2006; and will complete a Ph.D. in Electrical Engineering at Duke University in Durham, North Carolina, in 2013.

In 2010, Nathan was one of eleven students selected to give an early career presentation at the IWEM (International Workshop on Electromagnetic Metamaterails) Conference. He won an award for Best Student Paper at the Metamorphose Metamaterials Congress in Barcelona, Spain, in 2011.

Upon graduation from Duke University, Nathan will be working at the Metamaterials Commercialization Center at Intellectual Ventures in Bellevue, Washington.

A complete list of Nathan's publications may be found below:

- Landy, N. I. and Chen, H.-T., Infrared and Millimeter Waves, 2007 and the 2007 15th International Conference on Terahertz Electronics. IRMMW-THz. Joint 32nd International Conference on. IEEE, 2007 (2007)

- Landy, N. I., Sajuyigbe, S., Mock, J. J., Smith, D. R., and Padilla, W. J., Phys. Rev. Lett. **100** (2008) 207402

- Tao, H., Landy, N. I., and Bingham, C., Opt. Express **16** (2008) 1494

- Landy, N. I. and Padilla, W. J., Opt. Express **17** (2009) 14872

- Landy, N. I. et al., Phys. Rev. B **79** (2009) 125104
- Hunt, J., Kundtz, N. B., Landy, N. I., and Smith, D. R., Appl. Phys. Lett. **97** (2010) 024104
- Landy, N. I., Kundtz, N. B., and Smith, D. R., Phys. Rev. Lett. **105** (2010) 193902
- Hunt, J. et al., Sensors (Basel, Switzerland) **11** (2011) 7982
- Driscoll, T. et al., Opt. Express **20** (2012) 28
- Urzhumov, Y. A., Landy, N. I., and Smith, D. R., J. Appl. Phys. **111** (2012) 053105
- Landy, N. I. and Smith, D. R., Nature Mater. **12** (2013) 25
- Landy, N. I., Hunt, J., and Smith, D. R., Phot. Nano. Fund. Appl. (2013)
- Urzhumov, Y. A., Landy, N. I., Driscoll, T., Basov, D. N., and Smith, D. R., Opt. Lett. **38** (2013) 1606
- Landy, N. I., Urzhumov, Y. A., and Smith, D. R., Quasi-Conformal Approaches for Two and Three-Dimensional Transformation Optical Media, in *Transformation Electromagnetics and Metamaterials*, Springer US, 2014
- Urzhumov, Y. A., Landy, N. I., Ciracì, C., and Smith, D. R., Going Beyond Axisymmetry :2 . 5D Vector Electromagnetics, in *COMSOL*, pages 1–4